JGR Solid Earth

RESEARCH ARTICLE
10.1029/2025JB032996

Hydroacoustic Observations of the 15 January 2022 Hunga Tonga-Hunga Ha'apai Eruption: The Role of Bathymetry Along the Path

Joel D. Simon[1,2], Frederik J. Simons[1], Jessica C. E. Irving[3], Wenbo Wu[4,5], Masayuki Obayashi[6], Yong Yu[7,8], Yongshun John Chen[7], Hiroko Sugioka[9], and Yann Hello[10]

[1]Department of Geosciences, Princeton University, Princeton, NJ, USA, [2]Now at Bathymetrix, LLC, Portland, OR, USA, [3]School of Earth Sciences, University of Bristol, Bristol, UK, [4]Department of Geology and Geophysics, Woods Hole Oceanographic Institution, Woods Hole, MA, USA, [5]Now at Department of Earth and Planetary Science, University of California, Berkeley, CA, USA, [6]Japan Agency for Marine-Earth Science and Technology, Yokosuka, Japan, [7]Department of Ocean Science and Engineering, Southern University of Science and Technology, Shenzhen, China, [8]Institute of Geology, Chinese Earthquake Administration, Beijing, China, [9]Kobe Ocean-Bottom Exploration Center, Kobe University, Kobe, Japan, [10]Seisocean, Saint Jeannet, Provence-Alpes-Côte d'Azur, France

Abstract The 15 January 2022 submarine volcanic eruption of Hunga Tonga-Hunga Ha'apai released immense energy throughout the ocean, solid Earth, and atmosphere. We analyze mid-oceanic column acoustic pressure recordings from 24 freely drifting Mobile Earthquake Recorder in Marine Areas by Independent Divers sensors, and from 11 moored hydrophones in the International Monitoring System. We focus on the pulsed hydroacoustic phase which propagated horizontally through the ocean as a 30-min *T* wave with energy around 2.5–10 Hz. The records show high correlation between some receivers, significant variation among others, and varying amplitudes that cannot be explained by distance alone. We investigate the origin of this heterogeneity via the influence of bathymetric features that may block, or occlude, *T*-wave propagation, affecting both shape and amplitude of the records received. We count the number of seafloor obstacles within the horizontal plane of the first (ray-theoretical) Fresnel zone at a depth of 1,350 m, where the fundamental-mode *T*-wave eigenfunction is maximal. Adjusted for geometric spreading, the cross-correlations and sound pressure level differences between receivers systematically relate to differences in occlusion count. Our model of signal loss due to seafloor interactions predicts a 5.6 dB reduction in sound pressure level per logarithm of occlusion count, explaining 88% of the *T*-wave sound pressure variance across the ocean. Source characterization requires adequate path models. Our findings describe how to correct signal amplitudes for seafloor roughness. This is important for constraining volcanic or explosive yield estimates and earthquake magnitudes, and useful to model detectability through various oceanic corridors when designing hydroacoustic monitoring networks of the future.

Plain Language Summary An underwater volcano in the South Pacific named Hunga Tonga-Hunga Ha'apai erupted spectacularly on 15 January 2022, generating the loudest sounds heard on Earth in nearly 150 years. We recorded the eruption across the Pacific deep in the ocean, using freely drifting robots called Mobile Earthquake Recorder in Marine Areas by Independent Divers, equipped with underwater microphones called hydrophones. We supplemented this novel data source with acoustic waveforms from tethered hydrophones in the International Monitoring System network. Our data contain a telltale sign of the eruption in the form of "Tertiary" or "*T*" waves: hydroacoustic pressure waves that move horizontally through the ocean at the speed of sound in water. The *T*-wave signals received vary in ways that are not just due to distance effects. We assess whether seafloor interactions—literally, underwater sound being distorted and dampened due to running into mountains on the seafloor—are to blame. To account for these effects we derive a metric we call "bathymetric occlusion," an assessment of the number of obstacles in a *T*-wave's path, to be understood as a measure of path blockage. Ultimately, our model is able to explain almost 90% of the signal variability in our data set.

Key Points:

- Understanding ocean-scale *T*-wave variability will aid source characterization, magnitude, and yield estimation, and inform sensor siting
- *T* waves from the Hunga Tonga-Hunga Ha'apai eruption recorded on Mobile Earthquake Recorder in Marine Areas by Independent Divers and International Monitoring System hydrophones are modified by ocean floor roughness
- We quantify bathymetric interactions of the hydroacoustic *T* waves within the Fresnel zone at the modal depth along their propagation paths

Supporting Information:

Supporting Information may be found in the online version of this article.

Correspondence to:

J. D. Simon,
jdsimon@bathymetrix.com

Citation:

Simon, J. D., Simons, F. J., Irving, J. C. E., Wu, W., Obayashi, M., Yu, Y., et al. (2026). Hydroacoustic observations of the 15 January 2022 Hunga Tonga-Hunga Ha'apai eruption: The role of bathymetry along the path. *Journal of Geophysical Research: Solid Earth*, *131*, e2025JB032996. https://doi.org/10.1029/2025JB032996

Received 15 SEP 2025
Accepted 3 DEC 2025

Author Contributions:

Conceptualization: Joel D. Simon
Data curation: Joel D. Simon
Formal analysis: Joel D. Simon, Frederik J. Simons, Jessica C. E. Irving, Wenbo Wu
Funding acquisition: Frederik J. Simons, Jessica C. E. Irving, Masayuki Obayashi, Hiroko Sugioka
Investigation: Joel D. Simon, Frederik J. Simons, Jessica C. E. Irving
Methodology: Joel D. Simon, Frederik J. Simons, Jessica C. E. Irving, Wenbo Wu
Project administration: Frederik J. Simons, Masayuki Obayashi, Yong Yu,

1. Introduction

The 15 January 2022 Hunga Tonga-Hunga Ha'apai (HTHH) event, a subaqueous phreatomagmatic explosion, was the largest submarine volcanic eruption in nearly 150 years (Terry et al., 2022). It generated seismic disturbances with cumulative magnitude M_W 6.5 (Thurin & Tape, 2023), triggered a megatsunami throughout the

Yongshun John Chen, Hiroko Sugioka, Yann Hello
Resources: Frederik J. Simons, Jessica C. E. Irving, Masayuki Obayashi, Yong Yu, Yongshun John Chen, Hiroko Sugioka, Yann Hello
Software: Joel D. Simon, Frederik J. Simons, Wenbo Wu
Supervision: Frederik J. Simons, Jessica C. E. Irving
Validation: Joel D. Simon
Visualization: Joel D. Simon, Frederik J. Simons
Writing – original draft: Joel D. Simon, Frederik J. Simons, Jessica C. E. Irving, Wenbo Wu
Writing – review & editing: Joel D. Simon, Frederik J. Simons, Jessica C. E. Irving, Wenbo Wu

Pacific (Purkis et al., 2023), set off exceptionally intense and abundant lightning flashes (Yuen et al., 2022), produced atmospheric gravity waves that circled the planet multiple times (C. J. Wright et al., 2022), and excited a broad spectrum of oceanic pressure waves and solid-Earth normal-mode phenomena (Ringler et al., 2023).

Analysis of a wealth of geophysical data from many types of sensors (barometers, infrasound and pressure sensors, hydrophones and seismometers) spanning multiple Earth domains (atmospheric, oceanic, solid-Earth) has shed light on the detailed chronology of the HTHH sequence of events, identifying at least four distinct phases that occurred in the time span of a few hours (Donner et al., 2023; Thurin et al., 2022, 2023; Thurin & Tape, 2023; Zheng et al., 2023). Matoza et al. (2022) and Le Bras et al. (2023) reported a suite of seismoacoustic observations including hydroacoustic time series from the International Monitoring System (IMS). While what can be learned about submarine volcanism and associated phenomena from seismometers and distant hydrophones is remarkable (e.g., Caplan-Auerbach et al., 2001; Dietz & Sheehy, 1954; Latchman et al., 2023; Metz et al., 2016; Matsumoto et al., 2023; Talandier & Okal, 1987; I. C. Wright et al., 2008), overall limited observation of seismo-hydro-acoustic *T* (and *H*, Wilmut et al., 2010; Dall'Osto et al., 2023) phases has stood in the way of providing a full picture of this uniquely important event. Submarine volcanism worldwide is widespread (Tepp & Dziak, 2021) but challenging to observe directly and in real time (e.g., Mittal & Delbridge, 2019; Walker & de Ronde, 2024), which puts a premium on understanding the acoustic record, whether atmospheric (e.g., Maher et al., 2021; Le Bras et al., 2025) or underwater (e.g., Wech et al., 2018, 2025). In particular, we have yet to quantify how hydroacoustic records are shaped by interactions with the rough seafloor.

In this paper we exploit a novel data set of hydroacoustic data from the HTHH event recorded by Mobile Earthquake Recorder in Marine Areas by Independent Divers (MERMAID) sensors (Simons et al., 2009). These are freely drifting robotic floats (Hello & Nolet, 2020) designed primarily to autonomously detect (Sukhovich et al., 2011) and transmit (Hello et al., 2011) teleseismic *P* waves (Simon et al., 2020) for the purpose of conducting whole-Earth seismic tomography (Nolet et al., 2019, 2025; Simon et al., 2022). Over the years, they have revealed themselves to be useful for other purposes as well (Pipatprathanporn & Simons, 2022, 2024; Simon, Simons, & Irving, 2021; Sukhovich et al., 2015; Yu et al., 2023). The 24 instruments used in this study were deployed as part of the South Pacific Plume Imaging and Modeling (SPPIM) project (Hello, 2018) under the banner of the international EarthScope-Oceans consortium (www.earthscopeoceans.org). Their serendipitous proximity to HTHH, quantity, and quality make them a valuable new data source on this once-in-a-lifetime event, while holding the continued promise of increasing coverage globally.

As a "known" source, the 15 January 2022 eruption sequence will help us understand how submarine volcanic events are being recorded by mobile marine sensors (Matsumoto et al., 2011) at the basin scale, for which there is no precedent. The hydroacoustic phase that contains information about HTHH is the *T* wave: a transient of ambient acoustic pressure that is generated either directly in the water column by the eruption, or after conversion at the rock-water interface. The phase is recorded in the ocean by hydrophones, again possibly after multiple interactions with the ocean surface and the solid Earth (Talandier & Okal, 1998).

From their earliest detection and labeling (as *Tertiary* arrivals) and correct identification (as hydroacoustic phases) on land seismometers (Tolstoy & Ewing, 1950) or on oceanic pressure sensors (Norris & Johnson, 1969), whether from earthquakes, earthquakes associated with volcanism, or from volcanic sources (Kibblewhite, 1966), it has been clear that ocean-bottom interactions play a major role in determining transmission fidelity. Figure 1 makes clear that the data collected for this study traversed a great variety of bathymetric environments on their way from HTHH to the receivers, and that propagation effects may be largely responsible for reshaping and attenuating the signal received.

To characterize the relationship between the seafloor and the signal, we construct an algorithm to count bathymetric highs impinging upon the first-Fresnel zone of the *T* wave. From there we are able to understand signal variability, in particular in shape and total energy, of *T* waves produced by the HTHH eruption. Accounting for epicentral distance, we argue that the main factor driving signal differences across a large-aperture hydroacoustic array is a path-propagation effect, namely, how underwater sound waves interact with oceanic bathymetry.

2. Instrumentation, Data, and Waveform Analysis

MERMAID is primarily designed to return minutes-long segments of data that contain earthquake arrivals from distant seismic events. To understand the full range of signals received from HTHH, immediately after the event,

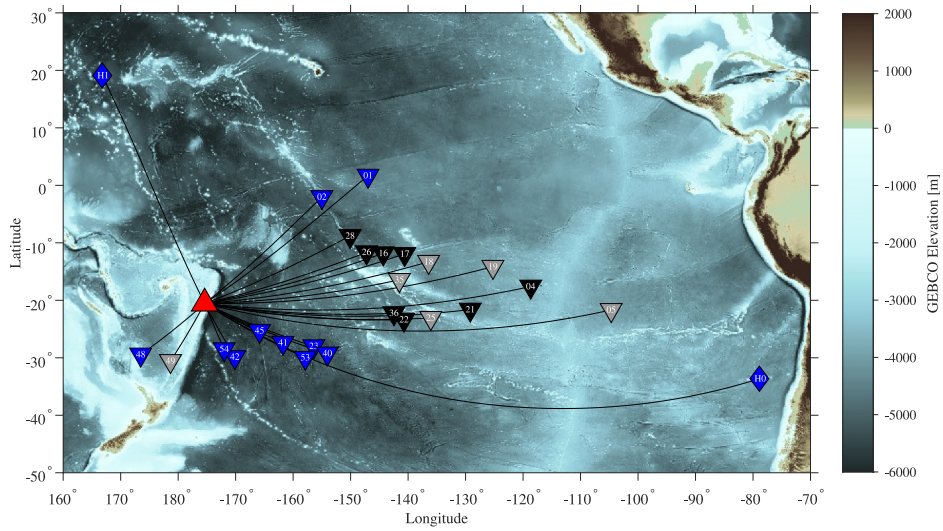

Figure 1. Hydroacoustic receivers used in this study to detect the 15 January 2022 Hunga Tonga-Hunga Ha'apai (HTHH) volcanic eruption (red triangle). Mobile Earthquake Recorder in Marine Areas by Independent Divers instruments are represented by triangles numbered with their station suffix, and International Monitoring System triad pairs are marked by diamonds labeled by station prefix. Colors denote our categorization of the *T*-wave signal received from the main HTHH eruption: A ("well defined") in blue, B ("diffuse") in black, and C ("undetected") in gray (see Figure 2). Great-circle paths connecting HTHH to each receiver are drawn as black lines overlain on map of bathymetry and topography from GEBCO (Weatherall et al., 2015).

we began directly requesting MERMAID buffer data from all instruments operating in the Pacific, via IRIDIUM satellite communication, supplementing them with data available from the IMS. As our timing and location reference we use the United States Geological Survey (USGS) event `us7000gc8r` with an origin time, t_0, of 04:14:45 UTC on 15 January 2022, located at 20.546°S, 175.390°W and 0 km depth. We begin our analysis by classifying the data based on visual inspection of the time series containing the arrival of waves traveling at the non-dispersive acoustic wave speed in water, counting from the time of the HTHH eruption.

2.1. Mobile Marine Sensors and Tethered Hydroacoustic Stations

As MERMAIDS drift freely with the ocean currents, they record data at parking depths (in this study) between 500 and 1,500 m (accurate to within ∼50 m), out of GPS range. Location at the time of recording is interpolated between multiple surfacings (Joubert et al., 2016) using `automaid` (Simon, Bonnieux, et al., 2021). MERMAID latitudes and longitudes in Table S1 in Supporting Information S1 are given to three decimal places (approximately 100 m), which is within the same order-of-magnitude range for the average location errors derived for MERMAID by Nolet et al. (2024) and sufficient for the purpose of this study.

IMS stations are moored (Oliveira et al., 2025; Pulli & Upton, 2002), and may be better located than our MERMAIDS, via acoustic ranging (e.g., Harben et al., 1999). Each IMS installation comprises two hydrophone triads, spaced 40–140 km apart in a north-south configuration, with sensors individually spaced about 2 km apart within each triad. Individual receiver locations are given in Tables S1 and S2 in Supporting Information S1. At the time of the eruption H03N3 was malfunctioning, so the two diamonds together in Figure 1 represent 11 closely spaced hydrophones.

2.2. The Data Set

MERMAID waveforms were requested via two-way IRIDIUM satellite communication in 30-min segments, with 5 s overlap, of 20 and 40 Hz sampled data, and stitched together using the `merge` command in the `SAC` software (Goldstein et al., 2003; Helffrich et al., 2013). The resulting MERMAID traces used in this study all start at least 14.9 min before the first *P* wave, as computed in the `ak135` model (Kennett et al., 1995), and end at least 58.9 min after the predicted *T* wave. The common Nyquist frequency of all MERMAID data presented in this paper is 10 Hz. Any data gaps were filled using piecewise cubic interpolation. We removed the mean and linear trend

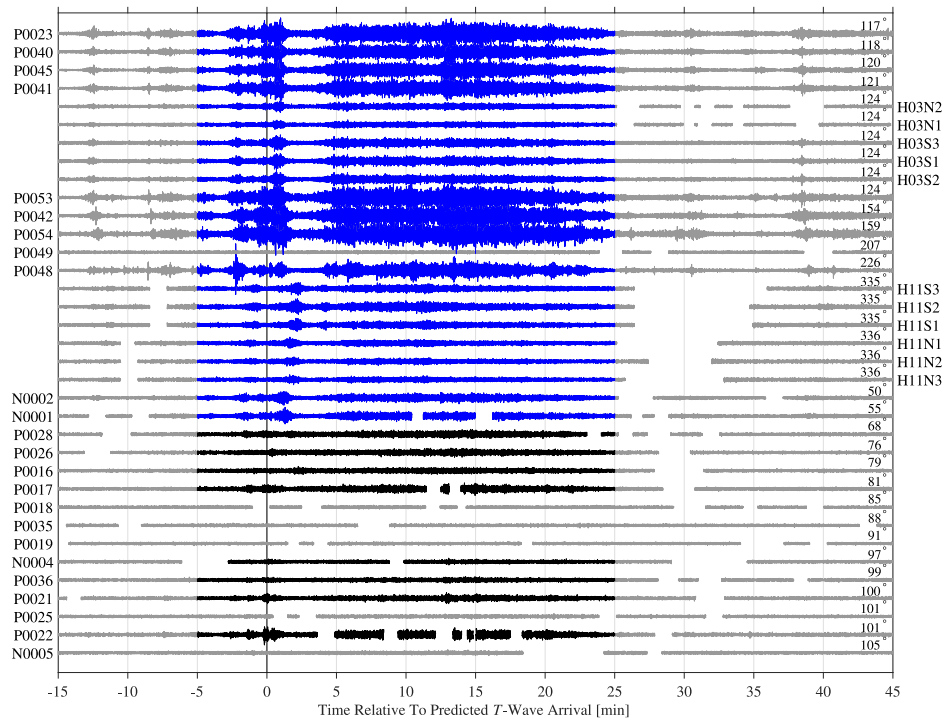

Figure 2. Hydroacoustic records of HTHH recorded by Mobile Earthquake Recorder in Marine Areas by Independent Divers floats (outside left labels) and International Monitoring System stations (outside right labels), normalized for visual clarity, with local events removed. Waveforms are ordered from top to bottom by azimuth (inside right label) clockwise from P0023. Timing is relative to the predicted arrival time of a 1.48 km/s wave originating from USGS event `us7000gc8r`. Colors denote signal category as in Figure 1.

and applied a `SAC` default `taper` prior to instrument-response removal following Burky et al. (2021), with corner frequencies [0.2, 0.4, 10, 19.8] Hz, and poles and zeros from Simon et al. (2022), which yielded time series of pressure (in Pa).

IMS data were retrieved from the virtual Data Exploitation Centre (vDEC) system (Gibbons, 2022), with sampling frequencies initially at 250 Hz. The mean and linear trend were removed, and the data tapered using `SAC` defaults. The instrument response was removed by the `SAC transfer` command within the corner frequency limits [0.1, 0.5, 100, 115] Hz, which yielded time series of pressure (in Pa).

Unless noted otherwise, all hydroacoustic records analyzed in this study were band-pass filtered using a one-pass four-pole Butterworth filter within the 2.5–10 Hz frequency band. In each trace we focus on a segment that begins 5 min before and ends 25 min after the expected first-arriving HTHH acoustic phase, which we term the "30-min *T* wave."

2.3. Time-Domain Analysis

We introduce t_T as the time of the expected first arrival at each station of a pure *T* wave emanating from HTHH and traveling horizontally at the non-dispersive acoustic wave speed in water of 1.48 km/s. No adjustments were made to t_T to account for higher-speed (e.g., body) wave propagation to a potential *T*-wave conversion point away from HTHH (i.e., along the trench for stations to the east).

Figure 2 is a record section of our data set for all of the 24 Mermaids and 11 IMS hydrophones from which we recovered data. Signals that we judged to arise from events local to a receiver and unrelated to HTHH were removed, leaving white-filled gaps in the waveforms. We took a very conservative approach whereby signals within our 30-min time windows of interest were only removed if their amplitudes exceeded the biggest *T*-wave pulses around those expected arrival times, and if they did not appear at other Mermaid or IMS receivers with moveout times that could be linked to HTHH. See also Figure S1 in Supporting Information S1 for a version of

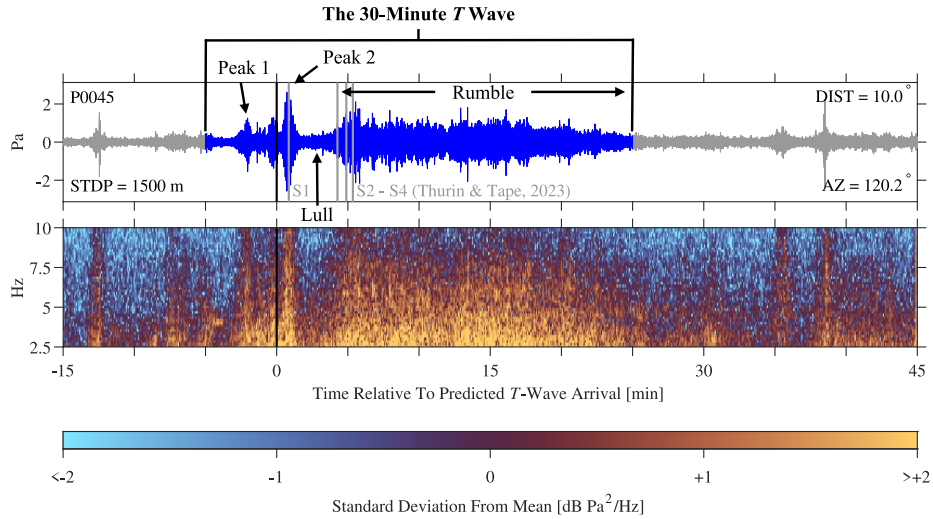

Figure 3. Time-domain and time-frequency behavior of the hydroacoustic signature of the HTHH eruption, illustrated with the record from Mobile Earthquake Recorder in Marine Areas by Independent Divers float P0045. This record demonstrates the defining features of all Category A signals: two clear arrivals around the expected *T*-wave time, t_T. They are separated by a minutes-long lull and followed by a long-duration "rumble." The corners of the upper panel show, clockwise from top left, the receiver name, epicentral distance, azimuth from HTHH, and station depth. The light gray lines S1–4 correspond to predicted *T*-wave arrivals from the four subevents identified by Thurin and Tape (2023). The spectrogram reveals strong and sustained HTHH signal at frequencies up to the 10 Hz Nyquist.

Figure 2 with stations reordered by epicentral distance, and Figure S2 in Supporting Information S1 for an expanded record section that retains local events and is timed relative to the eruption.

For context, Figure 2 shows 60-min traces, though for the remainder of the paper we focus on the 30-min *T* wave colored here, and in all subsequent figures, according to our subjective classification of signal quality: well defined (Category A), diffuse (Category B), or undetected (Category C), with blue and black highlighting the presence of clear *T* waves, and gray traces denoting waveforms with no discernible signal. By ignoring distance and instead plotting against direction from the source, Figure 2 visually suggests a relation exists between signal quality and propagation path. Stations that recorded Category B and C traces are generally clustered within a narrow azimuthal range to the east of HTHH (and bottom of Figure 2), while Category A signals left the source along relatively more northern and southern paths, see Figure 1.

Time-slowness analysis and vespagrams (Davies et al., 1971) that prove the dominant energy in our data set are *T* waves originating from HTHH may be found in Supporting Information S1 (Section S1 and Figure S3).

2.4. Time-Frequency Analysis

To understand the hydroacoustic signature of the HTHH eruption we focus on an hour-long record from MERMAID P0045, which recorded the loudest *T* wave in our data set. Figure 3 shows its time-domain (referenced to t_T) and time-frequency behavior. The bottom panel shows the spectrogram within the band-pass of the panel above, constructed using 6 s-long sliding windows with 70% overlap.

Our annotations in black text on the time-domain signal in Figure 3 first identify two distinct "peaks" that are major diagnostic features of what we label as Category A signals across our data set. The first peak reaches its maximum around 2 min before the expected *T*-wave arrival time, and the second peak is maximal some 45 s after t_T. This relative delay between what we label as "peak 1" and "peak 2" varies (see Figure 2). Additional energy arriving between those initial bursts adds complexity to this overall picture. However, these two peaks stand out prominently in the time series for the majority of our receivers. Next we call out a nearly two-minute "lull" separating those initial peaks from a long and energetic arrival, which we describe as a "rumble." The latter emerges more gradually than either of the preceding peaks, but it does eventually ramp up to an amplitude similar to, or in some cases exceeding, that of the two initial pulses.

Also labeled in the time domain in Figure 3, with gray vertical lines, are S1 through S4, which correspond to the timings of four subevents identified and named by Thurin and Tape (2023). Those times are based on a best-fit force model that used lower-frequency *P*-wave data as input. Our own "peak 2" aligns with the onset time of their S1; what we call the "lull" matches the time gap between their first and second subevents S1 and S2; and the buildup of our "rumble" overlaps with the rapid succession of onset times of their subevents S2–S4. The spectrogram, however, does show the strong and sustained energy between what we label "peak 1" and "peak 2," implying a timing mismatch with respect to a *T* wave propagating with reference to the USGS origin time. Near-source or near-receiver interactions, multipathing, and bathymetric or sound-speed refraction (e.g., Heaney et al., 1991, 2017; Oliveira et al., 2021; Talandier & Okal, 1998) all could help explain such timing differences. For example, if the signal left HTHH as a relatively faster *P* wave that was subsequently converted to a slower *T* wave at the Kermadec-Tonga trench, the predicted arrival times in Figure 3 could shift left (relatively earlier) on the order of ∼1 min (see Section S2 in Supporting Information S1). This could potentially align S1 of Thurin and Tape (2023) with an intermediate peak between what we label "peak 1" and "peak 2." However, similar reasoning cannot explain the 3 min shift that would be required to align S1 of Thurin and Tape (2023) with our "peak 1." Therefore, interpreting our "peak 2" to be the first subevent of the HTHH eruption as identified by Thurin and Tape (2023) using body waves implies alternatively that what we labeled "peak 1" may be generated by earthquake foreshocks or other activity (e.g., small/partial explosions, tremor bursts), as have been reported around another eruption (in March 2009, by Bohnenstiehl et al., 2013). In summary, HTHH may have kicked off in earnest a few minutes earlier than reported by the USGS.

The hypothesis of an earlier eruption time compared to the USGS origin is bolstered by a signal in the spectrogram of Figure 3 that begins about 6 min before t_T. There we see what we interpret to be a precursory "glide" (Tepp & Haney, 2019), a tremor whose frequency changes with time, climbing in frequency before settling around 4 Hz as a monochromatic tremor that persists for about 1 min. After a pause of around another minute the eruption seemingly kicks into full swing and we see the arrival of "peak 1" coming in at 2 min before t_T. Glides that immediately precede eruptions are often interpreted as a sign of magma migration or pressure building in a resonant conduit (Tepp & Dziak, 2021). A similar series of events including a (6–10 Hz) glide and brief (1 min) pause before the main eruption was also identified for the May 2010 eruption of the South Sarigan submarine volcano (Green et al., 2013; Searcy, 2013). Figure S4 in Supporting Information S1 provides an enlarged image of this precursory signal.

To further appreciate the richness of the hydroacoustic record documenting HTHH we show, in the left column of Figure 4, a collection of time-domain and time-frequency plots, in the same format as in Figure 3 but with reduced annotation. Three more examples of Category A signals are shown. As argued, their defining feature is the clear expression of two separate time-domain peaks, followed by a lull and then a rumble. The first two examples lie along approximately the same azimuth from HTHH as P0045, shown earlier, and see Figure 1. The third example, in the lightest blue, is from an entirely different azimuth. One Category B signal that lacks that clear expression, and which is more diffuse, smoothed, and subdued, and one Category C example spanning the same relative time window but without discernible recorded activity, round out the set.

2.5. Envelopes and Cross-Correlation Analysis

Category A and B signals as shown in Figure 3 and the left column of Figure 4, reveal consistent and recognizable features and an overall similar structure that we should like to quantify. To this end we compute cross-correlations between their 30-min *T*-wave envelopes, displayed in right column of Figure 4. There are two signal envelopes in each panel, with the lower one mirrored about the horizontal axis for visual clarity. The top curve in each panel is the 30 s sliding root mean square (RMS) envelope of the waveform in the left column. The blue curve in the bottom of every panel is the similarly constructed envelope for Mermaid float P0045 (Figure 3). Mermaid and IMS data were decimated to 10 Hz sampling before cross-correlation.

As we are only interested in the shape similarity of the waveforms, the envelopes are normalized and thus amplitudes cannot be compared. Time gaps corresponding to local events left blank in Figure 1 were replaced by the average of the envelope in the minute before and after the relevant interval. The horizontal axis in all panels of the right column is relative to t_T for Mermaid float P0045, marked by a blue vertical line in the bottom half of every panel. The corresponding predicted arrival time for the correlating receiver in the top half of each panel is marked by a vertical line in the appropriate color.

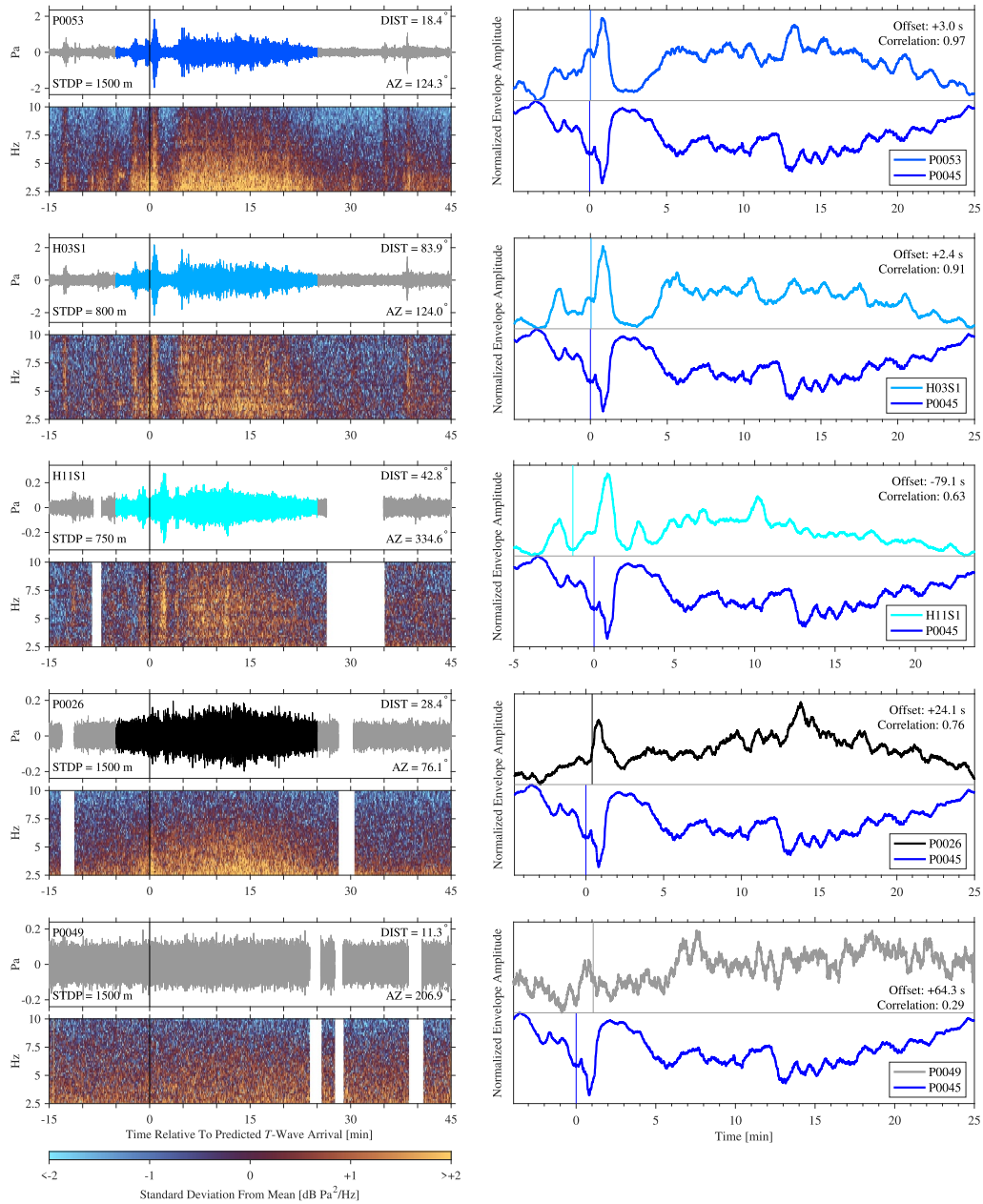

Figure 4. (Left column) Time-domain and time-frequency renditions of three Category A (blue shades; well-defined features), and one each of Category B (black; diffuse) and Category C (gray; no detectable signal), plotted relative to their predicted *T*-wave arrival times, t_T, marked by vertical lines. (Right column) Envelopes of the corresponding records shown in the left column (top curve in each panel), and from Mobile Earthquake Recorder in Marine Areas by Independent Divers float P0045 (Figure 3; bottom blue curve, and flipped upside down). Vertical lines mark t_T relative to each envelope, and their offsets and corresponding correlation coefficients are quoted within each panel.

The cross-correlations were carried out after an initial examination of the waveforms focused on a five-minute window around t_T. Waveform envelopes were then shifted to effectively align on the main eruptive pulse, labeled "peak 2" in Figure 3. In Figure 4, the time shift ("offset") between respective t_T (vertical lines) required to align on the main pulse, and the resulting correlation coefficient, is shown within each panel. We preferred aligning on the main peak, as allowing for arbitrary lags produced preferential alignment of maxima within the rumble at the expense of misaligning the main pulse and subsequent lull, especially for Category B signals; for example, the black envelope of P0026 in Figure 4, whose global maximum is actually reached some 14 min after t_T. We note that the

29% correlation for the gray Category C P0049 envelope is a result of the sliding RMS function being a positive-valued lowpass operation, and does not imply the presence of actual, detectable signal in that trace.

A detailed timing analysis and comparison of the precise onset of the *T*-wave wavetrain between receivers is not our focus, though we do note the nearly 80 s signal advance required to align H11S1 and P0045 in Figure 4. Nearly 50 s of this timing difference can be explained by the first-order travel-time correction briefly discussed last section, which posited that the seismic energy started its journey toward P0045 as a (faster) *P* wave, only to be converted to a (slower) *T* wave at the Kermadec-Tonga trench, at around 100 km into its trajectory. Conversely, the near-source bathymetry for the path to H11S1 shows that *T*-wave energy could have been easily injected directly into the water column off the northwestern flank of HTHH, and therefore would have traveled at the *T*-wave velocity for a greater proportion of its path (see Section S2 and Figures S5 and S6 in Supporting Information S1).

Figure 4 shows how well correlated some 30-min *T*-wave envelopes are. The top panel shows that receivers P0045 and P0053 are 97% correlated. The next panel below that P0045 and H03S1, whose paths lie at nearly the same azimuth from HTHH, are still 91% correlated despite the *T* wave completing a nearly 90 min and 8,000 km journey between those two stations.

We have demonstrated that waveforms recorded by MERMAID and IMS hydrophones are often very highly correlated, even when their traces appear noisy or diffuse at first glance. However our envelope cross-correlations provide crude measures at best. For example, H11S1 remains 63% correlated with P0045 despite showing significant differences in the time-domain waveforms throughout, while P0026 is 76% correlated with P0045 despite the former not showing any sharp arrivals. When computing correlation coefficients on the entire 30-min wavetrains, the highly correlated and long-duration rumble appears to outweigh any cross-correlation gains or losses that may depend on the presence or absence of the two initial peaks.

2.6. Path Bathymetric Effects

Interpreting differences in HTHH signal expression at different stations simply in terms of their azimuth or distance from the source is unsatisfactory, and from the data shown, it is unclear how to explain them by pure source effects, although these might include anisotropic and directed mechanisms of energy release (Thurin & Tape, 2023; Zheng et al., 2023) or conversion (Piserchia et al., 1998). As to the receivers, their identical instrumentation (for all MERMAID floats and among all IMS stations) and free placement in the water column do not afford much interpretative wiggle room.

What then explains the presence of different signal reception categories, and what is the possible source of the sometimes strong similarities, and sometimes stark differences, between them? We pivot toward a quantitative description of propagation effects along the hydroacoustic travel path, augmented by considerations of the ambient noise field in the vicinity of the receivers.

Our basic premise is that when seeking to explain signal quality and quantity originating from a known isotropic *T*-wave source and propagating in a dominantly vertically stratified ocean, distance effects arising from geometrical spreading can be approximately accounted for. After that, our main task is to quantify seafloor interactions along the propagation path, which we conceptualize as chiefly leading to signal transmission loss, neglecting possible gains (e.g., De Caro et al., 2021).

3. Methods

We are interested in quantifying the effect of bathymetric occlusion on various signal characteristics. By "occlusion" we mean obstacles (guyots, seamounts, ocean islands, and mid-ocean ridges, etc.) encountered by the *T* wave during propagation from source to receiver. To define "encounter" we must discuss what a *T* wave "feels" during propagation from source to receiver; that is, we must characterize the geographic region that encapsulates the likely volume within which bathymetric features may act to reduce propagation efficiency.

3.1. Depth of Influence: The Fundamental Mode

T-wave propagation along a presumed great-circle path is influenced by the depth to the ocean bottom and modulated by the sound speed which is dominantly varying as a function of depth below the ocean surface.

Table 1
Maximum Fresnel Radii, $F_1(R/2)$ (Equation 1 at the Path Midpoint), of Sound Waves Traveling at a Nominal c = 1.48 km/s, at Various Frequencies (f), Recorded at Different Stations

Receiver	2.5 Hz	5.0 Hz	7.5 Hz	10.0 Hz
P0054	12 km	8 km	7 km	6 km
P0021	27 km	19 km	15 km	13 km
H03N1	37 km	26 km	22 km	19 km

Whether we take a ray-theoretical or a modes-based viewpoint (Heaney et al., 1991, 2017; Okal, 2008), the bulk of the energy transport is explained by the presence of the oceanic low-velocity zone: the SOund Fixing And Ranging (SOFAR) channel. This channel acts as a horizontal waveguide in the ocean that traps and focuses acoustic energy (Ewing & Worzel, 1948). In deeper waters, a well-expressed SOFAR channel allows *T* waves to efficiently propagate across vast distances with minimal attenuation from lossy interactions with the abyssal seafloor.

Generally, at low- to mid-latitudes, the SOFAR channel is well expressed in the upper 3,000 m of the ocean (Munk, 1974), though its actual structure and depth extent vary with latitude and season (Forget et al., 2015). Oceanic temperature and salinity profile together control the sound speed (Del Grosso, 1974; McDougall & Barker, 2011; Millero & Li, 1994; Roquet et al., 2015). In high latitudes the axis may even shoal to the surface (Johnson & Norris, 1968; Northrop & Colborn, 1974). Figure S7 in Supporting Information S1 shows a profile through ocean sound-speed model GDEM-V 3.0 (Carnes, 2009) in our study area.

Figure 3 displays frequencies above 2.5 Hz, where we observe the acoustic fundamental mode. At the frequencies used in our study, the majority of *T* wave energy resides in the fundamental mode, and less is partitioned among higher modes that are more prone to attenuation due to their interaction with the seafloor (de Groot-Hedlin & Orcutt, 2001). In Section S3 in Supporting Information S1 we discuss fundamental-mode pressure eigenfunctions (Dziewoński & Anderson, 1981; Porter, 1992) derived for specific ocean depths at individual receiver locations, and for average depths (Amante & Eakins, 2009) in the regions around them. Ocean depths averaged along every propagation path yield 2.5 Hz fundamental acoustic pressure mode eigenfunctions whose maxima cluster tightly around 1,350 m depth. Eigenfunctions for near-receiver regional average-ocean depths for all 29 stations that recorded Category A and B signals also reach their maxima around 1,350 m. Since no meaningful differences in regionally averaged ocean-depth mode shapes or amplitudes exist between any of our receivers (Figures S8 and S9 in Supporting Information S1), we will maintain a single depth of 1,350 m as the dominant depth of *T*-phase propagation when counting occlusions, as detailed next.

We choose not to individually correct signal amplitudes based on ocean-depth eigensolutions computed at the receiver, as we lack the ability to model the path-dependent mode-transmission coupling properties required for meaningful scaling of mode amplitudes.

3.2. Width of Influence: The Fresnel Zone

Having considered the dominant sensitivity of fundamental-mode *T*-wave propagation with depth in order to develop a scheme to quantify bathymetric blockage that may help explain signal loss, we now turn to the lateral dimension to establish the horizontal extent of the region within which *T* waves may propagate between the source and receiver, that is, the three-dimensional Fresnel volume (Červený & Soares, 1992). We desire a rule of thumb to understand the width of the Fresnel zone around the dominant path at depth.

For an acoustic wave of frequency f propagating in a medium with phase speed c, the first Fresnel zone, modeled around the geometrical ray, has a radius F_1 that depends approximately on the distance r from the source as (e.g., Baig et al., 2003; Skarsoulis & Cornuelle, 2004; Spetzler & Snieder, 2001),

$$F_1(r) = \sqrt{\frac{r(R-r)}{R}\frac{c}{f}} = \sqrt{\frac{r(R-r)}{R}\lambda}, \tag{1}$$

whereby R is the entire distance from source to receiver, and λ the wavelength. For context and intuition, Table 1 lists maximum Fresnel radii for three representative stations at frequencies ranging from 2.5 to 10 Hz. In this study we count occluders exclusively within the broadest 2.5 Hz Fresnel zone in order to capture the full extent of seafloor interactions affecting our *T* waves.

We computed great-circle tracks between the source and every receiver, and Fresnel radii using Equation 1 for every point along those paths. Drawn perpendicularly to the great-circle path in the horizontal plane, bathymetry within this two-dimensional area was sampled from the GEBCO_2014 bathymetry model (Weatherall et al.,

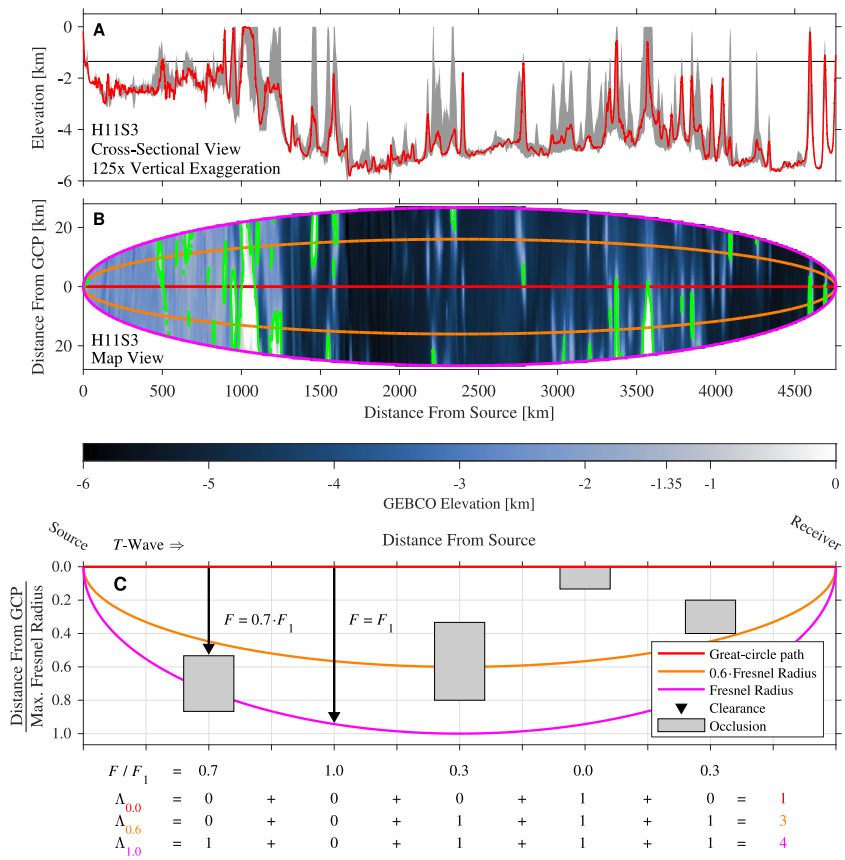

Figure 5. Counting bathymetric occlusion along the *T*-wave propagation path. (a) Cross-section with great-circle bathymetric profile (red) and bathymetry range within the 2.5 Hz *T*-wave Fresnel zone (gray) between HTHH and International Monitoring System station H11S3. The black line at 1,350 m marks the depth of the maximum of the fundamental-mode pressure eigensolution broadly applicable to all of the propagation paths in this study. In map view, (b) shows the edges (magenta) of the first Fresnel zone, within which we render oceanic bathymetry. The direct path is shown in red, and the orange lines bound the zone defined by the 0.6 clearance ratio. Green contours encircle bathymetric regions shallower than 1,350 m, which we count as occluders. Our counting algorithm is schematically illustrated in (c), which shows one half of the symmetric Fresnel zone using the same colors as in (b) to mark clearance ratios $F(r,z)/F_1(r)$. Bathymetric occluders are drawn generically as gray rectangles, and the clearances at two points on the great circle path are marked by black vertical arrows. Clearance ratios are listed below the figure panel at their corresponding position. Note that the clearance ratio and the vertical figure coordinate have different denominators except at the path midpoint. The lowermost three lines exemplify the total occlusion counts Λ_Φ of Equation 4, for $\Phi = 0$, 0.6, and 1.0, and their individual contributions from each of the four obstacles.

2015) with an equal-area discretization in latitude and longitude commensurate with that model, which is available at a resolution of 30 arc-s (about 900 m at the equator and roughly half that length at 60° latitude). We chose a Fresnel-zone grid with 600 m spacing, resulting in each grid cell being sampled roughly once by a 2.5 Hz *T* wave propagating at the nominal acoustic sound speed of 1.48 km/s.

At nearly 34°S, H03S2 is the highest-latitude station in our set, where the GEBCO grid is smallest at ~770 m, while at N0001, the station nearest the equator, it is ~926 m. For all latitudes in our study, the bathymetry grid is larger than a single wavelength of the 2.5 Hz *T* waves of interest, resulting in our model oversampling occluders along all paths. Hence, while we are oversampling the GEBCO model, we are doing so on an equal-area grid.

3.3. Counting and Accounting for Bathymetric Occlusion

In our simplified treatment the *T* wave propagates along a great circle at the depth of the maximum of the pressure eigenfunction of the fundamental acoustic mode for the average ocean depth and sound speed structure along the path, and within a lateral zone of influence defined by the width of the first Fresnel zone at the dominant 2.5 Hz frequency. We now count as obstacle any bathymetric feature that penetrates this two-dimensional area of

influence and devise a scheme to translate this number into a relative "occlusion factor" whose influence on signal amplitude we will attempt to quantify.

Figure 5a shows a bathymetric cross-section along the great-circle path between HTHH and IMS station H11S3 as a solid red line, with the gray shading encompassing the minimum and maximum elevations within the first Fresnel zone about the direct path, defined by $F_1(r)$ as given by Equation 1. In map view, Figure 5b, the first Fresnel zone is an ellipsoidal area bounded by the magenta curve. The direct path is represented by the red line. Also marked, in orange, is the area bounded by the zone defined by $0.6F_1(r)$ which, to cite Levis et al. (2010), is the zone outside of which (in radio wave theory, at least) it might be reasonable to ignore occlusions—a "clearance ratio" of 0.6 that must be maintained in order for signal attenuation to approximate "free-space loss," that is, attenuate due solely to geometrical spreading along an unobstructed path (Bullington, 1957; Maher et al., 2021). This 0.6 clearance ratio is often given as a rule-of-thumb minimum clearance in reference materials for telecommunications standards (Coleman & Westcott, 2021) because it provides a simple metric to determine, for example, how high above a tree line transmitters and receivers should be to maintain levels approximating free space. In other words, paths that see obstacles intruding more than 40% into the first Fresnel zone should be avoided to maintain signal integrity.

We define an occluder to be any bathymetric obstacle within the first Fresnel zone that has an elevation greater (depth shallower) than some test elevation of interest, z. We define clearance, $F(r,z)$, at some distance from the source, r, and for a test elevation, z, as the perpendicular distance from the direct path to the first occluder, on either side. We further define

$$F(r,z)\big/F_1(r) \tag{2}$$

to be the clearance ratio, with respect to the radius of the first Fresnel zone at that same location.

At every point r along the direct path from source to receiver, we search for possible occluders on either side of the direct ray, and, if any such occluders exist, we count,

$$O_\Phi(r,z) = \begin{cases} 1, & \text{if clearance ratio} < \Phi, \\ 0, & \text{otherwise.} \end{cases} \tag{3}$$

A single distance r can only contribute 1 to the count at a single test depth z, for a given test clearance ratio Φ. Our count makes no mention of the material properties of the seafloor or the shape of the occluder, it only asks whether an obstacle exists—or not. Note that Φ in Equation 3 is a fixed test clearance ratio used to specify the clear-path berth, to be distinguished from the actual clearance ratio $F(r,z)\big/F_1(r)$.

Our final occlusion count, $\Lambda_{\Phi,z}$, is the sum of all bathymetric obstacles at all distances from source to receiver,

$$\Lambda_{\Phi,z} = \sum_{r=0}^{R} O_\Phi(r,z), \tag{4}$$

where $z = 1{,}350$ m, that is, taken near the average depth of the maximum of the pressure eigenfunction for the average ocean depth and sound speed profile (as explained in Section 3.1). Figure 5c is a schematic of our counting algorithm.

Expressions that take into account a range of elevations,

$$\overline{\Lambda}_\Phi = \sum_{i=1}^{n} w_i \, \Lambda_{\Phi,z_i}, \tag{5}$$

where w_i are appropriately normalized weights, were tested for a variety of scenarios but proved to be more general than needed. For example, we tested weighting occluders based on fundamental-mode acoustic eigenfunctions (e.g., Figures S8 and S9 in Supporting Information S1) and found the added complexity did not result in performance gains. Alternative algorithms that properly weight based on occluder and receiver depths, and

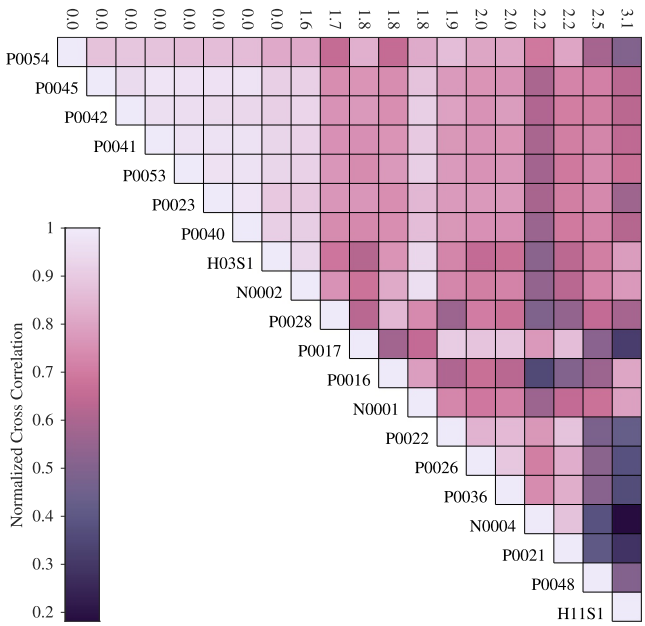

Figure 6. Correlation matrix ordered by occlusion count, from left to right and top to bottom. The number above each column is the logarithm of the occlusion count, $\Lambda_{1.0}$, see Equation 4, computed using the algorithm illustrated in Figure 5. A single sensor from each pair of moored hydrophone triads is included. Examples of envelope correlations are shown in the right column of Figure 4. The overall trend is one of progressive signal decorrelation with increased bathymetric occlusion.

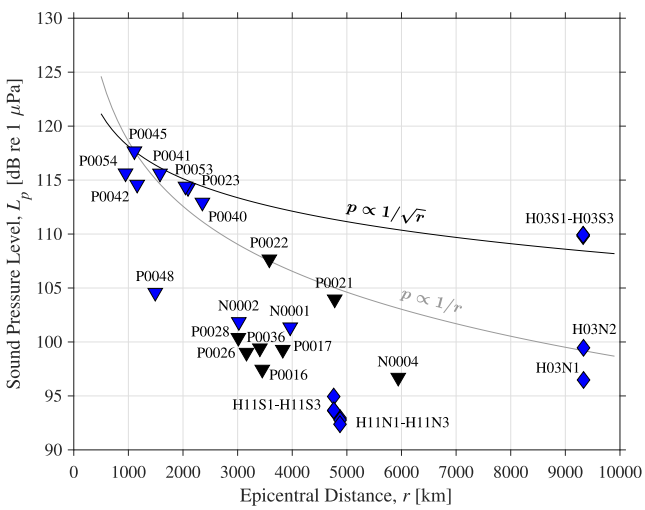

Figure 7. Sound pressure levels (SPL, Equation 6) as a function of distance for the 29 stations that recorded Category A and B signals, with cylindrical ($p \propto 1/\sqrt{r}$, Equation 7) and spherical ($p \propto 1/r$) geometric attenuation curves superimposed, relative to P0045. Signal losses for most receivers are greater than can be explained by distance considerations alone, revealing the importance of bathymetric path occlusion effects that sap the propagating signals of their energy.

additionally consider occluder contiguity and proximity to the great-circle path, remain alternatives that should be tested in the future.

Figures S10–S44 in Supporting Information S1 combine portions of Figures 3–5, displaying waveforms and spectrograms, and bathymetric cross-sections and maps, for all 35 sensors used in this study.

4. Results

In this section we explore to what extent correlation and amplitude differences between the hydroacoustic records presented in Section 2 are explained by path propagation effects as postulated in Section 2.6, for which Section 3 developed a quantitative formalism based on bathymetric occlusion. We focus on the relative shapes and sizes of signals we identified as belonging to Category A and B.

4.1. Bathymetric Occlusion and *T*-Wave Correlations

In the right column of Figure 4 we showcased individual examples of RMS envelope cross-correlations among and between Mermaid floats and IMS stations. Figure 6 shows identically computed pairwise correlations for all receivers reporting Category A and B signals (retaining only a single representative record from each IMS station), ordered, from left to right and from top to bottom, by occlusion count $\Lambda_{1.0}$ (Equation 4). Accounted for are all bathymetric obstacles within the full first Fresnel zone of 2.5 Hz hydroacoustic waves, for a reference depth of 1,350 m, as illustrated schematically by Figure 5. Float and station names are listed, as are the logarithms of the occlusion counts.

In the top left corner of Figure 6, a cluster of highly correlated signals corresponds to virtually unimpeded paths with very low occlusion counts. At the other extreme, in the bottom right corner of Figure 6 cluster stations that lie on highly occluded paths and are thus poorly correlated with other receivers.

The overall gradient, from highly to poorly correlated (light to dark purple), from left to right and from lower diagonal to upper right corner in the representation of Figure 6, is a first-order validation of the hypothesis that increasing bathymetric occlusion along the path progressively decorrelates the hydroacoustic record, although we remain mindful of the limitations linked to neglecting possible source anisotropy and energy conversion effects as mentioned in Section 2.6.

4.2. Bathymetric Occlusion and *T*-Wave Amplitudes

Having quantified the relative similarities among signal *shapes*, we now study how occlusion affects their *sizes*, that is, amplitudes.

For the 29 Category A and B signals that faithfully recorded the HTHH event, we explore the extent to which the presence and amount of bathymetric occlusion along the propagation path to the receiving Mermaid float or IMS station help explain lossy signal transmission with respect to unimpeded *T*-wave propagation, whose loss is presumed to be due solely to geometrical spreading with distance from the source. Intrinsic attenuation in seawater is known to be negligible (Pulli & Upton, 2002). For a discussion of how bathymetric occlusion relates to signal observability in general—e.g., considering Category C records, and the interplay between local noise environments, occlusion, and detectability—see Section S4 and Figures S45 and S46 in the Supporting Information.

We begin by defining sound pressure level (SPL) in water as

$$L_p = 20 \log_{10}\left(\frac{p}{p_0}\right), \tag{6}$$

in decibel (dB), where we take p to be the RMS acoustic pressure (in Pa), and p_0 the customary reference sound pressure of 1 μPa (Ainslie et al., 2022). Sound confined to propagating within the ocean layer spreads *cylindrically*, hence pressure, p, attenuates with distance, r, proportionally to $p \propto 1/\sqrt{r}$. In this case, pressures at two receivers located at r_1 and r_2 relate as $p_2 = \left(\sqrt{r_1}/\sqrt{r_2}\right)p_1$, which transforms Equation 6 into an SPL difference between them as,

$$L_{p_2} - L_{p_1} = 20 \log_{10}\left(\frac{\sqrt{r_1}}{\sqrt{r_2}}\right). \tag{7}$$

A more rapid fall-off of energy would be expected for geometrical attenuation controlled by *spherical* spreading, where the parenthetical term in Equation 7 is replaced by (r_1/r_2).

Figure 7 plots SPL measurements for all Category A and B records from Mermaid floats and IMS stations using all of the same data processing and graphical conventions adopted thus far. Superimposed are the cylindrical (Equation 7) and spherical (in gray, only for reference) SPL curves relative to Mermaid P0045, the largest signal in the set with its completely unoccluded propagation path. With the exception of the southern triad of receivers at IMS station H03, the majority of SPL values lie below those which would be expected from cylindrical geometrical spreading, that is, free-space loss, alone.

The difference between the relative lack of signal loss at the southern IMS hydrophones H03S1, H03S2, and H03S3, compared to the two functioning hydrophones of the northern array, H03N1 and H03N2, which show SPL losses between about 10 and 14 dB, is remarkable, given their 40 km geographical separation. Metz et al. (2018) noted a similar, albeit smaller, pattern of SPL difference between the H03 triads while studying volcanic signals originating from Monowai on the Kermadec trench, which is near the location of our presumed *T*-phase origin for the stations to the east of HTHH. In that case the northern hydrophones exhibited lower coherence and experienced 4–8 dB losses compared to their southern counterparts, a phenomenon that Metz et al. (2018) suggested may be due to differences in near-station bathymetric environments.

Indeed, those differences in bathymetry between the southern and northern IMS hydrophone triads provide direct evidence for which depths matter when counting occlusion. For example, in our propagation model, no path to any of the three hydrophones in the southern H03 triad includes bathymetry shallower than 1,429 m, just beyond the 1,350 m counting depth we chose. In those cases, *T* waves are seemingly unaffected by the seafloor, as evidenced by Figure 7 which shows their RMS pressures being recorded with losses predicted by free-space propagation. Adjusted for epicentral distance, H03S1 records the largest *T* wave in our set. On the other hand, the corridor from HTHH to the northern H03 triad is punctured by bathymetry that rises essentially to the surface. The logarithmic occlusion counts at those sensors are 1.6 and 1.7.

We can now explain the quantitative departure of sound pressure levels from the $p \propto 1/\sqrt{r}$ free-space geometrical spreading trend in Figure 7, for a common source presumed to be isotropic, and recalling that we forgo attempting a station-depth correction due to the fundamental-mode arguments put forward in Section 3.1. Removing the effect of geometrical spreading from our pressure measurements following the cylindrical free-space proportionality allows us to define an adjusted RMS pressure, $p_r^* = p\sqrt{r}$, whose substitution into Equation 6 gives the adjusted SPL,

$$L_{p^*} = 20 \log_{10}\left(\frac{p^*}{p_0}\right). \tag{8}$$

In Figure 8 we show the relationship between L_{p^*}, the free-space adjusted SPL of Equation 8, and the occlusion count, Λ_Φ, defined in Equation 4, for various values of the test clearance ratio Φ, the fractional width of the zone

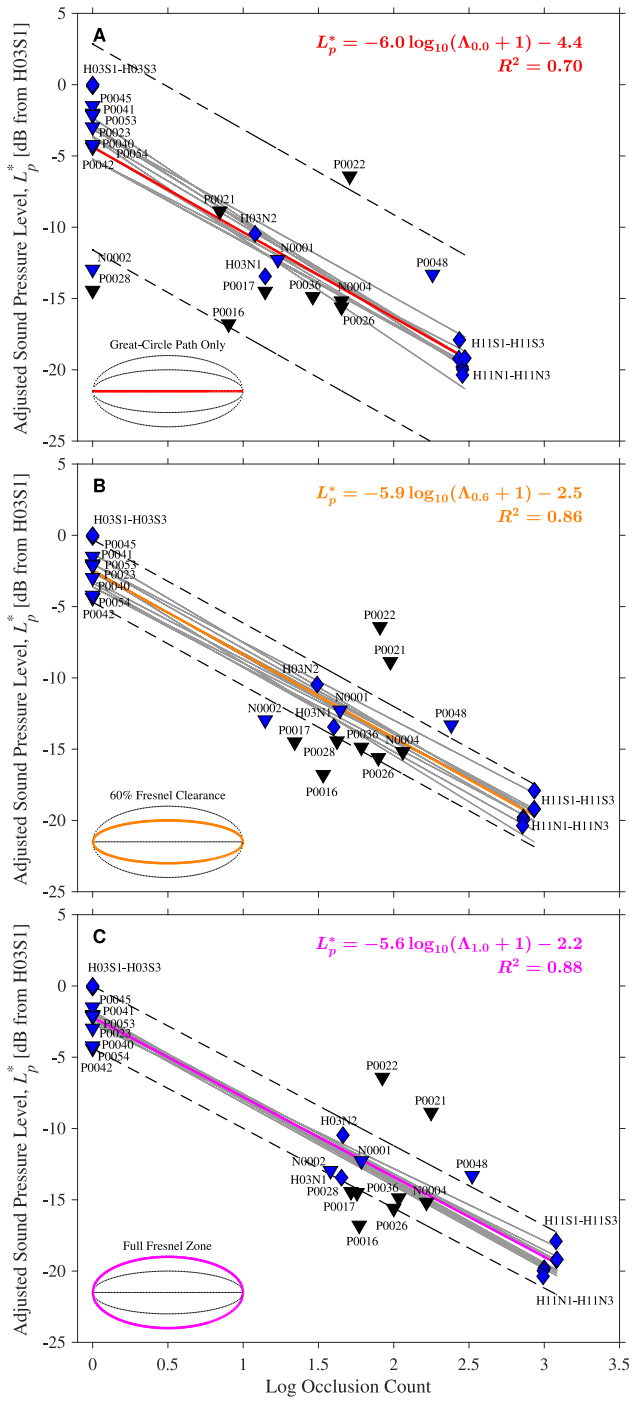

Figure 8. Adjusted sound pressure levels (Equation 8) relative to the maximum of the set (H03S1) as a function of occlusion count Λ_Φ computed for different test clearance ratios: $\Phi = 0.0$ (a), $\Phi = 0.6$ (b), and $\Phi = 1.0$ (c). In each panel a line plots the best-fitting linear regression model (Equation 9) for the 29 stations recording Category A and B signals, colored to represent the clearance ratio whose counting domain is illustrated by the Fresnel-zone diagram inset in the lower left corner and explained in Figure 5. Best-fitting model parameters and the corresponding coefficient of determination, R^2, values are provided. Gray lines plot a random sample of 10 from a set of 1,000 bootstrapped regressions obtained via resampling with replacement (Efron & Tibshirani, 1994). Dashed black lines are plotted with slopes equal to the colored best-fit data line but offset above and below it by half the range of the adjusted SPL values recorded by stations with zero path occlusion.

relative to the width of the first Fresnel zone. This figure demonstrates the influence of counting bathymetric obstacles as occluders within this zone, as detailed in Section 3, leading to signal transmission loss and diminished *T*-wave amplitude after correcting for propagation distance. For the 29 stations that recorded HTHH *T* waves shown in Figure 7, the relationship appears to be linear, as follows,

$$L_{p^*} \propto \log_{10}(\Lambda_\Phi + 1), \tag{9}$$

where the +1 on the right-hand-side of Equation 9 protects against the cases when the occlusion count is identically zero.

From top to bottom, the three panels of Figure 8 plot the adjusted SPL (in dB relative to the maximum of the set, H03S1) against occlusion counts Λ_Φ for $\Phi = 0$, $\Phi = 0.6$, and $\Phi = 1$; that is, Figure 8a only considers obstacles that directly impede the direct great-circle path at 1,350 m depth, Figure 8b expands the bathymetric search to include all occluders within the 0.6 Fresnel-zone clearance ratio, and Figure 8c unfurls the dragnet to catch all seafloor interactions within the full width of the first Fresnel zone.

As the panels in Figure 8 have now fully removed (cylindrically spreading) distance and (bathymetrically occluded) path effects, differences in *T*-wave amplitudes that remain might be attributable to differences in recording depth and azimuthal inhomogeneities in the source. To appreciate any possible variability due to source effects, dashed lines are plotted with the same slope as the solid regression line, offset above and below it by one-half the spread of the zero-occlusion adjusted SPL values.

4.3. Analysis

A simple line count of bathymetric interactions along the source-receiver great-circle path of a propagating *T* wave explains 70% of the variance of sound pressure level losses adjusted for free-space geometrical spreading. The outliers in Figure 8a show that the count along the great-circle path alone, $\Lambda_{0.0}$, is likely most useful as a bulk estimate across large-aperture arrays and may be insufficient to estimate signal losses along narrow corridors or at single stations. Even with this most restrictive occlusion count, Figure 8a explains the discrepancy in SPL recorded by the northern and southern H03 triads identified in Figure 7. Adjusted for distance and plotted against occlusion count it is clear that the southern hydrophones recorded louder *T* waves because of their unoccluded paths, while the northern hydrophones heard a relatively quieter HTHH eruption due to bathymetric occlusion. For the majority of their ~9,300 km paths, the Fresnel zones of these closely collocated stations overlap, implying the difference in bathymetric environments is confined to a region very near the receiver, as apparent from Figures S40–S44 in Supporting Information S1.

Figure 8b broadens the geographic domain of the occlusion count to consider 60% of the first Fresnel-zone width. The resulting model predicts losses of 5.9 dB with the logarithm of occlusion count, $\Lambda_{0.6}$, and explains 86% of the data variance. The greatly improved goodness-of-fit is partially the result of the disappearance of the most egregious outliers in Figure 8a, notably Mermaid floats N0002 and P0028, which lie along unobstructed great-circle paths with zero occlusion in Figure 8a, but in Figure 8b reveal themselves to be much more occluded when the obstacle search is expanded off the direct path. This supports the motivation for considering at least some portion of the Fresnel zone to accurately gauge path effects when modeling transmission loss. Conversely, the fit is worse for receiver P0021 when considering a broader Fresnel zone. We speculate this is due in part to the geographic distribution of occluders (mainly clustered within the lower half of the symmetric Fresnel zone, see Figure S33 in Supporting Information S1), which our algorithm does not take into account.

Finally, Figure 8c widens the domain of the occlusion search to the entire Fresnel zone, with the occlusion count $\Lambda_{1.0}$ identifying the most path obstacles. The linear model records the highest goodness-of-fit, $R^2 = 0.88$, and the best-fit regression line is in very close agreement with the average of the bootstrap-resampled models. In other words, this final model, which predicts a 5.6 dB loss in adjusted sound pressure level per logarithm of the full-Fresnel occlusion count, is highly stable, and also highly significant, with the probability of spuriously recording such a high correlation vanishingly small (with a *p*-value on the order of 10^{-14}).

The clearance ratio of $\Phi = 0.6$ analyzed in Figure 8b validates the nearly 70-year old rule-of-thumb discussed in Section 3.3 which theorizes that signal attenuation approximating free-space losses may be obtained by keeping the innermost 60% of the first-Fresnel-zone completely clear of obstacles. Additionally, a comparision

of Figures 8b and 8c shows that very little additional model strength is gained by expanding the counting region to include the outer 40% of the full Fresnel radius—a second proof, independent of the concept of free-space loss, that obstacles within this most important inner volume of the Fresnel zone have the most effect on *T*-wave attenuation. In fact, Table S3 in Supporting Information S1, which provides model performance for Φ between 0.0 and 1.0, shows that greater than 90% of the model performance relative to $\Phi = 1.0$ is achieved at an even narrower clearance ratio of $\Phi = 0.4$. This has implications for signal detectability and correlation, important factors in, for example, seismic ocean thermometry (Wu et al., 2020, 2023; Zheng et al., 2023).

5. Discussion

Understanding physical processes of the solid Earth as recorded in the ocean requires comprehending signal transmission, the influence of a *T*-wave path from generation to detection, and how the structure of the ocean floor along the path—or across an array—shapes what can be observed on hydrophones.

Adjusted for free-space losses, that is, corrected for cylindrical geometrical spreading, bathymetric occlusion is a significant driver of *T*-wave signal attenuation. As we have shown for the HTHH eruption sequence observed by Mermaid floats and IMS stations, sound pressure levels decrease logarithmically with the number of obstacles encountered by the *T* wave along the propagation path. The strength of this relation grows with the portion of the Fresnel zone—the clearance ratio—that is being included in counting those obstacles. Obstacles nearer the great-circle path have a stronger attenuation effect, while expanding the search yields a diminishing rate of return in terms of explanatory power.

If *T*-wave signals are to be used to infer source characteristics, whether from volcanoes (e.g., Tepp & Dziak, 2021; Wech et al., 2025), or indeed any other source (e.g., Okal, 2001; Reymond et al., 2003), we recommend that sound pressure levels be corrected for bathymetric occlusion within the Fresnel zone. This will reduce the risk of backprojecting unmodeled path effects onto source attributes.

Taken together, these findings will be useful for designing future ocean-acoustic monitoring networks because they demonstrate that occlusion within some portion of the Fresnel zone—as determined by an acceptable level of signal transmission—should be considered when optimizing station placement and sensor specification, whether in efforts to monitor volcanic eruptions or assess potential explosions.

We do not have perfect knowledge of the seafloor (Mayer et al., 2018; Yu et al., 2024), nor of the ocean acoustic regime. The prospect of being able to "hear" the roughness of the former (Goff & Arbic, 2010), and sense the temperature of the latter (Wu et al., 2020) via differential observation of hydroacoustic phases is exciting.

6. Conclusions

A novel hydroacoustic data set from 24 Mermaid sensors of the 15 January 2022 submarine volcanic eruption at HTHH illuminates how the seafloor can shape the source signal along the path to the receiver. Supplemented by hydrophone records from moored IMS stations, we focused on the characteristics of a 30-min window that carries *T* waves associated with the main eruptive pulse. Beyond shedding light on the HTHH eruption sequence, we show that signal variability cannot simply be explained by differences in epicentral distance. We characterized path effects under the hypothesis that the seafloor environment along the propagation path is the main driver of mutual decorrelation and individual signal attenuation.

Simply counting occluders along the great-circle path at the depth of maximum fundamental-mode pressure explains 70% of the variance of sound pressure level adjusted for epicentral distance, while a broader tally of all occluders within the full width of the Fresnel zone boosts that statistic to 88%. While the strength of this relation increases as a function of the clearance ratio accounted for, the parameters derived from it are stable. In particular the slope of the regression line is very robust. Our final model predicts a 5.6 dB loss in adjusted sound pressure level per logarithm of full-Fresnel occlusion count.

Our findings may help explain progressive decorrelation of signals emanating from known or repeating sources but recorded at different locations, and may be used to adjust signal amplitudes to correct for occluded and lossy propagation paths. In particular our model has implications for constraining explosive or volcanic yield estimates and estimating earthquake magnitudes, and will be useful for modeling sound propagation losses through various oceanic paths when planning the hydroacoustic monitoring networks of the future.

Conflict of Interest

The authors declare no conflicts of interest relevant to this study.

Data Availability Statement

The International Federation of Digital Seismograph Networks (FDSN) has granted Mobile Earthquake Recorder in Marine Areas by Independent Divers (Mermaid) the network code MH (https://fdsn.org/networks/detail/MH/; DOI: https://doi.org/10.7914/SN/MH). Routinely reported Mermaid waveforms and open International Monitoring System (IMS) data (station H11) are hosted at the EarthScope Data Management Center (https://ds.iris.edu/ds/nodes/dmc/) for public distribution. Restricted IMS data (station H03) are available to registered users of the virtual Data Exploitation Centre (vDEC; https://ctbto.org/resources/for-researchers-experts/vdec).

Processed Mermaid data required to reproduce the figures in this paper are available from Simon (2025b). Mermaid instrumentation characteristics, including transfer-function poles and zeros, are detailed in Simon et al. (2022). Software required to reproduce the figures in this paper, using Crameri et al. (2020) colormaps, are published in Simon (2025a).

Acknowledgments

JDS thanks Gabrielle Tepp (Caltech) for enlightening conversations about underwater volcanic processes, Haakon Ervik (Caltech) for helping to derive and interpret acoustic eigenfunctions, and Dirk Metz (Preparatory Commission for the Comprehensive Nuclear-Test-Ban Treaty Organization) for providing IMS data and guidance on their processing. The views expressed in this study are those of the authors and do not necessarily reflect those of the Preparatory Commission for the CTBTO. We thank Ifremer, all of our friends and colleagues in the EarthScope-Oceans consortium, and all of our collaborators on the South Pacific Plume Imaging and Modeling (SPPIM) project, for being the many hands on deck that ultimately provided the unique Mermaid data set. The authors acknowledge Grants JSPS KAKENHI 19H00731 to MO and HS, NSF OCE-1917058 to FJS and JCEI, and NSF EAR-2341811 to FJS. Publication of this research was funded in part by the Gordon and Betty Moore Foundation through Grant GBMF13614 to FJS. Finally, all authors thank Editor Rachel Abercrombie, and two anonymous reviewers, whose insightful comments consequentially improved our submission and sharpened its focus.

References

Ainslie, M. A., Halvorsen, M. B., & Robinson, S. P. (2022). A terminology standard for underwater acoustics and the benefits of international standardization. *IEEE Journal of Oceanic Engineering*, *47*(1), 179–200. https://doi.org/10.1109/JOE.2021.3085947

Amante, C., & Eakins, B. W. (2009). ETOPO1 1 arc-minute global relief model: Procedures, data sources and analysis. *NOAA Technical Memorandum NESDIS NGDC-24*. National Geophysical Data Center, NOAA. https://doi.org/10.7289/V5C8276M

Baig, A. M., Dahlen, F. A., & Hung, S.-H. (2003). Traveltimes of waves in three-dimensional random media. *Geophysical Journal International*, *153*(2), 467–482. https://doi.org/10.1046/j.1365-246X.2003.01905.x

Bohnenstiehl, D. R., Dziak, R. P., Matsumoto, H., & Lau, T.-K. A. (2013). Underwater acoustic records from the March 2009 eruption of Hunga Ha'apai-Hunga Tonga volcano in the Kingdom of Tonga. *Journal of Volcanology and Geothermal Research*, *249*, 12–24. https://doi.org/10.1016/j.jvolgeores.2012.08.014

Bullington, K. (1957). Radio propagation fundamentals. *Bell System Technical Journal*, *36*(3), 593–626. https://doi.org/10.1002/j.1538-7305.1957.tb03855.x

Burky, A. L., Irving, J. C. E., & Simons, F. J. (2021). Instrument response removal and the 2020 M_{Lg} 3.1 Marlboro, New Jersey, earthquake. *Seismological Research Letters*, *92*(6), 3865–3872. https://doi.org/10.1785/0220210118

Caplan-Auerbach, J., Fox, C. G., & Duennebier, F. K. (2001). Hydroacoustic detection of submarine landslides on Kilauea volcano. *Geophysical Research Letters*, *28*(9), 1811–1813. https://doi.org/10.1029/2000GL012545

Carnes, M. R. (2009). *Description and evaluation of GDEM-V 3.0 (technical report)*. Naval Research Laboratory.

Červený, V., & Soares, J. E. P. (1992). Fresnel volume ray tracing. *Geophysics*, *57*(7), 902–915. https://doi.org/10.1190/1.1443303

Coleman, D. D., & Westcott, D. A. (2021). *CWNA certified wireless network administrator study guide* (6th ed.). John Wiley.

Crameri, F., Shephard, G. E., & Heron, P. J. (2020). The misuse of colour in science communication. *Nature Communications*, *11*(1), 5444. https://doi.org/10.1038/s41467-020-19160-7

Dall'Osto, D. R., Dahl, P. H., & Chapman, N. R. (2023). The sound from underwater explosions. *Acoustics Today*, *19*(1), 12–19. https://doi.org/10.1121/AT.2023.19.1.12

Davies, D., Kelly, E. J., & Filson, J. R. (1971). Vespa process for analysis of seismic signals. *Nature Physical Science*, *232*(27), 8–13. https://doi.org/10.1038/physci232008a0

De Caro, M., Montuori, C., Frugoni, F., Monna, S., Cammarano, F., & Beranzoli, L. (2021). *T*-phases observed at the Ionian seafloor: Seismic source and bathymetric effects. *Seismological Research Letters*, *92*(1), 481–493. https://doi.org/10.1785/0220200096

de Groot-Hedlin, C. D., & Orcutt, J. A. (2001). Excitation of *T*-phases by seafloor scattering. *Journal of the Acoustical Society of America*, *109*(5), 1944–1954. https://doi.org/10.1121/1.1361057

Del Grosso, V. A. (1974). New equation for the speed of sound in natural waters (with comparisons to other equations). *Journal of the Acoustical Society of America*, *56*(4), 1084–1091. https://doi.org/10.1121/1.1903388

Dietz, R. S., & Sheehy, M. J. (1954). Transpacific detection of Myojin volcanic explosions by underwater sound. *Geological Society of America Bulletin*, *65*(10), 941–956. https://doi.org/10.1130/0016-7606(1954)65[941:TDOMVE]2.0.CO;2

Donner, S., Steinberg, A., Lehr, J., Pilger, C., Hupe, P., Gaebler, P., et al. (2023). The January 2022 Hunga Volcano explosive eruption from the multitechnological perspective of CTBT monitoring. *Geophysical Journal International*, *235*(1), 48–73. https://doi.org/10.1093/gji/ggad204

Dziewoński, A. M., & Anderson, D. L. (1981). Preliminary reference Earth model. *Physics of the Earth and Planetary Interiors*, *25*(4), 297–356. https://doi.org/10.1016/0031-9201(81)90046-7

Efron, B., & Tibshirani, R. J. (1994). *An introduction to the bootstrap*. Chapman & Hall.

Ewing, M., & Worzel, J. L. (1948). Propagation of sound in the ocean. Part III: Long-range sound transmission. *Geological Society Memoirs*, *27*, 1–35. https://doi.org/10.1130/MEM27-3-p1

Forget, G., Campin, J.-M., Heimbach, P., Hill, C. N., Ponte, R. M., & Wunsch, C. (2015). ECCO version 4: An integrated framework for non-linear inverse modeling and global ocean state estimation. *Geoscientific Model Development*, *8*, 3071–3104. https://doi.org/10.5194/gmd-8-3071-2015

Gibbons, S. J. (2022). The hydroacoustic network of the CTBT International Monitoring System: Access and exploitation. *Journal of Peace and Nuclear Disarmament*, *5*(2), 452–468. https://doi.org/10.1080/25751654.2022.2129948

Goff, J. A., & Arbic, B. K. (2010). Global prediction of abyssal hill roughness statistics for use in ocean models from digital maps of paleo-spreading rate, paleo-ridge orientation, and sediment thickness. *Ocean Modelling*, *32*(1–2), 36–43. https://doi.org/10.1016/j.ocemod.2009.10.001

Goldstein, P., Dodge, D., Firpo, M., & Minner, L. (2003). SAC2000: Signal processing and analysis tools for seismologists and engineers. In W. H. K. Lee, H. Kanamori, P. C. Jennings, & C. Kisslinger (Eds.), *International handbook of earthquake and engineering seismology, Part B* (Vol. 81, pp. 1613–1614). Academic Press. https://doi.org/10.1016/S0074-6142(03)80284-X

Green, D. N., Evers, L. G., Fee, D., Matoza, R. S., Snellen, M., Smets, P., & Simons, D. (2013). Hydroacoustic, infrasonic and seismic monitoring of the submarine eruptive activity and sub-aerial plume generation at South Sarigan, May 2010. *Journal of Volcanology and Geothermal Research*, *257*, 31–43. https://doi.org/10.1016/j.jvolgeores.2013.03.006

Harben, P. E., Hollfelder, J. R., & Rodgers, A. J. (1999). *Experimentally determined coordinates for three MILS hydrophones near Ascension Island (technical report)*. Lawrence Livermore National Laboratory.

Heaney, K. D., Kuperman, W. A., & McDonald, B. E. (1991). Perth–Bermuda sound propagation (1960): Adiabatic mode interpretation. *Journal of the Acoustical Society of America*, *90*(5), 2586–2594. https://doi.org/10.1121/1.402062

Heaney, K. D., Prior, M., & Campbell, R. L. (2017). Bathymetric diffraction of basin-scale hydroacoustic signals. *Journal of the Acoustical Society of America*, *141*(2), 878–885. https://doi.org/10.1121/1.4976052

Helffrich, G., Wookey, J., & Bastow, I. (2013). *The seismic analysis code. A primer and user's guide*. Cambridge University Press.

Hello, Y. (2018). *SPPIM cruise, RV Alis (technical report)*. Flotte Océanographique Française.

Hello, Y., & Nolet, G. (2020). Floating seismographs (MERMAIDS). In H. K. Gupta (Ed.), *Encyclopedia of Solid Earth Geophysics* (pp. 1–6). Springer. https://doi.org/10.1007/978-3-030-10475-7_248-1

Hello, Y., Ogé, A., Sukhovich, A., & Nolet, G. (2011). Modern Mermaids: New floats image the deep Earth. *Eos Transactions AGU*, *92*(40), 337–338. https://doi.org/10.1029/2011EO400001

Johnson, R. H., & Norris, R. A. (1968). Geographic variation of Sofar speed and axis depth in the Pacific Ocean. *Journal of Geophysical Research*, *73*(14), 4695–4700. https://doi.org/10.1029/JB073i014p04695

Joubert, C., Nolet, G., Bonnieux, S., Deschamps, A., Dessa, J.-X., & Hello, Y. (2016). *P*-delays from floating seismometers (MERMAID), Part I: Data processing. *Seismological Research Letters*, *87*(1), 73–80. https://doi.org/10.1785/0220150111

Kennett, B. L. N., Engdahl, E. R., & Buland, R. (1995). Constraints on seismic velocities in the Earth from traveltimes. *Geophysical Journal International*, *122*(1), 108–124. https://doi.org/10.1111/j.1365-246X.1995.tb03540.x

Kibblewhite, A. C. (1966). Detection and location of a new underwater volcano. *Nature*, *210*(5039), 938–939. https://doi.org/10.1038/210938a0

Latchman, J. L., Dondin, F. J.-Y., Robertson, R. E. A., Stewart, R., Smith, P., Lynch, L. L., et al. (2023). Contrasting *T*-phase and *P*-wave patterns from the 2015 and 2017 eruptions of the submarine volcano Kick-'em-Jenny: Influence of cardinal direction on recorded first phase arrival. *Bulletin of the Seismological Society of America*, *113*(5), 2056–2068. https://doi.org/10.1785/0120220101

Le Bras, R. J., Bittner, P., Kuśmierczyk-Michulec, J., Mialle, P., & Rambolamanana, G. (2025). Timing analysis of the multiple passages of the pressure wave generated by the 2022 Hunga Tonga-Hunga Ha'apai and comparison with the 1883 Krakatoa pressure wave. *Pure and Applied Geophysics*, *182*, 1–28. https://doi.org/10.1007/s00024-024-03507-y

Le Bras, R. J., Zampolli, M., Metz, D., Haralabus, G., Bittner, P., Villarroel, M., et al. (2023). The Hunga Tonga–Hunga Ha'apai eruption of 15 January 2022: Observations on the International Monitoring System (IMS) hydroacoustic stations and synergy with seismic and infrasound sensors. *Seismological Research Letters*, *94*(2A), 578–588. https://doi.org/10.1785/0220220240

Levis, C. A., Johnson, J. T., & Teixeira, F. L. (2010). *Radiowave propagation: Physics and applications*. John Wiley.

Maher, S. P., Matoza, R. S., de Groot-Hedlin, C., Kim, K., & Gee, K. (2021). Evaluating the applicability of a screen diffraction approximation to local volcano infrasound. *Volcanica*, *4*(1), 67–85. https://doi.org/10.30909/vol.04.01.6785

Matoza, R. S., Fee, D., Assink, J. D., Iezzi, A. M., Green, D. N., Kim, K., et al. (2022). Atmospheric waves and global seismoacoustic observations of the January 2022 Hunga eruption, Tonga. *Science*, *377*(6601), 95–100. https://doi.org/10.1126/science.abo7063

Matsumoto, H., Haxel, J. H., Dziak, R. P., Bohnenstiehl, D. R., & Embley, R. W. (2011). Mapping the sound field of an erupting submarine volcano using an acoustic glider. *Journal of the Acoustical Society of America*, *129*(3), EL94–EL99. https://doi.org/10.1121/1.3547720

Matsumoto, H., Zampolli, M., Haralabus, G., Stanley, J., Robertson, J., & Özel, N. M. (2023). Hydroacousic signals originating from marine volcanic activity at Kadovar Island, Papua New Guinea, recorded by the Comprehensive Nuclear-Test-Ban Treaty International Monitoring System. *Pure and Applied Geophysics*, *180*(4), 1353–1373. https://doi.org/10.1007/s00024-022-03096-8

Mayer, L., Jakobsson, M., Allen, G., Dorschel, B., Falconer, R., Ferrini, V., et al. (2018). The Nippon Foundation–GEBCO Seabed 2030 project: The quest to see the world's oceans completely mapped by 2030. *Geosciences*, *8*(2), 63. https://doi.org/10.3390/geosciences8020063

McDougall, T. J., & Barker, P. M. (2011). *Getting started with TEOS-10 and the Gibbs Seawater (GSW) oceanographic toolbox*. SCOR/IAPSO WG127.

Metz, D., Watts, A. B., Grevemeyer, I., & Rodgers, M. (2018). Tracking submarine volcanic activity at Monowai: Constraints from long-range hydroacoustic measurements. *Journal of Geophysical Research*, *123*(9), 7877–7895. https://doi.org/10.1029/2018JB015888

Metz, D., Watts, A. B., Grevemeyer, I., Rodgers, M., & Paulatto, M. (2016). Ultra-long-range hydroacoustic observations of submarine volcanic activity at Monowai, Kermadec Arc. *Geophysical Research Letters*, *43*(4), 1529–1536. https://doi.org/10.1002/2015GL067259

Millero, F. J., & Li, X. (1994). Comments on "On equations for the speed of sound in seawater". *Journal of the Acoustical Society of America*, *95*(5), 2757–2759. https://doi.org/10.1121/1.409844

Mittal, T., & Delbridge, B. (2019). Detection of the 2012 Havre submarine eruption plume using Argo floats and its implications for ocean dynamics. *Earth and Planetary Science Letters*, *511*, 105–116. https://doi.org/10.1016/j.epsl.2019.01.035

Munk, W. H. (1974). Sound channel in an exponentially stratified ocean, with application to SOFAR. *Journal of the Acoustical Society of America*, *55*(2), 220–226. https://doi.org/10.1121/1.1914492

Nolet, G., Hello, Y., van der Lee, S., Bonnieux, S., Ruiz, M. C., Pazmino, N. A., et al. (2019). Imaging the Galápagos mantle plume with an unconventional application of floating seismometers. *Scientific Reports*, *9*(1), 1326. https://doi.org/10.1038/s41598-018-36835-w

Nolet, G., Hoang, N. B., Bonnieux, S., Kondo, Y., Kong, F., Obayashi, M., et al. (2025). Picking first arrivals in hydroacoustic seismograms from MERMAID floats. *Seismica*, *4*(1). https://doi.org/10.26443/seismica.v4i1.1505

Nolet, G., Simon, J. D., & Bonnieux, S. (2024). How accurately are MERMAID seismograms located? *Seismological Research Letters*, *95*(4), 2368–2374. https://doi.org/10.1785/0220230377

Norris, R. A., & Johnson, R. H. (1969). Submarine volcanic eruptions recently located in the Pacific by SOFAR hydrophones. *Journal of Geophysical Research*, *74*(2), 650–664. https://doi.org/10.1029/JB074i002p00650

Northrop, J., & Colborn, J. G. (1974). Sofar channel axial sound speed and depth in the Atlantic Ocean. *Journal of Geophysical Research*, *79*(36), 5633–5641. https://doi.org/10.1029/JC079i036p05633

Okal, E. A. (2001). T-Phase stations for the International Monitoring System of the Comprehensive Nuclear-Test Ban Treaty: A global perspective. *Seismological Research Letters*, *72*(2), 186–196. https://doi.org/10.1785/gssrl.72.2.186

Okal, E. A. (2008). The generation of *T* waves by earthquakes. *Advances in Geophysics*, *49*, 1–65. https://doi.org/10.1016/S0065-2687(07)49001-X

Oliveira, T. C. A., Lin, Y.-T., & Porter, M. B. (2021). Underwater sound propagation modeling in a complex shallow water environment. *Frontiers in Marine Science*, *8*, 751327. https://doi.org/10.3389/fmars.2021.751327

Oliveira, T. C. A., Prior, M., Saragiotis, C., Park, J. H., Metz, D., Bittner, P., et al. (2025). Global detection capabilities of *T* phases using the IMS hydrophone network. *Seismological Research Letters*, *96*(2A), 731–743. https://doi.org/10.1785/0220240418

Pipatprathanporn, S., & Simons, F. J. (2022). One year of sound recorded by a MERMAID float in the Pacific: Hydroacoustic earthquake signals and infrasonic ambient noise. *Geophysical Journal International*, *228*(1), 193–212. https://doi.org/10.1093/gji/ggab296

Pipatprathanporn, S., & Simons, F. J. (2024). Waveform modeling of hydroacoustic teleseismic earthquake records from autonomous MERMAID floats. *Geophysical Journal International*, *239*(1), 136–154. https://doi.org/10.1093/gji/ggae238

Piserchia, P.-F., Virieux, J., Rodrigues, D., Gaffet, S., & Talandier, J. (1998). Hybrid numerical modelling of *T*-wave propagation: Application to the midplate experiment. *Geophysical Journal International*, *133*(3), 789–800. https://doi.org/10.1046/j.1365-246X.1998.00546.x

Porter, M. B. (1992). *The KRAKEN normal mode program. Saclant undersea research centre memorandum (SM-245) (Mem. report 6920; technical report)*. Naval Research Laboratory.

Pulli, J. J., & Upton, Z. M. (2002). Hydroacoustic observations of Indian earthquake provide new data on T-waves. *Eos Transactions AGU*, *83*(13), 145–151. https://doi.org/10.1029/2002EO000090

Purkis, S. J., Ward, S. N., Fitzpatrick, N. M., Garvin, J. B., Slayback, D., Cronin, S. J., et al. (2023). The 2022 Hunga-Tonga megatsunami: Near-field simulation of a once-in-a-century event. *Science Advances*, *9*(15), eadf5493. https://doi.org/10.1126/sciadv.adf5493

Reymond, D., Hyvernaud, O., Talandier, J., & Okal, E. A. (2003). *T*-wave detection of two underwater explosions off Hawaii on 13 April 2000. *Bulletin of the Seismological Society of America*, *93*(2), 804–816. https://doi.org/10.1785/0120010296

Ringler, A. T., Anthony, R. E., Aster, R. C., Taira, T., Shiro, B. R., Wilson, D. C., et al. (2023). The global seismographic network reveals atmospherically coupled normal modes excited by the 2022 Hunga Tonga eruption. *Geophysical Journal International*, *232*(3), 2160–2174. https://doi.org/10.1093/gji/ggac284

Roquet, F., Madec, G., McDougall, T. J., & Barker, P. M. (2015). Accurate polynomial expressions for the density and specific volume of seawater using the TEOS-10 standard. *Ocean Modelling*, *90*, 29–43. https://doi.org/10.1016/j.ocemod.2015.04.002

Searcy, C. (2013). Seismicity associated with the May 2010 eruption of South Sarigan Seamount, Northern Mariana Islands. *Seismological Research Letters*, *84*(5), 1055–1061. https://doi.org/10.1785/0220120168

Simon, J. D., Simons, F. J., & Irving, J. C. E. (2021). A MERMAID miscellany: Seismoacoustic signals beyond the *P* wave. *Seismological Research Letters*, *92*(6), 3657–3667. https://doi.org/10.1785/0220210052

Simon, J. D. (2025a). omnia [Software]. https://doi.org/10.5281/zenodo.5637492

Simon, J. D. (2025b). MERMAID hydroacoustic records of the January 2022 Hunga Tonga-Hunga Ha'apai eruption [Dataset]. https://doi.org/10.5281/zenodo.15186135

Simon, J. D., Bonnieux, S., Rocca, F., Simons, F. J., & the EarthScope-Oceans Consortium. (2021). automaid [Software]. https://doi.org/10.5281/zenodo.5057096

Simon, J. D., Simons, F. J., & Irving, J. C. E. (2022). Recording earthquakes for tomographic imaging of the mantle beneath the South Pacific by autonomous MERMAID floats. *Geophysical Journal International*, *228*(1), 147–170. https://doi.org/10.1093/gji/ggab271

Simon, J. D., Simons, F. J., & Nolet, G. (2020). Multiscale estimation of event arrival times and their uncertainties in hydroacoustic records from autonomous oceanic floats. *Bulletin of the Seismological Society of America*, *110*(3), 970–997. https://doi.org/10.1785/0120190173

Simons, F. J., Nolet, G., Georgief, P., Babcock, J. M., Regier, L. A., & Davis, R. E. (2009). On the potential of recording earthquakes for global seismic tomography by low-cost autonomous instruments in the oceans. *Journal of Geophysical Research*, *114*(B5), B05307. https://doi.org/10.1029/2008JB006088

Skarsoulis, E. K., & Cornuelle, B. D. (2004). Travel-time sensitivity kernels in ocean acoustic tomography. *Journal of the Acoustical Society of America*, *116*(1), 227–238. https://doi.org/10.1121/1.1753292

Spetzler, J., & Snieder, R. (2001). The effect of small-scale heterogeneity on the arrival time of waves. *Geophysical Journal International*, *145*(3), 786–796. https://doi.org/10.1046/j.1365-246x.2001.01438.x

Sukhovich, A., Bonnieux, S., Hello, Y., Irisson, J.-O., Simons, F. J., & Nolet, G. (2015). Seismic monitoring in the oceans by autonomous floats. *Nature Communications*, *6*(1), 8027. https://doi.org/10.1038/ncomms9027

Sukhovich, A., Irisson, J.-O., Simons, F. J., Ogé, A., Hello, Y., Deschamps, A., & Nolet, G. (2011). Automatic discrimination of underwater acoustic signals generated by teleseismic P-waves: A probabilistic approach. *Geophysical Research Letters*, *38*(18), L18605. https://doi.org/10.1029/2011GL048474

Talandier, J., & Okal, E. A. (1987). Seismic detection of underwater volcanism: The example of French Polynesia. *Pure and Applied Geophysics*, *125*(6), 919–950. https://doi.org/10.1007/BF00879361

Talandier, J., & Okal, E. A. (1998). On the mechanism of conversion of seismic waves to and from *T* waves in the vicinity of island shores. *Bulletin of the Seismological Society of America*, *88*(2), 621–632. https://doi.org/10.1785/BSSA0880020621

Tepp, G., & Dziak, R. P. (2021). The seismo-acoustics of submarine volcanic eruptions. *Journal of Geophysical Research*, *126*(4), e2020JB020912. https://doi.org/10.1029/2020JB020912

Tepp, G., & Haney, M. M. (2019). Comparison of short-term seismic precursors and explosion parameters during the 2016–2017 Bogoslof eruption. *Bulletin of Volcanology*, *81*(11), 63. https://doi.org/10.1007/s00445-019-1323-8

Terry, J. P., Goff, J., Winspear, N., Bongolan, V. P., & Fisher, S. (2022). Tonga volcanic eruption and tsunami, January 2022: Globally the most significant opportunity to observe an explosive and tsunamigenic submarine eruption since AD 1883 Krakatau. *Geoscience Letters*, *9*(24), 1–11. https://doi.org/10.1186/s40562-022-00232-z

Thurin, J., & Tape, C. (2023). Comparison of force and moment tensor estimations of subevents during the 2022 Hunga–Tonga submarine volcanic eruption. *Geophysical Journal International*, *235*(2), 1959–1981. https://doi.org/10.1093/gji/ggad323

Thurin, J., Tape, C., & Modrak, R. (2022). Multi-event explosive seismic source for the 2022 M_w 6.3 Hunga Tonga submarine volcanic eruption. *The Seismic Record*, *2*(4), 217–226. https://doi.org/10.1785/0320220027

Thurin, J., Tape, C., & Modrak, R. (2023). *Erratum to* Multi-event explosive seismic source for the 2022 M_w 6.3 Hunga Tonga submarine volcanic eruption. *The Seismic Record*, *3*(2), 168–170. https://doi.org/10.1785/0320230014

Tolstoy, I., & Ewing, M. (1950). The *T* phase of shallow-focus earthquakes. *Bulletin of the Seismological Society of America*, *40*(1), 25–51. https://doi.org/10.1785/BSSA0400010025

Walker, S. L., & de Ronde, C. E. J. (2024). Ongoing activity at Hunga submarine volcano, Tonga: The case for better monitoring of submarine volcanoes worldwide. *Geochemistry, Geophysics, Geosystems*, *25*(8), e2024GC011685. https://doi.org/10.1029/2024GC011685

Weatherall, P., Marks, K. M., Jakobsson, M., Schmitt, T., Tani, S., Arndt, J. E., et al. (2015). A new digital bathymetric model of the world's oceans. *Earth and Space Science*, *2*(8), 331–345. https://doi.org/10.1002/2015EA000107

Wech, A. G., Haney, M. M., Chang, J. C., Jolly, A. D., Yoon, C. E., & Skoumal, R. J. (2025). Local, regional, and distal recordings of seismic unrest at Ta'ū Island volcano, American Samoa. *Bulletin of Volcanology*, *87*(3), 15. https://doi.org/10.1007/s00445-025-01798-0

Wech, A. G., Tepp, G., Lyons, J., & Haney, M. (2018). Using earthquakes, *T* waves, and infrasound to investigate the eruption of Bogoslof volcano, Alaska. *Geophysical Research Letters*, *45*(14), 6918–6925. https://doi.org/10.1029/2018GL078457

Wilmut, M. J., Chapman, N. R., & Prior, M. (2010). Detection of *H*-phase signals from hydroacoustic data using quadratic classification. *IEEE Journal of Oceanic Engineering*, *35*(3), 618–622. https://doi.org/10.1109/JOE.2010.2053771

Wright, C. J., Hindley, N. P., Alexander, M. J., Barlow, M., Hoffmann, L., Mitchell, C. N., et al. (2022). Surface-to-space atmospheric waves from Hunga Tonga–Hunga Ha'apai eruption. *Nature*, *609*(7928), 741–746. https://doi.org/10.1038/s41586-022-05012-5

Wright, I. C., Chadwick, W. W. Jr, de Ronde, C. E. J., Reymond, D., Hyvernaud, O., Gennerich, H.-H., et al. (2008). Collapse and reconstruction of Monowai submarine volcano, Kermadec Arc, 1998–2004. *Journal of Geophysical Research*, *113*(B8), B08S03. https://doi.org/10.1029/2007JB005138

Wu, W., Shen, Z., Peng, S., Zhan, Z., & Callies, J. (2023). Seismic ocean thermometry using CTBTO hydrophones. *Journal of Geophysical Research*, *128*(9), e2023JB026687. https://doi.org/10.1029/2023JB026687

Wu, W., Zhan, Z., Peng, S., Ni, S., & Callies, J. (2020). Seismic ocean thermometry. *Science*, *369*(6510), 1510–1515. https://doi.org/10.1126/science.abb9519

Yu, Y., Chen, Y. J., Guo, Z., & Ge, Z. (2023). Long-term seismic network in South China Sea by floating MERMAIDs. *Science China Earth Sciences*, *66*(9), 1979–1993. https://doi.org/10.1007/s11430-022-1100-3

Yu, Y., Sandwell, D. T., & Dibarboure, G. (2024). Abyssal marine tectonics from the SWOT mission. *Science*, *386*(6727), 1251–1256. https://doi.org/10.1126/science.ads4472

Yuen, D. A., Scruggs, M. A., Spera, F. J., Zheng, Y., Hu, H., McNutt, S. R., et al. (2022). Under the surface: Pressure-induced planetary-scale waves, volcanic lightning, and gaseous clouds caused by the submarine eruption of Hunga Tonga-Hunga Ha'apai volcano. *Earthquake Research Advances*, *2*(3), 100134. https://doi.org/10.1016/j.eqrea.2022.100134

Zheng, Y., Hu, H., Spera, F. J., Scruggs, M., Thompson, G., Jin, Y., et al. (2023). Episodic magma hammers for the 15 January 2022 cataclysmic eruption of Hunga Tonga-Hunga Ha'apai. *Geophysical Research Letters*, *50*(8), e2023GL102763. https://doi.org/10.1029/2023GL102763

Supporting Information for "Hydroacoustic Observations of the 15 January 2022 Hunga Tonga-Hunga Ha'apai Eruption: The Role of Bathymetry Along the Path"

DOI: 10.1029/2025JB032996

Joel D. Simon[1*], Frederik J. Simons[1], Jessica C. E. Irving[2],

Wenbo Wu[3†], Masayuki Obayashi[4], Yong Yu[5,6],

Yongshun John Chen[5], Hiroko Sugioka[7], and Yann Hello[8]

[1]Department of Geosciences, Princeton University, Princeton, NJ, USA

[2]School of Earth Sciences, University of Bristol, Bristol, UK

[3]Department of Geology and Geophysics, Woods Hole Oceanographic Institution, Woods Hole, MA, USA

[4]Japan Agency for Marine-Earth Science and Technology, Yokosuka, Japan

[5]Department of Ocean Science and Engineering, Southern University of Science and Technology, Shenzhen, China

[6]Institute of Geology, Chinese Earthquake Administration, Beijing, China

[7]Kobe Ocean-Bottom Exploration Center, Kobe University, Kobe, Japan

[8]Seisocean, Saint Jeannet, Provence-Alpes-Côte d'Azur, France

[*]Now at Bathymetrix, LLC, Portland, OR, USA
[†]Now at Department of Earth and Planetary Science, University of California, Berkeley, CA, USA

Corresponding author: Joel D. Simon, jdsimon@bathymetrix.com

Contents of this file

Preliminaries

Figure S1 is an alternative rendition of the data shown in Figure 2 of the Main Text, sorted by epicentral distance. Figure S2 is a record section of the data shown in Figure 2 of the Main Text, with local events included. This document was formatted using the `agutexSI2019.cls` LaTeXclass file, as required by *Journal of Geophysical Research: Solid Earth*.

S1. Time-Slowness Analysis

Figure S3 summarizes our data set as vespagrams (Davies et al., 1971) that render summed energy as a function of slowness and timing relative to the mean *T*-wave arrival time, in Figure S3(A), and to the mean *P*-wave arrival time, in Figure S3(B), calculated using a mean epicentral distance of 31.4°. Gaps in the crosshairs represent those hypothetical first arrivals. To cross-reference both panels: if the axis was expanded, the *P* wave would lie near $(-32.9\,\text{min}, -66.3\,\text{s/deg})$ in Figure S3(A). Predicted arrival times for *S* waves, and for Love (4.33 km/s) and Rayleigh (3.82 km/s) waves are marked by crosses to locate surface wave velocities identified by Thurin and Tape (2023). Phase arrival times were computed in the `ak135` model (Kennett et al., 1995) using `MatTaup`, written in MATLAB by Qin Li while at the University of Washington in November 2002.

Category A and B signals were filtered as in Figure 2 of the Main Text to generate Figure S3(A), and within the lower frequency band where MERMAID most strongly records *P* waves (Simon et al., 2022) to make Figure S3(B), as noted in the lower-right corner. To suppress noise, we furthermore used 30 s moving root-mean-squared (RMS) signal envelopes (the same used for correlations in the Main Text) before shifting and summing. Category C traces, which did not record the *T* wave were excluded from the vespagram calculation. Only one station from each of the IMS arrays, H11S1 and H03S1, was included so as not to bias the results.

Figure S3(A) shows that the majority of energy in our data set arrives with the slowness of a hydroacoustic phase. We see that energy is first concentrated near the predicted arrival time and

slowness of the *T* wave, and then after a minutes-long 'lull' reemerges into a longer-duration and more defocused secondary 'rumble.' That rumble reaches its maximum about 15 minutes later than, but at the same slowness of, the initial burst, and thus likely represents later-arriving *T* waves associated with the eruption.

Figure S3(B) lacks identifiable body or surface waves. No significant energy is seen to concentrate around those expected slownesses and arrival times. Thurin and Tape (2023) observed such phases at frequencies below 0.067 Hz (15 s period), below the nominal sensitivity of MERMAID (Simon et al., 2022).

S2. Near-Source Bathymetry and Travel-Time Corrections

To compute predicted first arrival times in this study we assume all waves travel at the speed of sound in water along the entire great-circle path from source to receiver.

One could imagine a simple travel-time correction that instead presumes that seismic energy leaves the Hunga Tonga-Hunga Ha'apai (HTHH) eruption as *P* waves (e.g., traveling at 5.8 km/s) before converting to slower *T* waves (1.48 km/s) at the solid-fluid interface. A first-order travel-time correction could assert that the conversion point lies along the solid-fluid interface where the seafloor first reaches 1350 m, the median depth of the maximum of the fundamental acoustic mode that we focus on, and where we count occluders (Section 3.1 of the Main Text, and Section S3 in the Supporting Information).

We do not claim this first-order travel-time correction captures actual *T*-wave generation for this event in any meaningful manner. We show it merely provides one reason why arrivals at H11 appear so delayed compared to stations to the east of HTHH when aligned on the predicted pure *T*-wave travel time (Figure 2 of the Main Text).

Figure S5 shows near-source bathymetry for stations P0045 and H11S1. If an initial *P*-wave path is assumed for both (much longer in the case of P0045) then the predicted arrival time at P0045

would shift relatively earlier (to the left in Figure 2 in the Main Text). When compared as in the right column of Figure 4 in the Main Text, where vertical lines mark first arrival times relative to each envelope, the result is that the perceived offset is substantially shrunk.

Here is a breakdown of that process:

```
Total distance to P0045:  1110.5 km
Total distance to H11S1:  4761.1 km


P0045:
Travel time for T wave (1110.5 km):  750.3 s
Travel time for P wave (103.2 km) then T wave (1007.2 km):  698.4 s
Time difference between one- and two-leg:  52.0 s


H11S1:
Travel time for T wave (4761.1 km):  3217.0 s
Travel-time for P wave (9.0 km) then T wave (4752.1 km):  3212.4 s
Time difference between one- and two-leg:  4.5 s
```

Therefore, the predicted arrival time (vertical line) of the upper envelope (H11S1) is only shifted 4.5 s to the left, while it is shifted 52 s to the left for the lower envelope (P0045) compared with the similar panel in Figure 4 of the Main Text, as shown in Figure S6.

S3. Ocean Depth, Sound Speed Profile, and Acoustic Modes

Figure S7 shows a profile through ocean sound-speed model GDEM-V 3.0 (Carnes, 2009) from HTHH to IMS station H03S1 (most distant), with MERMAIDS P0045, P0041, P0053, P0023, and P0040 (along similar azimuths, ordered by increasing distance; see Figure 1 in the Main Text and Table S1) projected onto the path, taken for a 'typical' month of January.

In the Main Text we explain our motivation to focus on the maximum of the 2.5 Hz acoustic fundamental mode when determining the depth to count occluders. To obtain modal pressure eigenfunctions we use the KRAKEN software (Porter, 1992) with specific ocean depths and sound-speed profiles overlying a halfspace with seafloor properties from the PREM model (Dziewoński & Anderson, 1981). To choose appropriate input values of ocean depth and sound speed, we use ECCO (Forget et al., 2015), a time-resolved ocean model with a spatial resolution of $0.5^\circ \times 0.5^\circ$, approximately 56×56 km^2 at the equator, and Roquet, Madec, McDougall, and Barker (2015) to map state variables into sound speed using the `gsw-python` toolbox (McDougall & Barker, 2011). To mirror this coarse resolution we computed average ocean depths and sound-speed profiles along 100 km-long north-south corridors with our receiver locations at their center, employing a 10-year averaged January sound speed. Regionally averaged ocean depths were computed using ETOPO1 (Amante & Eakins, 2009).

Figure S8 plots eigenfunctions of sound pressure for a 2.5 Hz acoustic fundamental mode propagating in one-dimensional ocean models of depths 5580 m (Figure S8(A), solid black curve), and 4020 m and 1146 m (Figure S8(B), solid black and dashed curves, respectively). Eigenfunctions are normalized to yield equal depth-integrated squared amplitudes, and may include a non-trivial component in the solid Earth (not shown). These two panels illustrate the cases pertinent to MERMAID P0045 (floating at 1500 m depth, 4080 m above the regionally averaged ocean floor as computed with ETOPO1, and 4140 m above the local ocean floor according to the GEBCO_2014 (Weatherall et al., 2015) model), and IMS station H11S3 (anchored at 726 m depth, 3294 m above the regionally averaged ocean floor as computed with ETOPO1, but in actuality only 420 m above the local ocean floor as reported by IMS).

In Figure S8(A), MERMAID P0045 is marked by a blue triangle, the local seafloor by a red horizontal line, and the 100-km averaged ocean depth by a black horizontal line where the mode solution vanishes. The fundamental mode is shown by a solid black line: the bulk of the *T*-

wave energy propagates well above any local bathymetric perturbations. In Figure S8(B), shallow seafloor IMS station H11S3 is shown twice, as blue diamonds, on the modal eigenfunction (black solid curve) for the 100-km averaged sound speed profile and ocean depth marked by the black horizontal line, and on the modal eigenfunction (black dashed curve) for the sound speed profile and local ocean depth marked by the red solid line at 1146 m.

Also in Figure S8(A), three box plots (minimum, 25$^{\text{th}}$, 50$^{\text{th}}$ and 75$^{\text{th}}$ percentiles, maximum, with outliers represented by crosses) illustrate the range of cruising depths (marked STDP) of all 29 receivers that recorded the HTHH event, the ocean depths averaged along every great-circle path from source to receiver (marked GCP OCDP), and the corresponding maxima of their fundamental-mode pressure eigenfunctions (marked Mode Max.). For stations to the east of HTHH (all except P0048, P0049 and H11) only the path after the Kermadec-Tonga trench (the presumptive seismoacoustic conversion point) was considered.

As with P0045 in Figure S8(A), it is clear that the seafloor will rarely greatly affect sound pressure levels for any of these oceanic paths, as even the most extreme minimum-average seafloor depth is around 3000 m, where the average ocean-depth sound pressure eigenfunctions display low sensitivity. Only bathymetric occluders that interact significantly with the pressure eigenmode are likely to be of high acoustic signal-blocking importance (Heaney et al., 1991; de Groot-Hedlin & Orcutt, 2001). On the other hand, for the particular example of IMS station H11S3, Figure S8(B), inspection of the near-receiver bathymetric profile reveals that the seafloor undergoes rapid bathymetric shoaling near this IMS station which is, essentially, moored on a seamount. This rapid transition from deep to shallow ocean might result in energy conversions as the fundamental mode starts to "feel" the seafloor in shallower waters, which we are unable to capture using a one-dimensional modeling framework. We do not attempt to account for the details of any amplification factors that may arise as a result. Hence, of the two candidate modal solutions, we

consider the deeper regional-average ocean solution to be the most representative for the relevant propagation path.

Figure S9 shows sound speeds and pressure eigenmodes as in Figure S8 for all 29 stations that reported Category A and B signals.

S4. Bathymetric Occlusion and *T*-Wave Observability

Figures S10–S44 contain time and spectral domain signals, and bathymetric profiles and maps for all sensors, sorted by epicentral distance. Not every sensor was able to detect HTHH. Section 4.2 of the Main Text explores how occlusion modulates amplitudes of detected Category A and B signals. This section is the complementary exploration of how occlusion affects observability in general, i.e., now including Category C records.

Figure S45 shows the ranked RMS pressure of all the records in Categories A, B, and C, for all 35 stations in this study, against the rank of their occlusion count. To continue to the graphical convention used in in the Main Text, symbols for Category A and B records are shown in blue and black, whereas those of Category C are gray. Only Category A and Category B records correspond to actual *signal*, whereas Category C records, effectively, contain *noise* segments within the same reference time window. In the top left corner of Figure S45 we find receivers along completely unimpeded paths, which we simply stacked on top of one another. In the bottom right we find again the cluster of H11 stations, all of which lie on highly occluded paths, with generally low, though relatively varying, RMS values which likely reflect their local noise environments.

The general decline in RMS following the trend of little to heavily occluded paths shown in Figure S45 is in line with our earliest expectations, although some stations notably defy this tendency. While occlusion clearly does degrade the hydroacoustic record, it is not so that the stations that recorded no signal are also the most occluded: if that were so, Category C stations would be contiguously grouped in the bottom right of Figure S45. Conversely, and perhaps paradoxically,

among the lowest-ranked RMS and highest-occluded signals feature clear Category A signals of high quality.

Beyond the reservations enunciated in Section 2.6 of the Main Text, first among all the possible confounding factors that we wish to disambiguate is the local noise environment. In Figure 3 of the Main Text we highlighted a 30-minute window in the record obtained from MERMAID P0045 as containing the *T*-wave "signal." For the Category A and B records we now label the 10-minute window that precedes the 30-minute signal segment, whatever it may contain (see, e.g., especially the 13 waveforms P0023 to P0048, excluding P0049, in Figure 2 of the Main Text, where this window in fact contains HTHH signal), as "noise."

Calculated in this manner, Figure S46 renders the RMS pressure of the 30-minute signal versus the 10-minute preceding windows. A solid line tracks a signal-to-noise ratio (SNR) of 1:1, while a dashed represents an SNR of 2:1. Figure S46(A) includes all stations, while Figure S46(B) is a zoom-in to show detail about the lowest-ranked RMS signals—ranks 17 (H03N2) through 35 (H11N3) in Figure S45, which excludes stations P0054–P0040—where the 10-minute segments are, indeed, mostly random noise. Figure S46(B) makes it clear that Category C signals congregate near the solid line marking the 1:1 SNR. Float N0004 lies close to that line, confirming the visual perception in Figure 2 of the Main Text that its signal is rather small, which may help clarify its anomalous position in the lineup of Figure S45.

Figure S46 confirms that the noise level of the H11 cluster of stations is exceptionally low. This may help explain why some *T* waves were recorded with such clarity at those locations despite their high occlusion counts, while others were not, despite their relatively lower occlusion values. Figure S46 furthermore shows that the *noise* level (horizontal coordinate) at float P0025 was relatively elevated, ranking higher than the *T*-wave signal (vertical coordinate) recorded by nine Category A and B stations (those to the right of P0025 in Figure S45).

Taken all together, Figure S45 and S46 help substantiate our assertion that transmission loss and diminishing signal quality scale with increasing bathymetric occlusion count. Therefore, in the results section of the Main Text, we drop Category C signals from consideration to derive a relationship between bathymetric occlusion and signal attenuation.

References

Amante, C., & Eakins, B. W. (2009). ETOPO1 1 Arc-minute global relief model: procedures, data sources and analysis. NOAA Technical Memorandum NESDIS NGDC-24. *National Geophysical Data Center, NOAA*, *10*, doi: 10.7289/V5C8276M.

Carnes, M. R. (2009). *Description and evaluation of GDEM-V 3.0* (Tech. Rep.). Naval Research Laboratory.

Davies, D., Kelly, E. J., & Filson, J. R. (1971). Vespa process for analysis of seismic signals. *Nature Phys. Sci.*, *232*(27), 8–13, doi: 10.1038/physci232008a0.

de Groot-Hedlin, C. D., & Orcutt, J. A. (2001). Excitation of *T*-phases by seafloor scattering. *J. Acoust. Soc. Am.*, *109*(5), 1944–1954, doi:10.1121/1.1361057.

Dziewoński, A. M., & Anderson, D. L. (1981). Preliminary Reference Earth Model. *Phys. Earth Planet. Inter.*, *25*, 297–356, doi: 10.1016/0031-9201(81)90046-7.

Forget, G., Campin, J.-M., Heimbach, P., Hill, C. N., Ponte, R. M., & Wunsch, C. (2015). ECCO version 4: An integrated framework for non-linear inverse modeling and global ocean state estimation. *Geosci. Model. Dev.*, *8*, 3071–3104, doi: 10.5194/gmd-8-3071-2015.

Gibbons, S. J. (2022). The hydroacoustic network of the CTBT International Monitoring System: Access and exploitation. *J. Peace Nucl. Disarm.*, *5*(2), 452–468, doi: 10.1080/25751654.2022.2129948.

Heaney, K. D., Kuperman, W. A., & McDonald, B. E. (1991). Perth–Bermuda sound propagation (1960): Adiabatic mode interpretation. *J. Acoust. Soc. Am.*, *90*(5), 2586–2594, doi: 10.1121/1.402062.

Kennett, B. L. N. (1995). Approximations for surface-wave propagation in laterally varying media. *Geophys. J. Int.*, *122*, 470–478.

Kennett, B. L. N., Engdahl, E. R., & Buland, R. (1995). Constraints on seismic velocities in the Earth from traveltimes. *Geophys. J. Int.*, *122*(1), 108–124, doi: 10.1111/j.1365-

246X.1995.tb03540.x.

McDougall, T. J., & Barker, P. M. (2011). *Getting started with TEOS-10 and the Gibbs Seawater (GSW) oceanographic toolbox*. SCOR/IAPSO WG127.

Porter, M. B. (1992). *The KRAKEN normal mode program. saclant undersea research centre memorandum (sm-245)* (Vol. Mem. Rep. 6920; Tech. Rep.). La Jolla, CA: Naval Research Laboratory.

Roquet, F., Madec, G., McDougall, T. J., & Barker, P. M. (2015). Accurate polynomial expressions for the density and specific volume of seawater using the TEOS-10 standard. *Ocean Modelling*, *90*, 29–43, doi: 10.1016/j.ocemod.2015.04.002.

Simon, J. D., Simons, F. J., & Irving, J. C. E. (2022). Recording earthquakes for tomographic imaging of the mantle beneath the South Pacific by autonomous MERMAID floats. *Geophys. J. Int.*, *228*(1), 147–170, doi: 10.1093/gji/ggab271.

Thurin, J., & Tape, C. (2023). Comparison of force and moment tensor estimations of subevents during the 2022 Hunga–Tonga submarine volcanic eruption. *Geophys. J. Int.*, *235*(2), 1959–1981, doi: 10.1093/gji/ggad323.

Weatherall, P., Marks, K. M., Jakobsson, M., Schmitt, T., Tani, S., Arndt, J. E., ... Wigley, R. (2015). A new digital bathymetric model of the world's oceans. *Earth Space Sci.*, *2*(8), 331–345, doi: 10.1002/2015EA000107.

Table S1. (*caption next page*)

Network	Receiver	Latitude (°)	Longitude (°)	Receiver Depth (m)	Ocean Depth (m)	Distance (km)	Azimuth (°)	Category
MH	P0054	-28.493	-171.993	1500	5232	948	159	A
MH	P0045	-25.295	-165.846	1500	5640	1110	120	A
MH	P0042	-29.848	-170.141	1500	5281	1161	154	A
MH	P0049	-30.553	178.669	1500	3734	1262	207	C
MH	P0048	-29.421	173.488	1000	2838	1492	226	A
MH	P0041	-27.382	-161.753	1500	5039	1579	121	A
MH	P0053	-29.972	-157.878	1500	5234	2045	124	A
MH	P0023	-27.977	-156.395	1500	5455	2092	117	A
MH	P0040	-29.232	-154.043	1500	5232	2355	118	A
MH	P0028	-8.786	-150.085	1500	4998	3013	68	B
MH	N0002	-2.023	-155.005	1500	4852	3022	50	A
MH	P0026	-11.632	-147.223	1500	4603	3162	76	B
MH	P0036	-22.235	-142.464	1500	3811	3408	99	B
MH	P0016	-11.810	-144.311	500	4937	3451	79	B
MH	P0022	-23.356	-140.723	1250	4561	3581	101	B
MH	P0035	-16.440	-141.518	1500	2917	3595	88	C
MH	P0017	-11.936	-140.596	1000	4113	3827	81	B
MH	N0001	1.692	-146.962	1500	4524	3962	55	A
MH	P0025	-23.053	-136.041	1500	4150	4060	101	C
MH	P0018	-13.293	-136.424	1250	4230	4213	85	C
IM	H11S2	18.490	166.705	742	1148	4759	335	A
IM	H11S3	18.495	166.687	726	1155	4760	335	A
IM	H11S1	18.508	166.700	750	1183	4761	335	A
MH	P0021	-21.605	-129.185	1000	4116	4778	100	B
IM	H11N3	19.718	166.910	729	1318	4874	336	A
IM	H11N1	19.714	166.891	731	1099	4875	336	A
IM	H11N2	19.731	166.897	721	1397	4876	336	A
MH	P0019	-14.157	-125.241	500	4888	5350	91	C
MH	N0004	-17.597	-118.668	1500	3611	5941	97	B
MH	N0005	-21.672	-104.669	1500	3860	7268	105	C
IM	H03S3	-33.8	-78.9	800	1960	9326	124	A
IM	H03S2	-33.8	-78.8	800	2113	9326	124	A
IM	H03S1	-33.8	-78.8	800	1891	9328	124	A
IM	H03N2	-33.4	-78.9	800	2804	9332	124	A
IM	H03N1	-33.5	-78.9	800	2926	9333	124	A

Table S1. (*previous page*) Receivers used in this study, their location and underwater depth, and their great-circle distances and azimuths from the HTHH event. While we used the most exact and up-to-date coordinates, not all are publicly available (Gibbons, 2022). For those (H03) we provide only rounded coordinates. Ocean depths are from GEBCO_2014 (Weatherall et al., 2015), which may differ greatly from those reported by the IMS (see Table S2). Azimuth is measured positive clockwise from due North. The final column lists our *T*-wave signal categorization defined in the Main Text, with A ("well defined") clearly peaked in its time-domain envelope, B ("diffuse") lacking defined onsets but displaying smooth-envelope "rumble," and C ("undetected") exhibiting no clear signal.

Table S2. (*current page*) Ocean depths (m) reported by GEBCO_2014 (Weatherall et al., 2015), the IMS, and their average per-triad differences, which can be substantial in some cases. H03N3 was malfunctioning during the study period and not used, but is retained here for completeness. Note that IMS bathymetric data were only available at specific IMS receiver locations, while GEBCO models bathymetry within the entire Pacific, hence we used the later for this study, but quote the former to illustrate that we have imperfect knowledge of ocean depths.

Station	GEBCO	IMS	Difference	Average
H03N1	2926	1538	1388	
H03N2	2804	2060	744	745
H03N3	2105	2003	102	
H03S1	1891	2040	-149	
H03S2	2113	2160	-47	-82
H03S3	1960	2011	-51	
H11N1	1099	1418	-319	
H11N2	1397	1427	-30	-155
H11N3	1318	1433	-115	
H11S1	1183	1179	4	
H11S2	1148	1197	-49	-12
H11S3	1155	1146	9	

Table S3. Model performance for our occlusion counting scheme, $L_{p^*} = \beta_1 \log_{10}(\Lambda_\Phi + 1) + \beta_0$, at a range of clearance ratios, Φ. The final column lists relative performance in terms of R^2 fit compared to the case when $\Phi = 1.0$, i.e., considering the full Fresnel width.

Φ	β_1	β_0	R^2	Rel. %
0.0	-6.0	-4.4	0.70	79.5
0.1	-5.8	-4.2	0.71	80.7
0.2	-5.6	-4.1	0.71	80.7
0.3	-5.8	-3.4	0.77	87.5
0.4	-5.9	-2.9	0.82	93.2
0.5	-5.9	-2.6	0.85	96.6
0.6	-5.9	-2.5	0.86	97.7
0.7	-5.8	-2.5	0.86	97.7
0.8	-5.7	-2.3	0.87	98.8
0.9	-5.7	-2.2	0.88	100.0
1.0	-5.6	-2.2	0.88	100.0

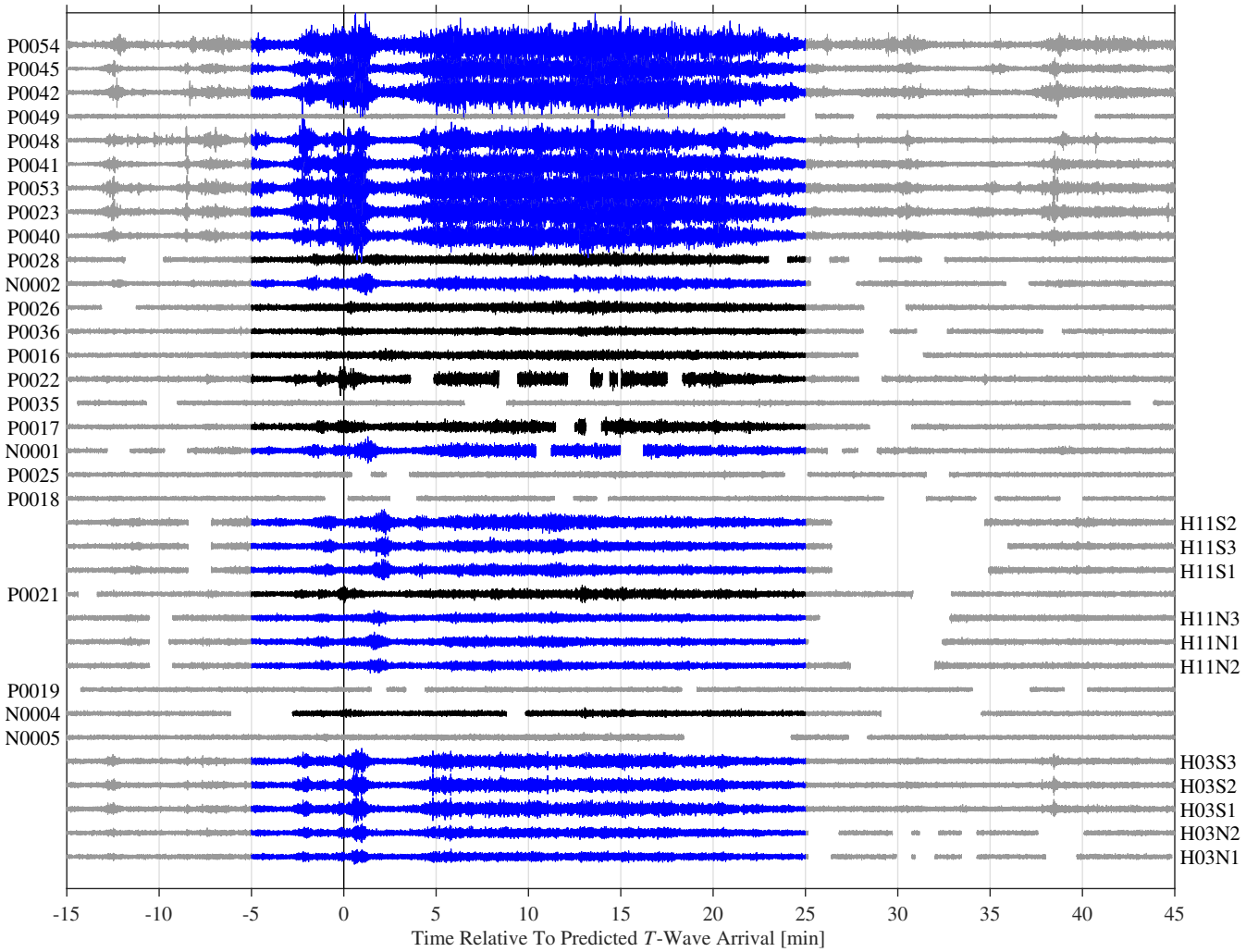

Figure S1. Data as in Figure 2 of the Main Text but with receivers reordered from top to bottom by increasing epicentral distance.

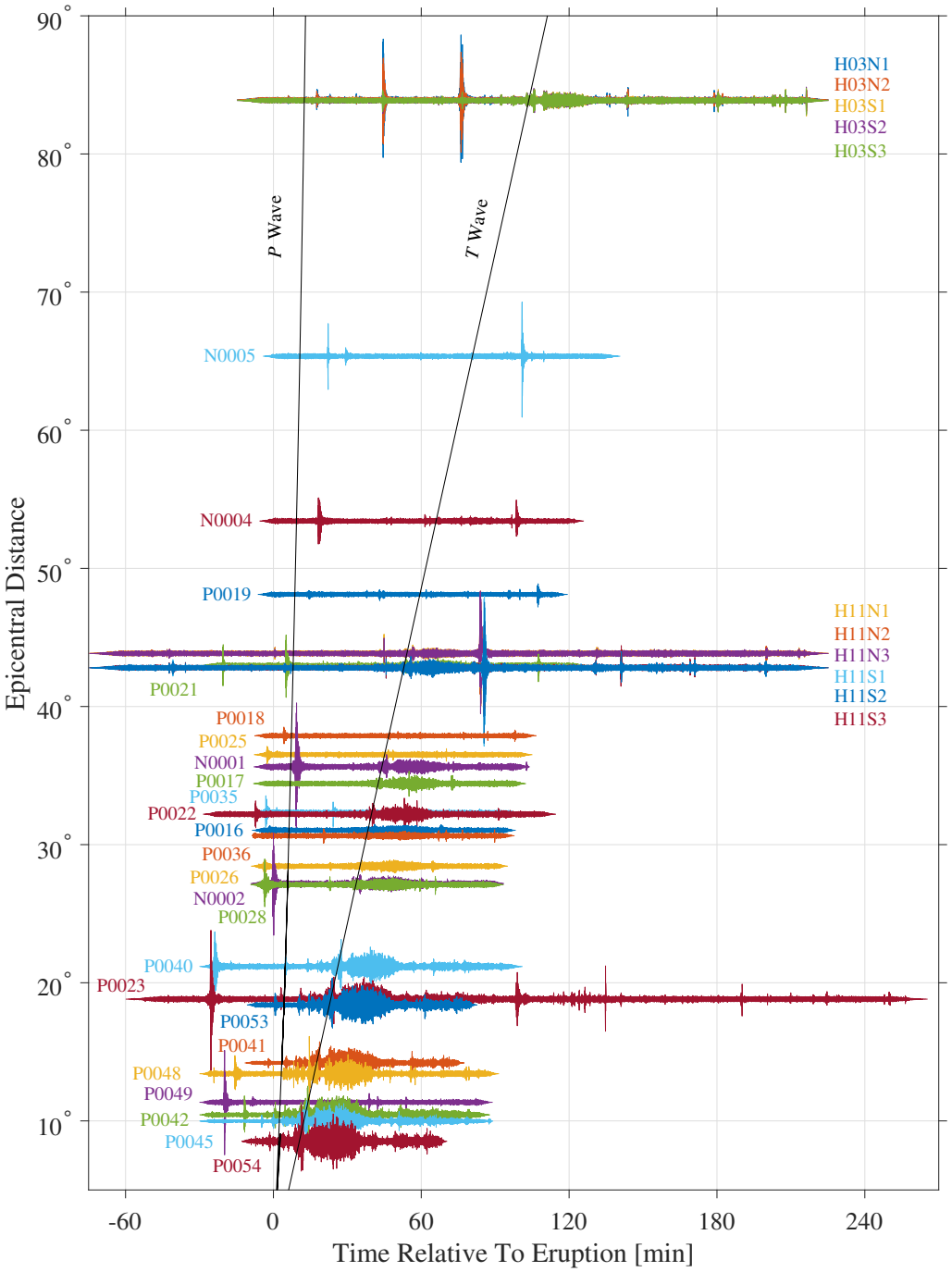

Figure S2. Record section with traces normalized like Figure 2 of the Main Text, but without local events removed, and in different colors. Position on the vertical axis corresponds to epicentral distance and timing on the horizontal axis is relative to the USGS origin `us7000gc8r` for the HTHH eruption. *P*-wave arrival times are predicted using Earth model ak135 (Kennett, 1995). Additional signals moving at the speed of sound in water are clearly visible before and after the main 30-minute *T* wave analyzed in this study.

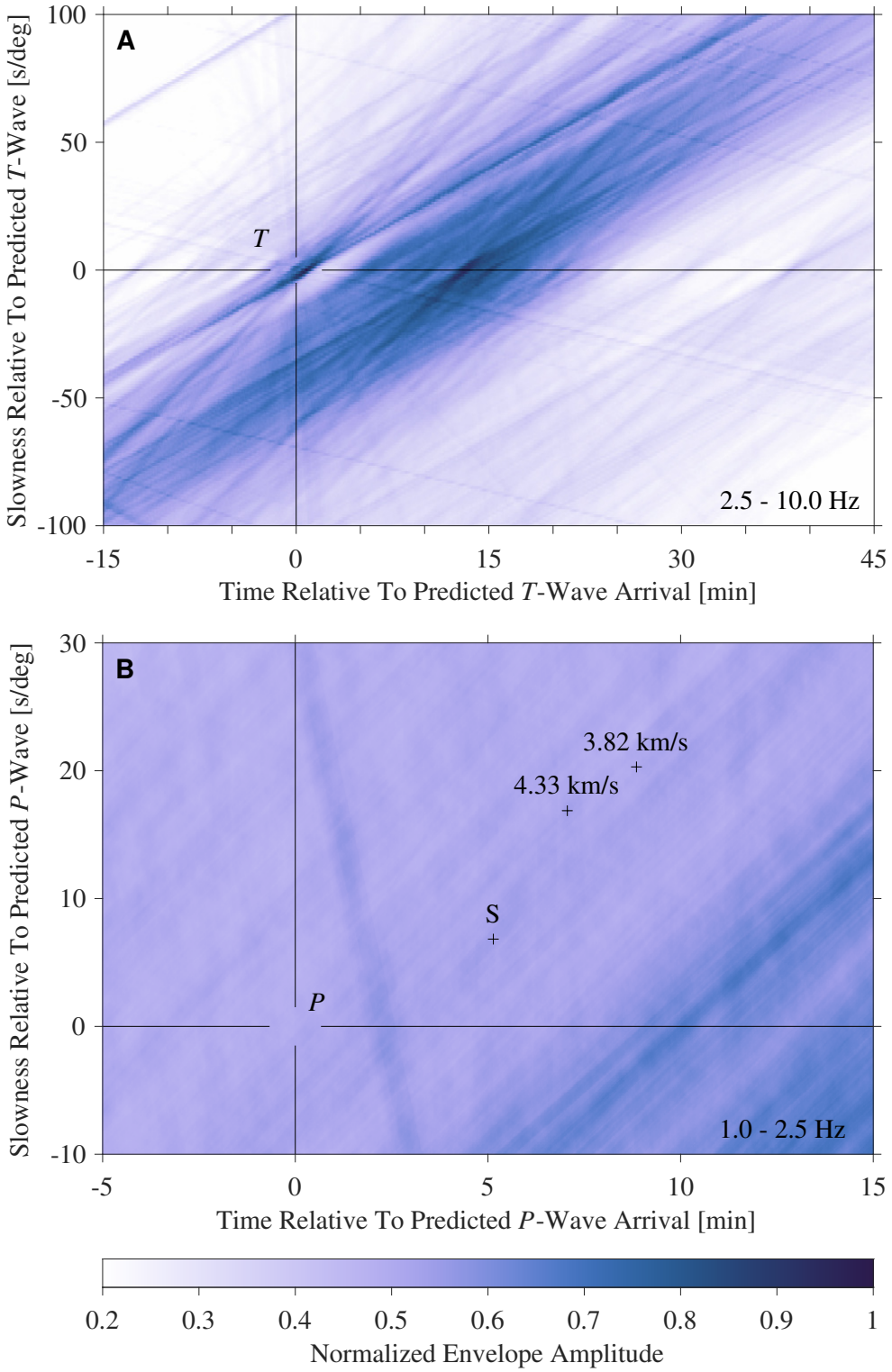

Figure S3. Vespagrams made from 30 s RMS waveform envelopes in two time-frequency windows, plotted relative to the predicted slowness and timing of the predicted *T* wave in (A), and *P* wave in (B). Most of the energy is concentrated in two bursts at the slowness of the *T* wave, while no clear *P* wave is detected, nor is there any evidence of *S* or surface waves, whose timings and slownesses are included as crosshairs for reference only.

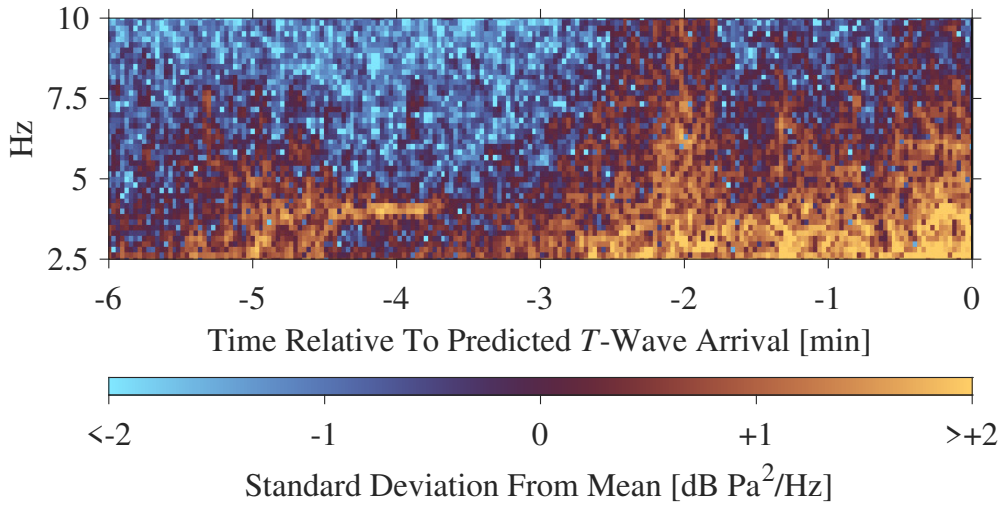

Figure S4. Zoom into Figure 3 of the Main Text highlighting six minutes around the time of the HTHH eruption, showing what we interpret as possibly 'gliding' tremor, followed by a brief pause, preceding the eruption.

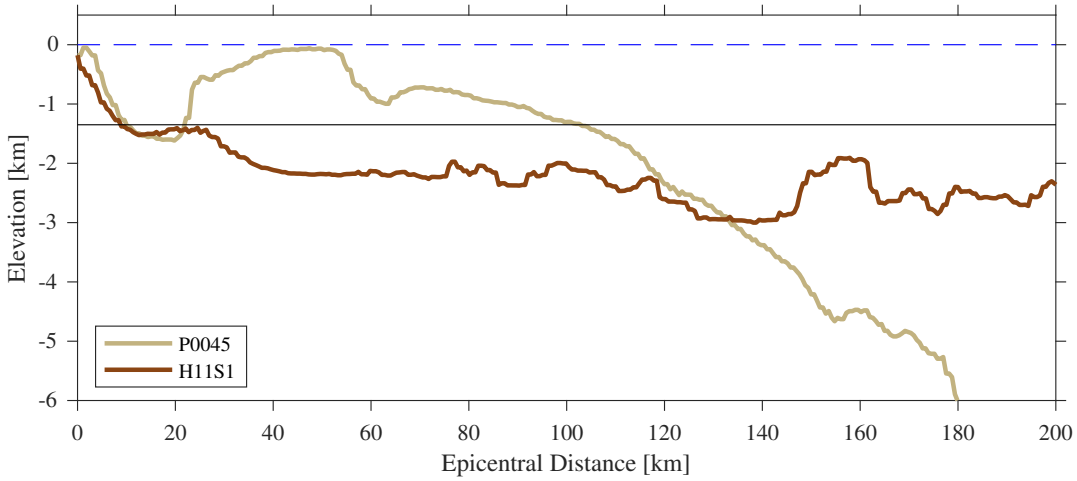

Figure S5. First 200 km of bathymetry along great-circle paths (GCP) to receivers P0045 and H11S1 (note that in the Main Text, and later in this Supporting Information, bathymetric profiles taken along GCP paths are colored red). The dashed blue line marks the sea surface. The solid black line at −1350 m marks the depth of the maximum of the fundamental-mode pressure eigensolution (where we count occluders), and its intersection with the open ocean after the trench (around 100 km from the source for the path to P0045) is the location of *P*-to-*T*-wave conversion in our first-order time correction.

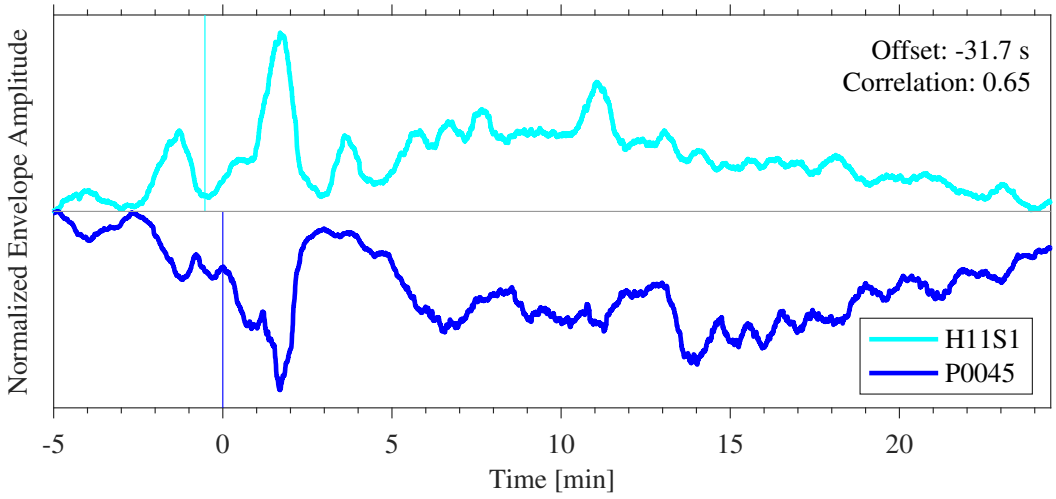

Figure S6. Envelope correlation and adjusted offset after making the first-order travel-time adjustment described in Section S2 and Figure S5. The minor difference in correlation coefficient compared to the Main Text is due to the slightly different (shifted) 30-minute windows considered.

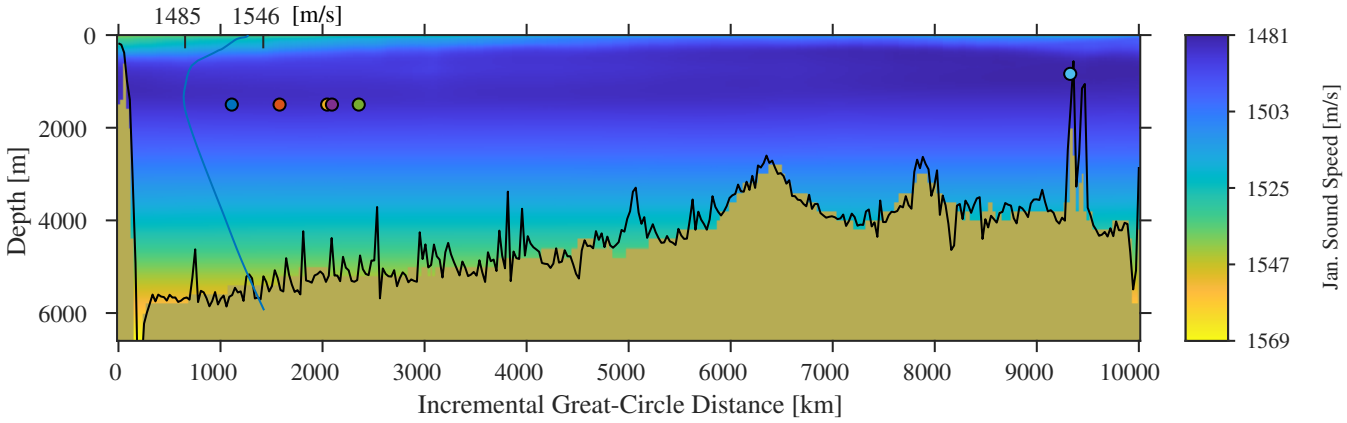

Figure S7. Cross-section of the bathymetry along the oceanic great-circle path between HTHH (at the left) and IMS station cluster H03 (H03S1 is plotted at the far right), with color rendering of the sound wave speed in the GDEM-V 3.0 model (Carnes, 2009) for a generic January. Projected onto the path, from left to right at 1500 m depth, are the receiving locations of MERMAID floats P0045, P0041, P0053, P0023, and P0040 (colored circles, representing receivers at similar azimuths; see Figure 1 in the Main Text). The blue curve is the local sound-speed profile at the location of P0045 with minimum and maximum speeds marked above the curve.

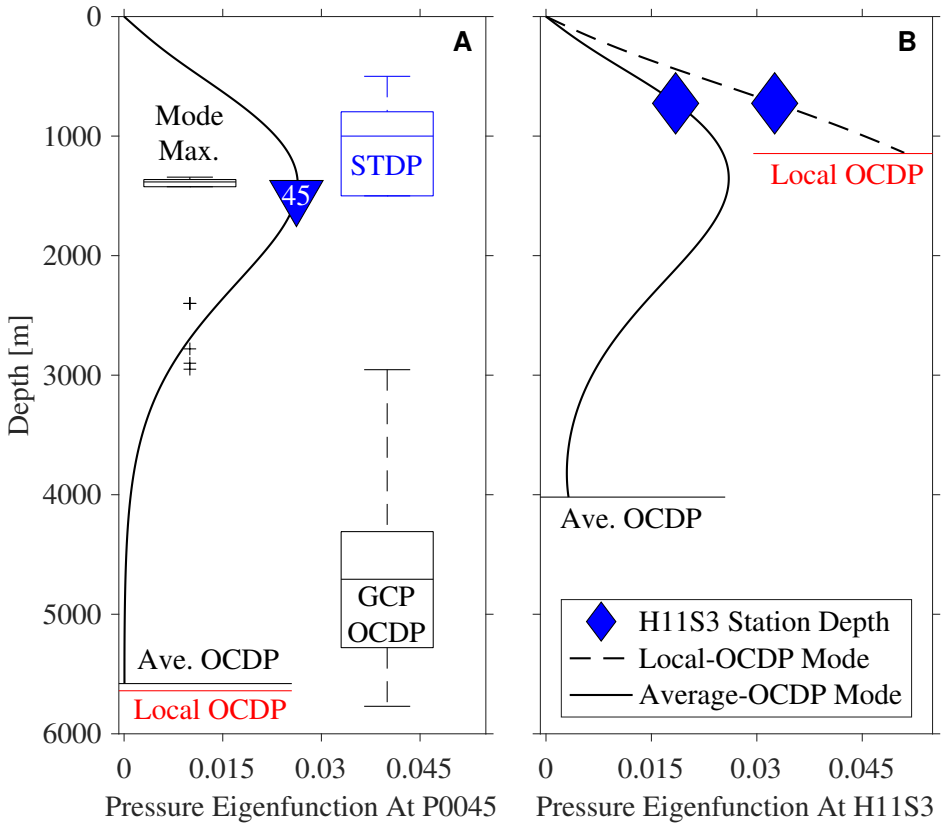

Figure S8. Sound pressure eigenfunctions for two stations for a 2.5 Hz fundamental acoustic mode propagating in one-dimensional ocean models of different depths over a seafloor with material properties of the PREM crust (Dziewoński & Anderson, 1981). Solid black curves were obtained via averaging of the ECCO model (Forget et al., 2015), ocean depths, and sound speeds along a 100 km north-south regional transect and computing fundamental-mode acoustic pressure eigenfunctions within the water column. Horizontal lines mark regional average ocean depths (black) and local ocean depths immediately below the receiver (red). (A) The case relevant to MERMAID P0045. Three box plots represent: station depths (STDP); ocean depths (OCDP) averaged across all great-circle propagation (GCP) paths; and depths at which pressure modes like the one shown here reach their maximum (Mode Max., with outliers marked by "+"), for all 29 receivers that reported Category A and B signals. (B) The case relevant to IMS station H11S3 with a dashed black curve showing the pressure mode within its locally shallower water column.

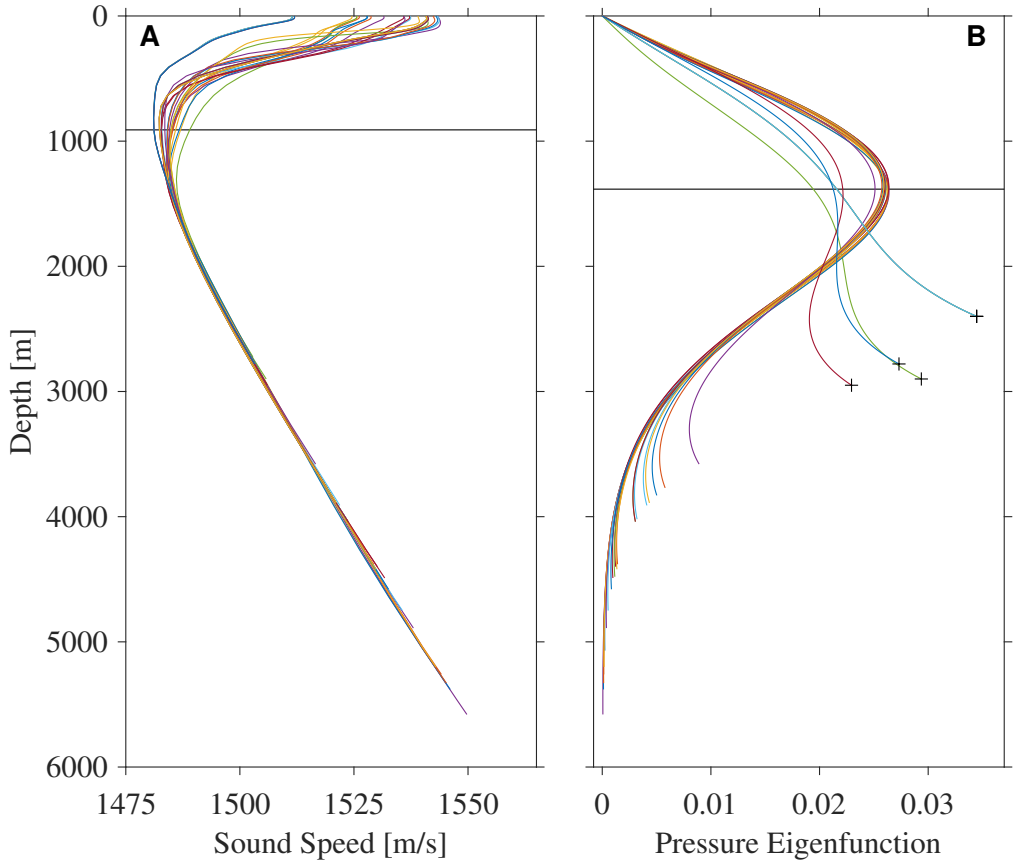

Figure S9. Path-average sound-speed profiles (A) and 2.5 Hz fundamental-mode sound pressure eigenfunctions (B) calculated for regionally averaged ocean depths (over a 100 km north-south transect) as in Figure S8, in the ECCO model (Forget et al., 2015), for all 29 stations recording Category A and B signals. A horizontal line marks the median of the minimum of the sound-speed profiles at 910 m in (A), and the median of the maximum mode pressures at 1384 m in (B). The anomalous eigenfunctions in (B) with maximums at or near the seafloor (marked by "+") correspond to MERMAID P0048 and all five functioning H03 hydrophones with their relatively shallower regionally averaged ocean depths (in total there are six anomalous modes plotted, though some overlap here).

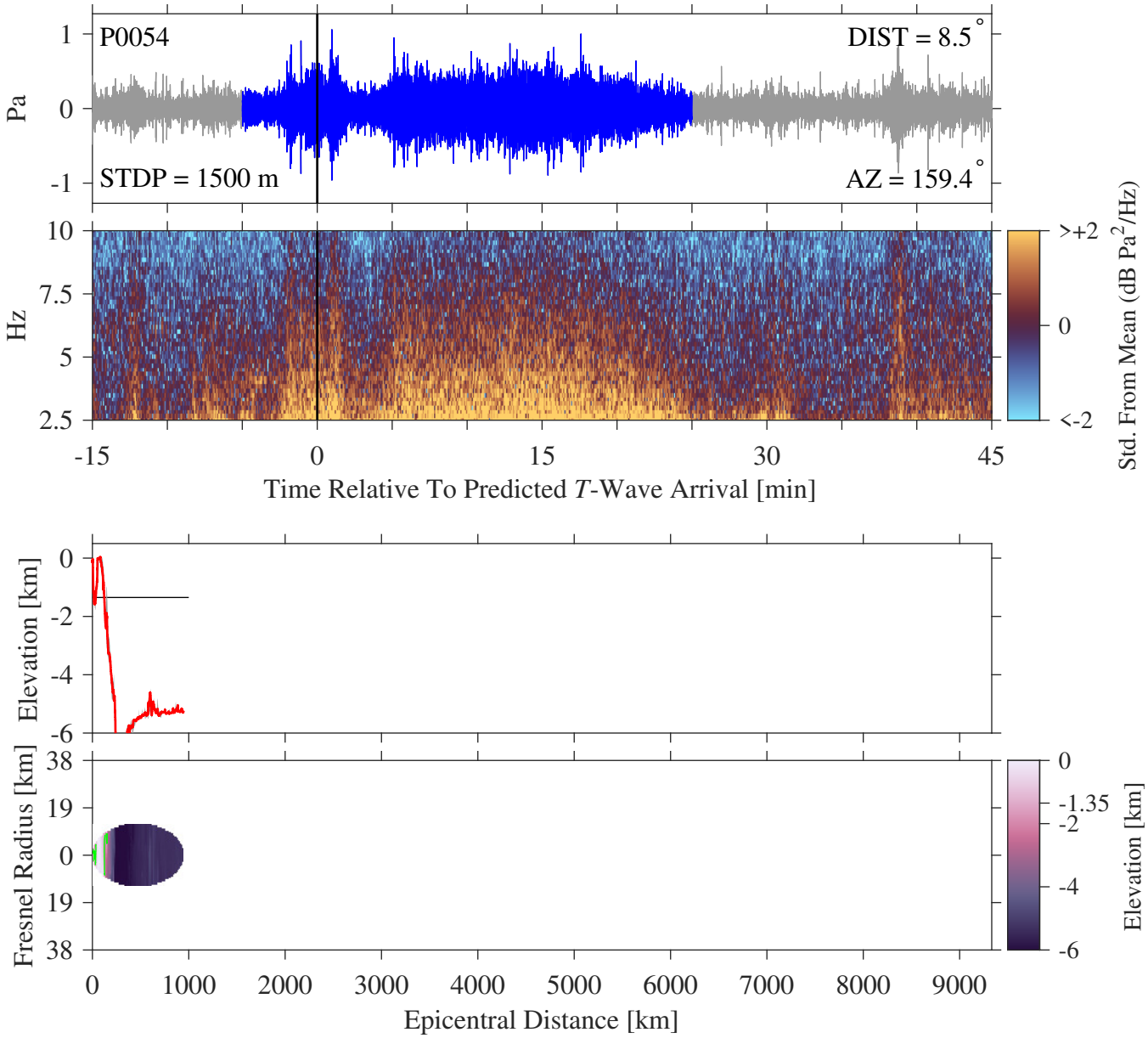

Figure S10. Time and spectral domain signals (two top panels, like Figures 3–4 of the Main Text), and bathymetric profile and map (bottom two panels, like Figure 5 of the Main Text), for MERMAID P0054.

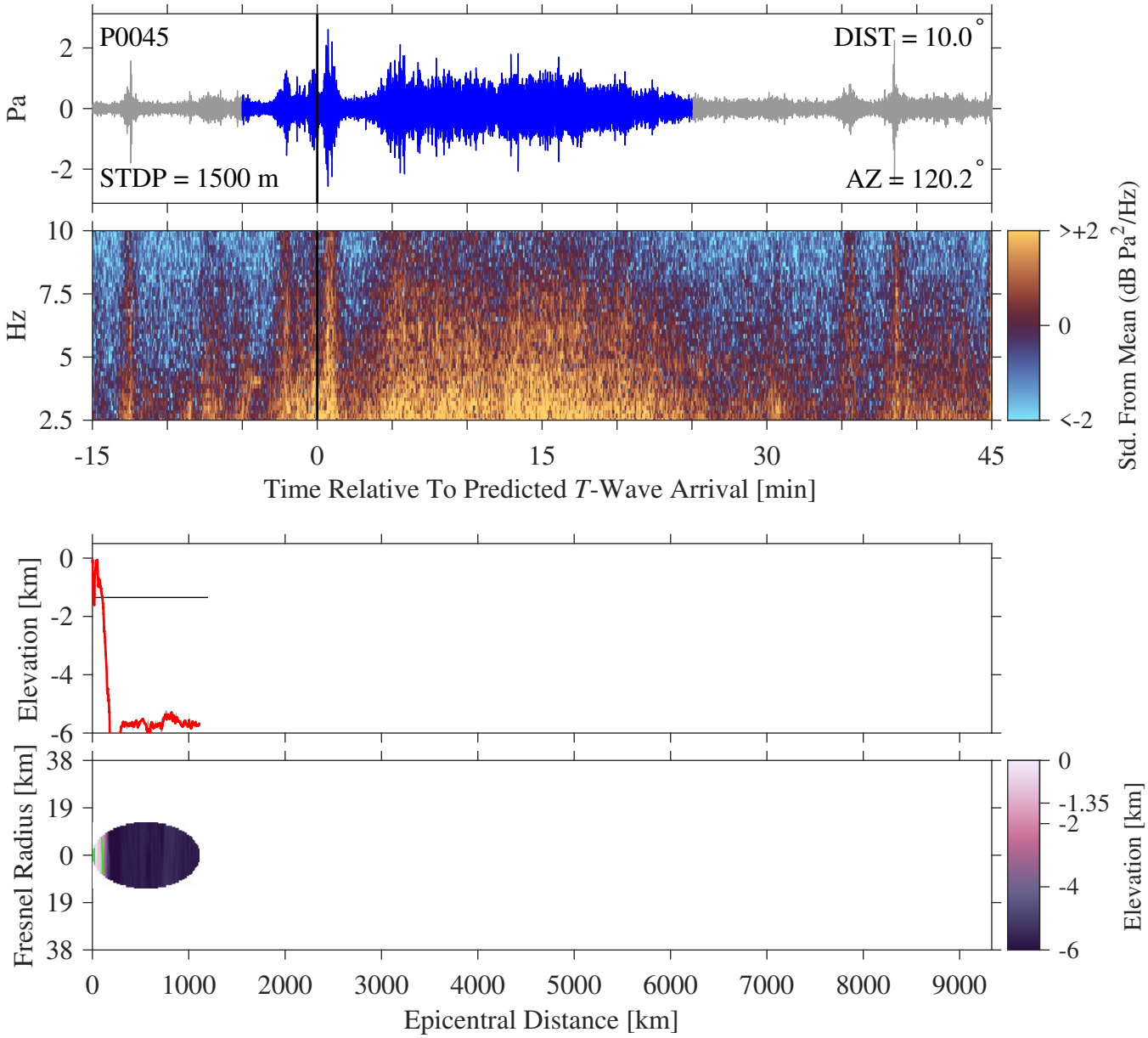

Figure S11. Time and spectral domain signals (two top panels, like Figures 3–4 of the Main Text), and bathymetric profile and map (bottom two panels, like Figure 5 of the Main Text), for MERMAID P0045.

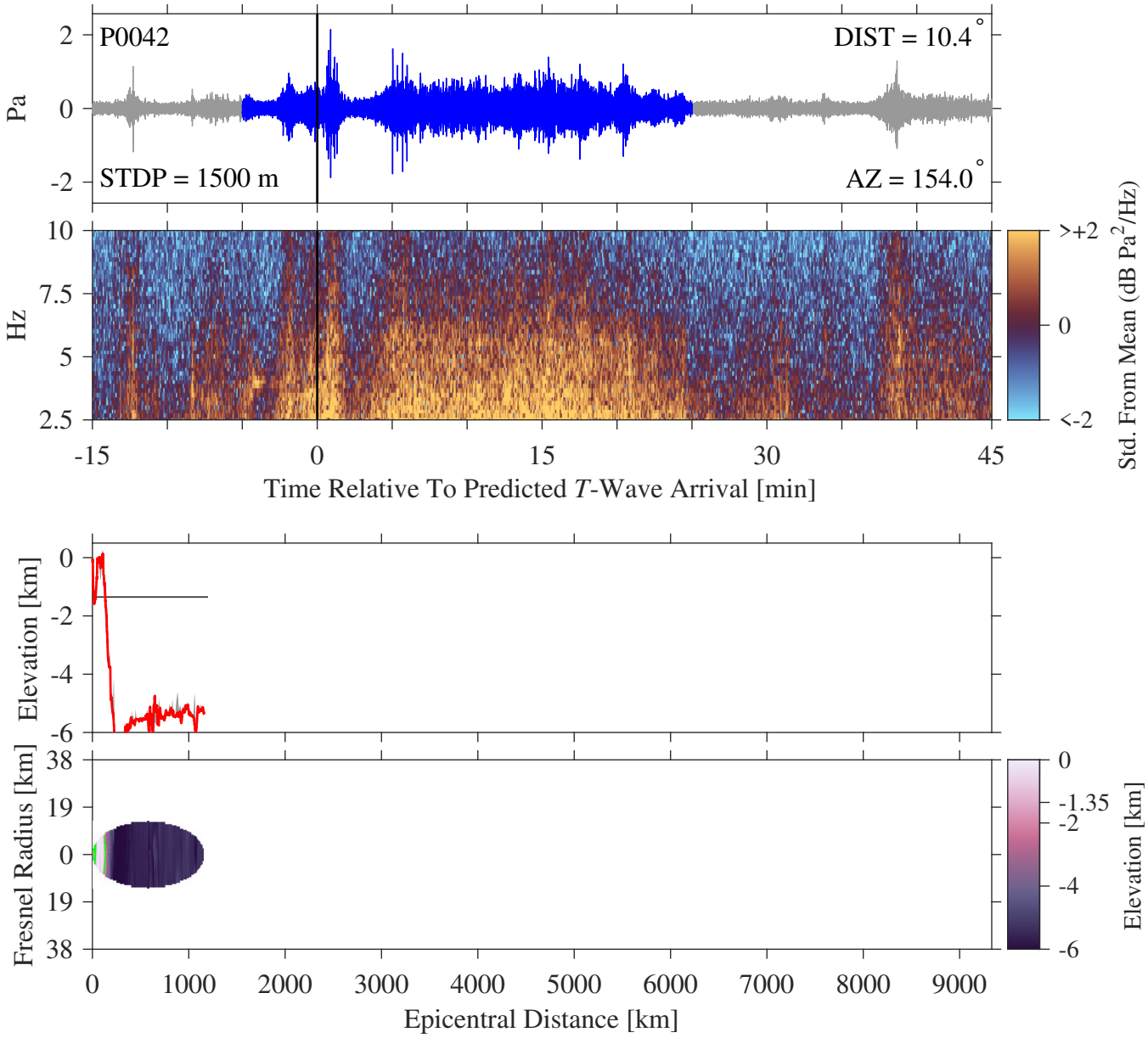

Figure S12. Time and spectral domain signals (two top panels, like Figures 3–4 of the Main Text), and bathymetric profile and map (bottom two panels, like Figure 5 of the Main Text), for MERMAID P0042.

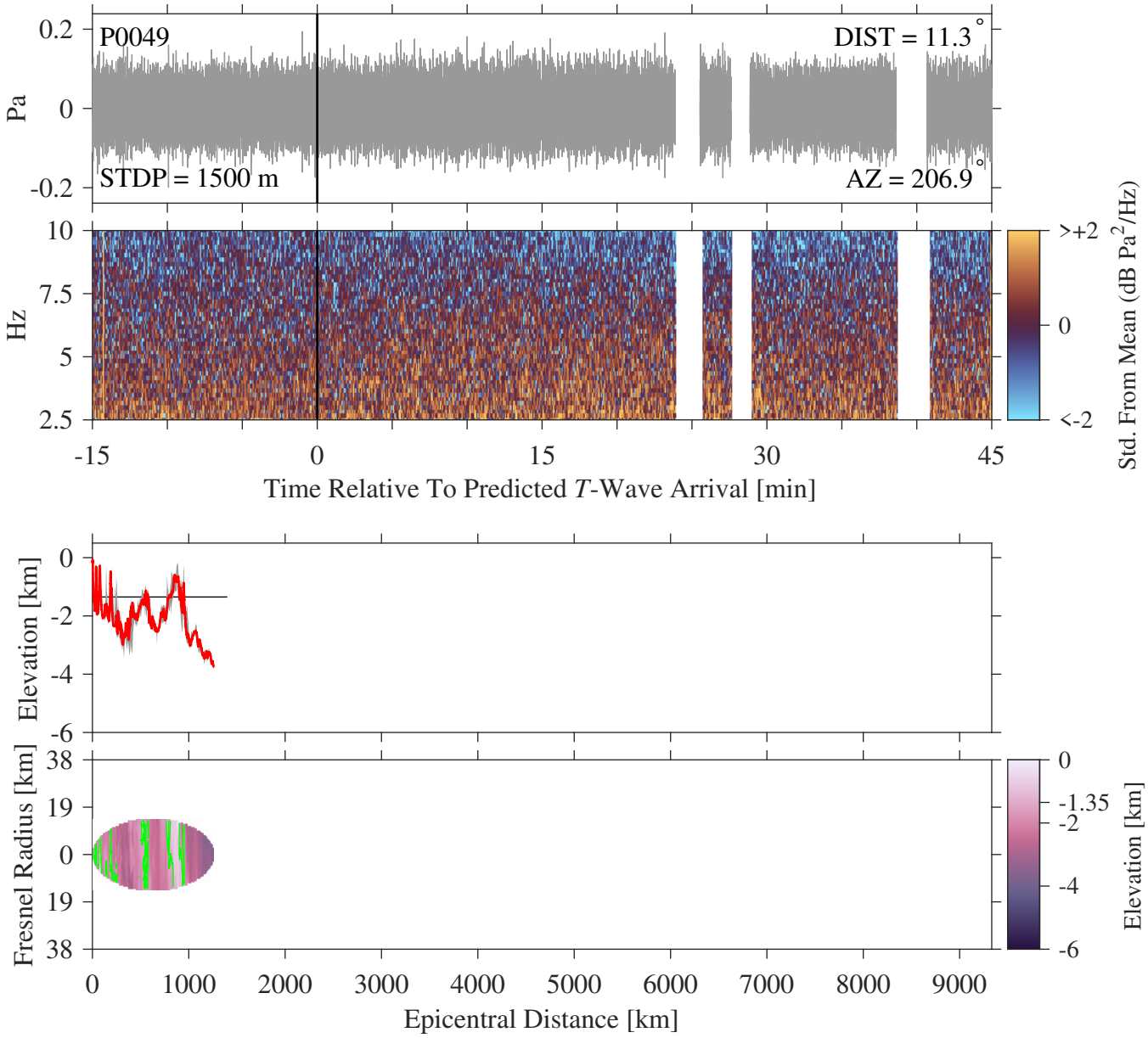

Figure S13. Time and spectral domain signals (two top panels, like Figures 3–4 of the Main Text), and bathymetric profile and map (bottom two panels, like Figure 5 of the Main Text), for MERMAID P0049.

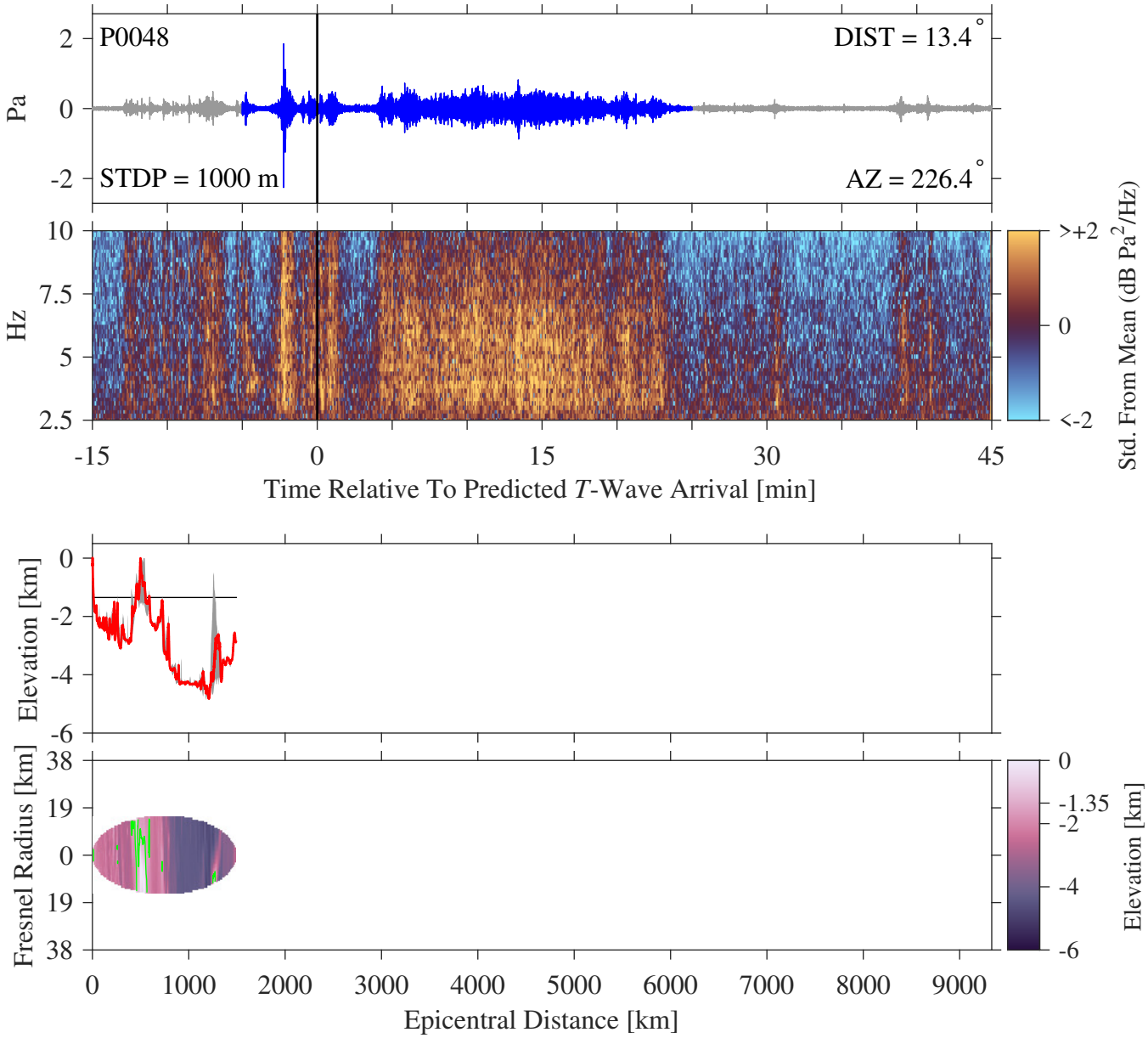

Figure S14. Time and spectral domain signals (two top panels, like Figures 3–4 of the Main Text), and bathymetric profile and map (bottom two panels, like Figure 5 of the Main Text), for MERMAID P0048.

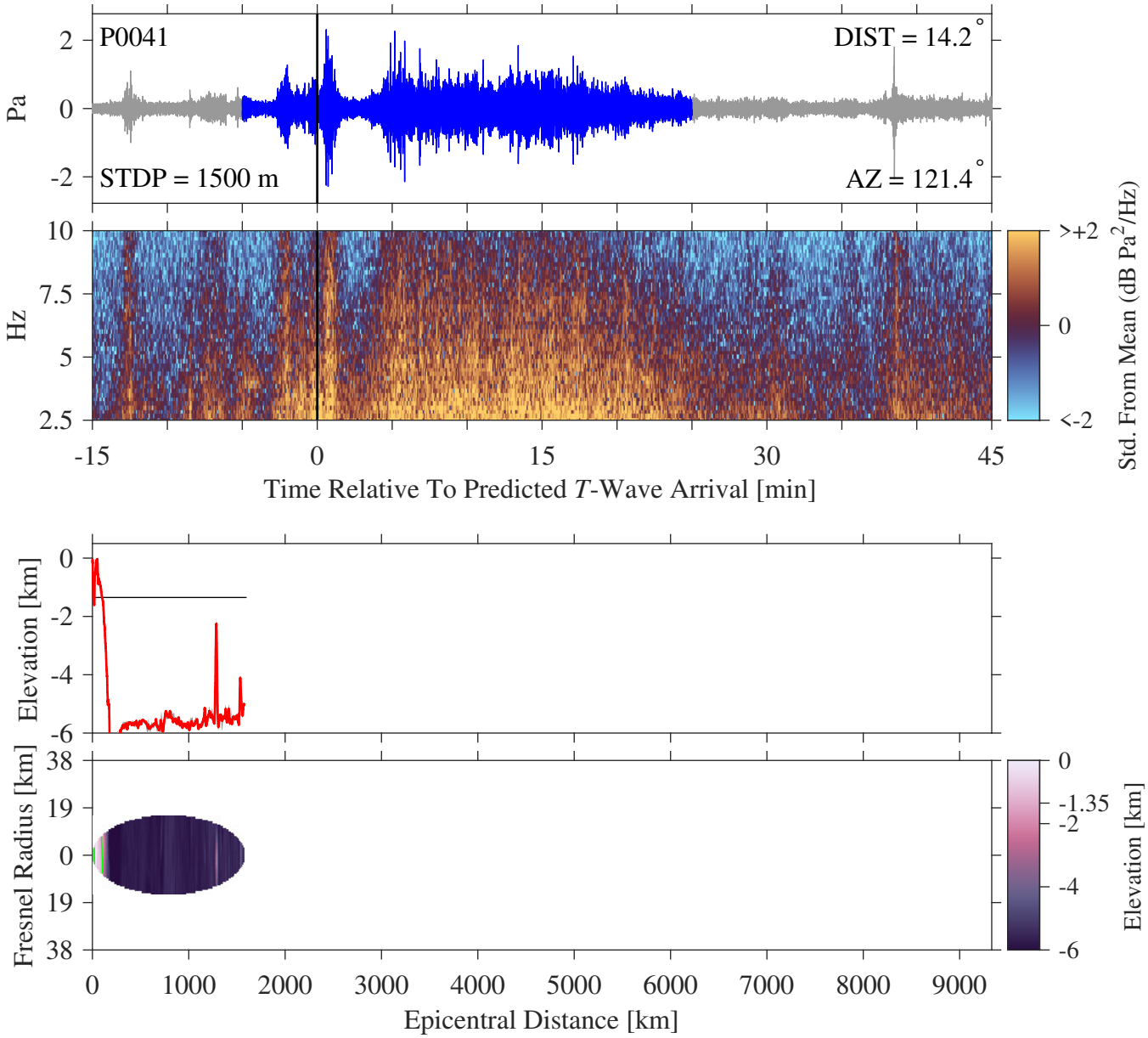

Figure S15. Time and spectral domain signals (two top panels, like Figures 3–4 of the Main Text), and bathymetric profile and map (bottom two panels, like Figure 5 of the Main Text), for MERMAID P0041.

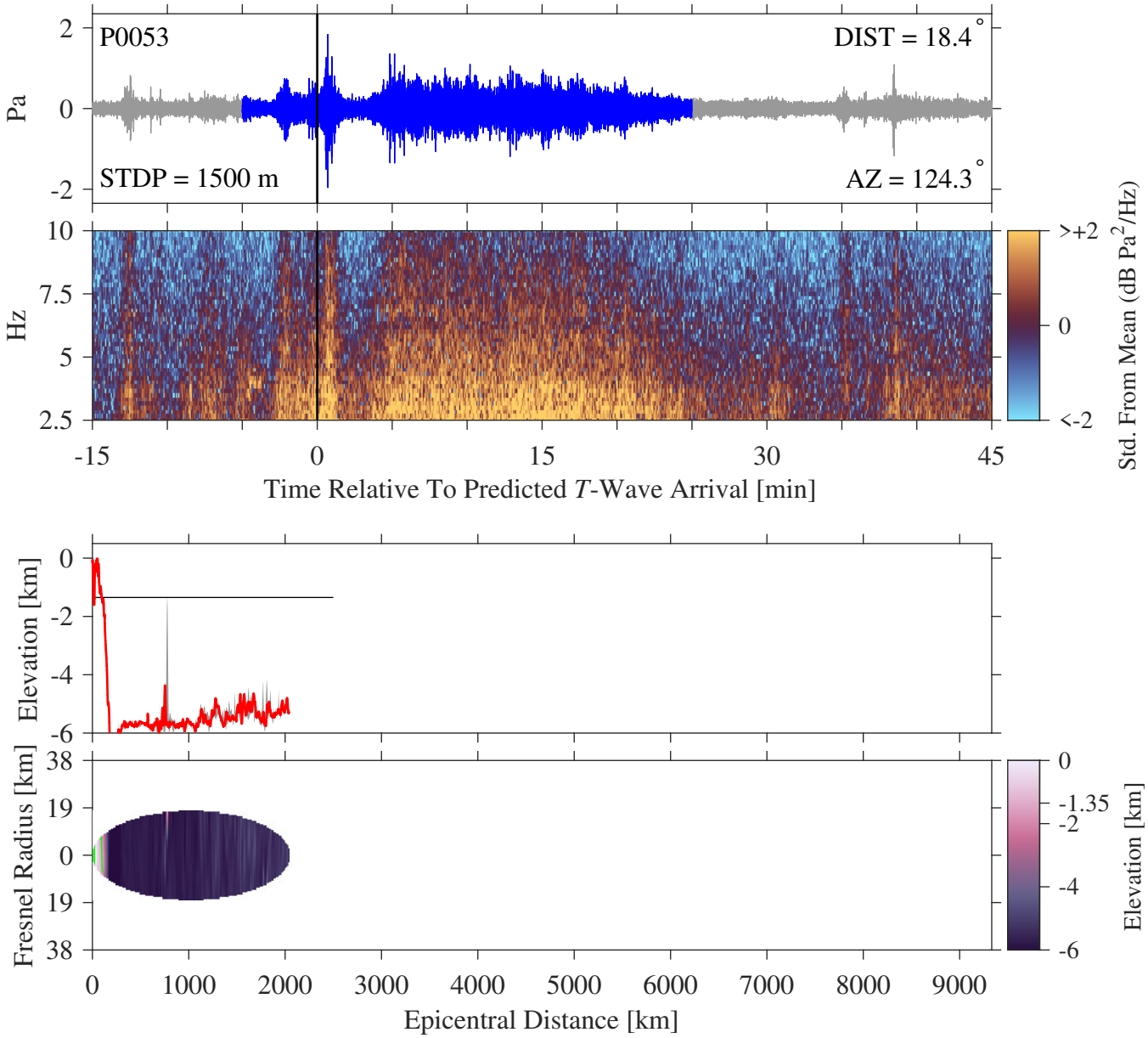

Figure S16. Time and spectral domain signals (two top panels, like Figures 3–4 of the Main Text), and bathymetric profile and map (bottom two panels, like Figure 5 of the Main Text), for MERMAID P0053.

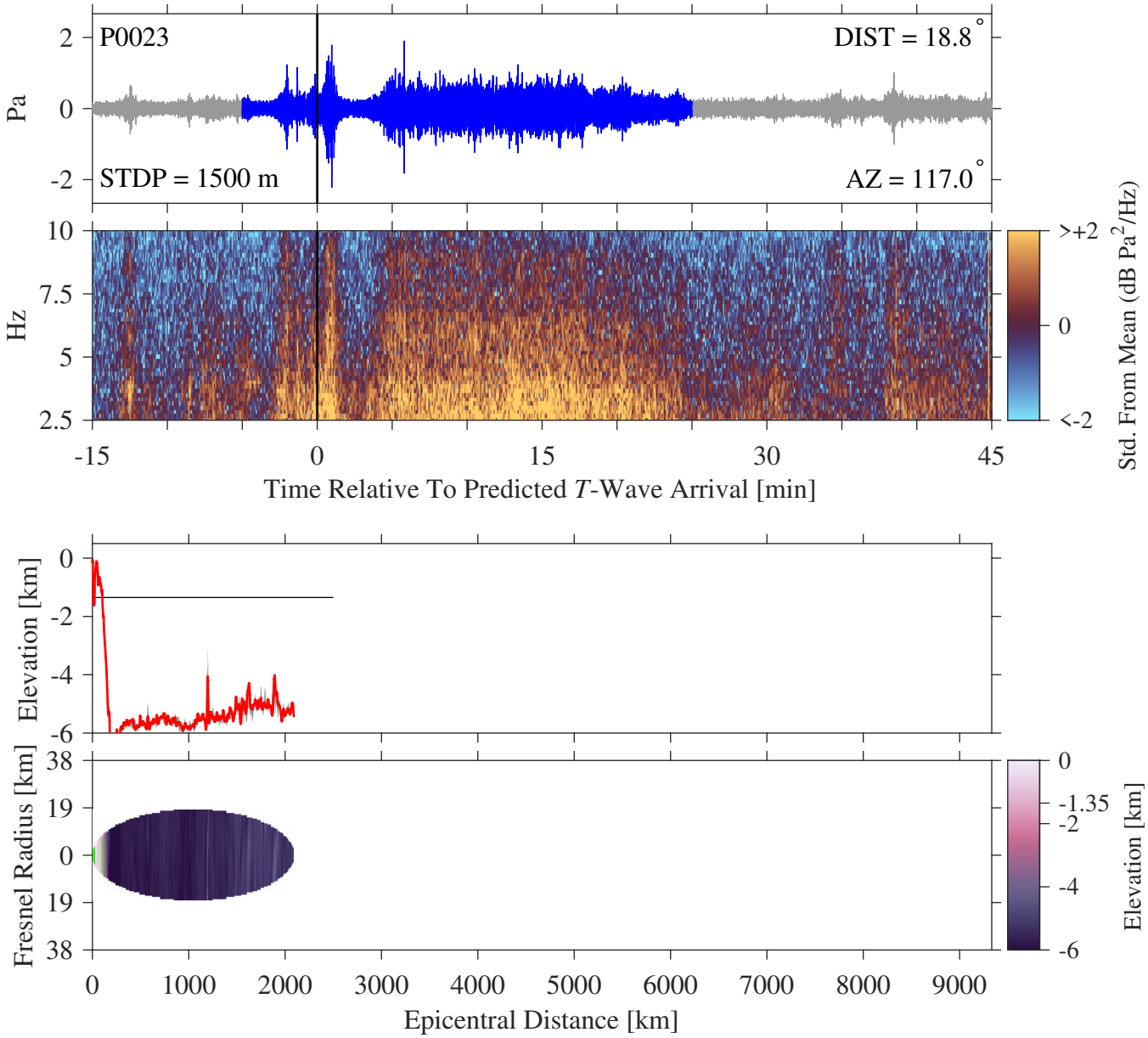

Figure S17. Time and spectral domain signals (two top panels, like Figures 3–4 of the Main Text), and bathymetric profile and map (bottom two panels, like Figure 5 of the Main Text), for MERMAID P0023.

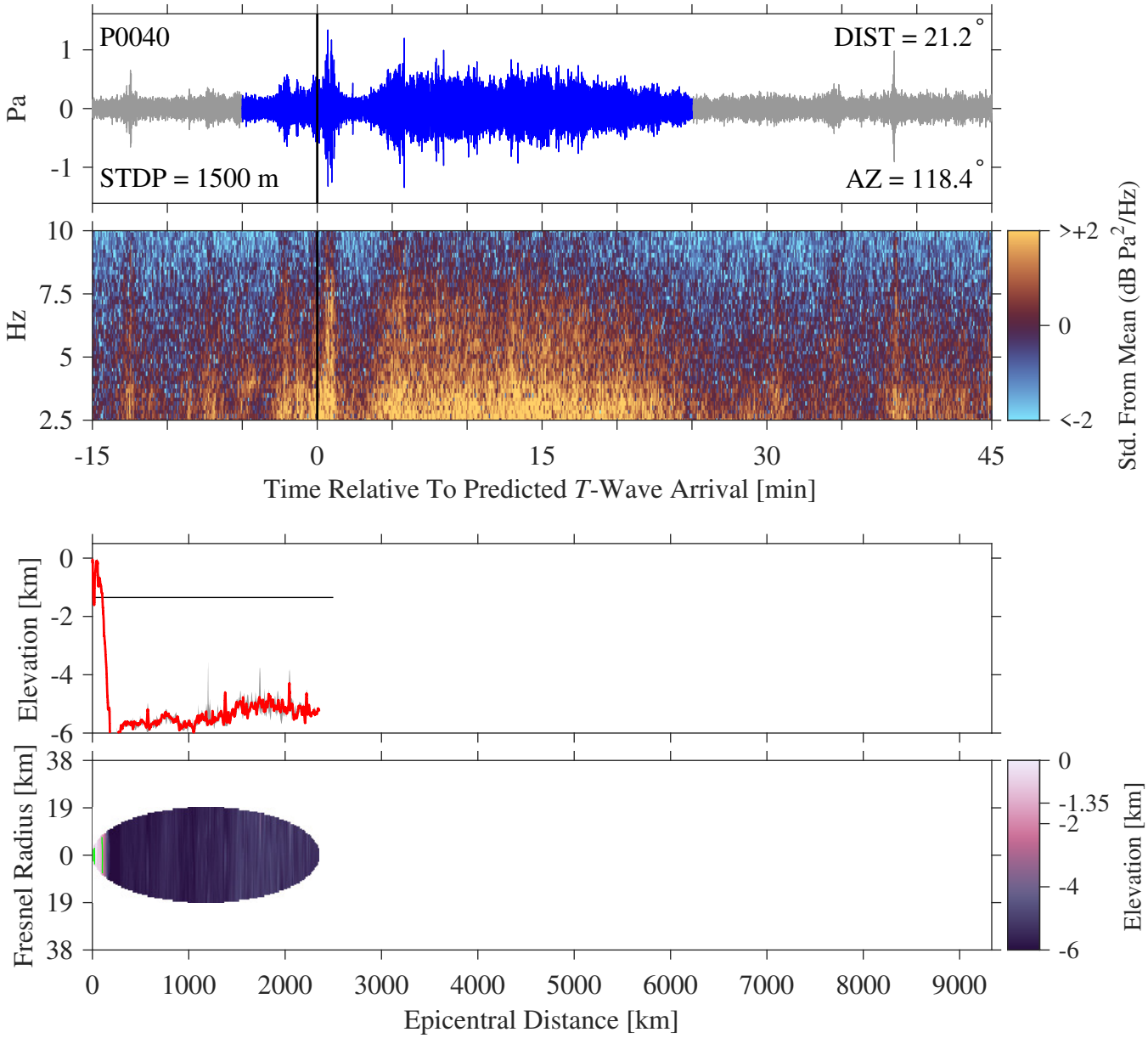

Figure S18. Time and spectral domain signals (two top panels, like Figures 3–4 of the Main Text), and bathymetric profile and map (bottom two panels, like Figure 5 of the Main Text), for MERMAID P0040.

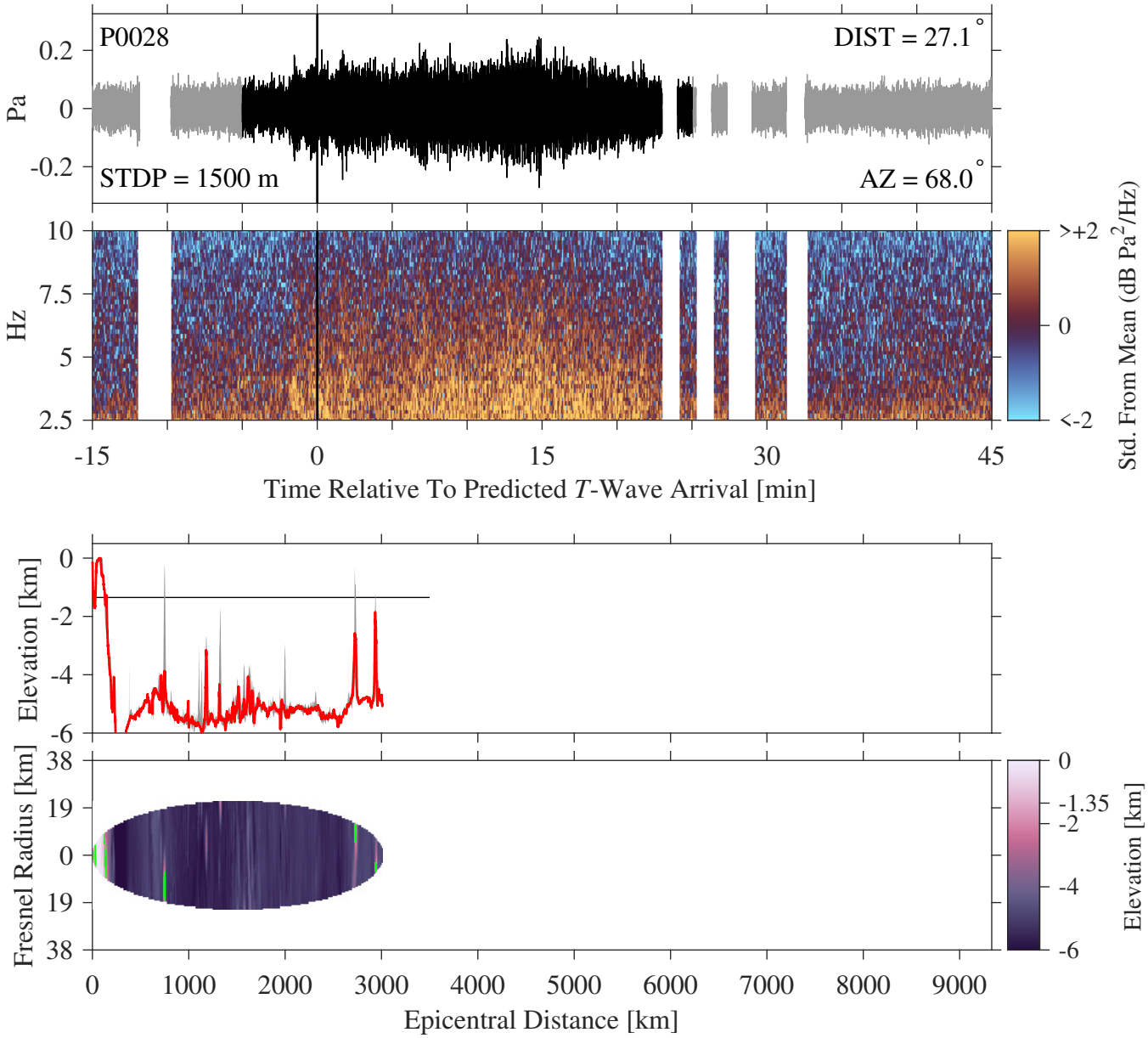

Figure S19. Time and spectral domain signals (two top panels, like Figures 3–4 of the Main Text), and bathymetric profile and map (bottom two panels, like Figure 5 of the Main Text), for MERMAID P0028.

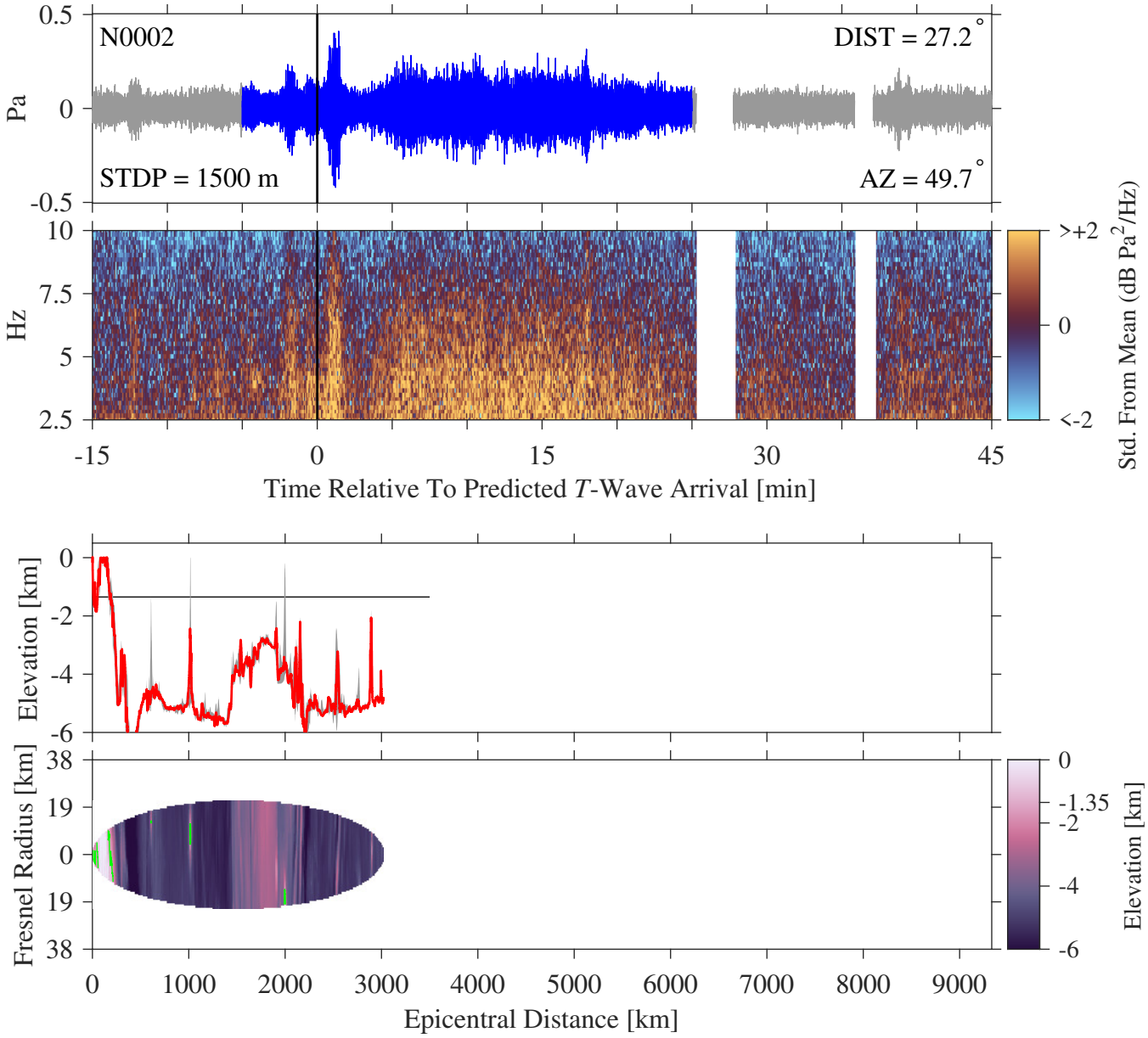

Figure S20. Time and spectral domain signals (two top panels, like Figures 3–4 of the Main Text), and bathymetric profile and map (bottom two panels, like Figure 5 of the Main Text), for MERMAID N0002.

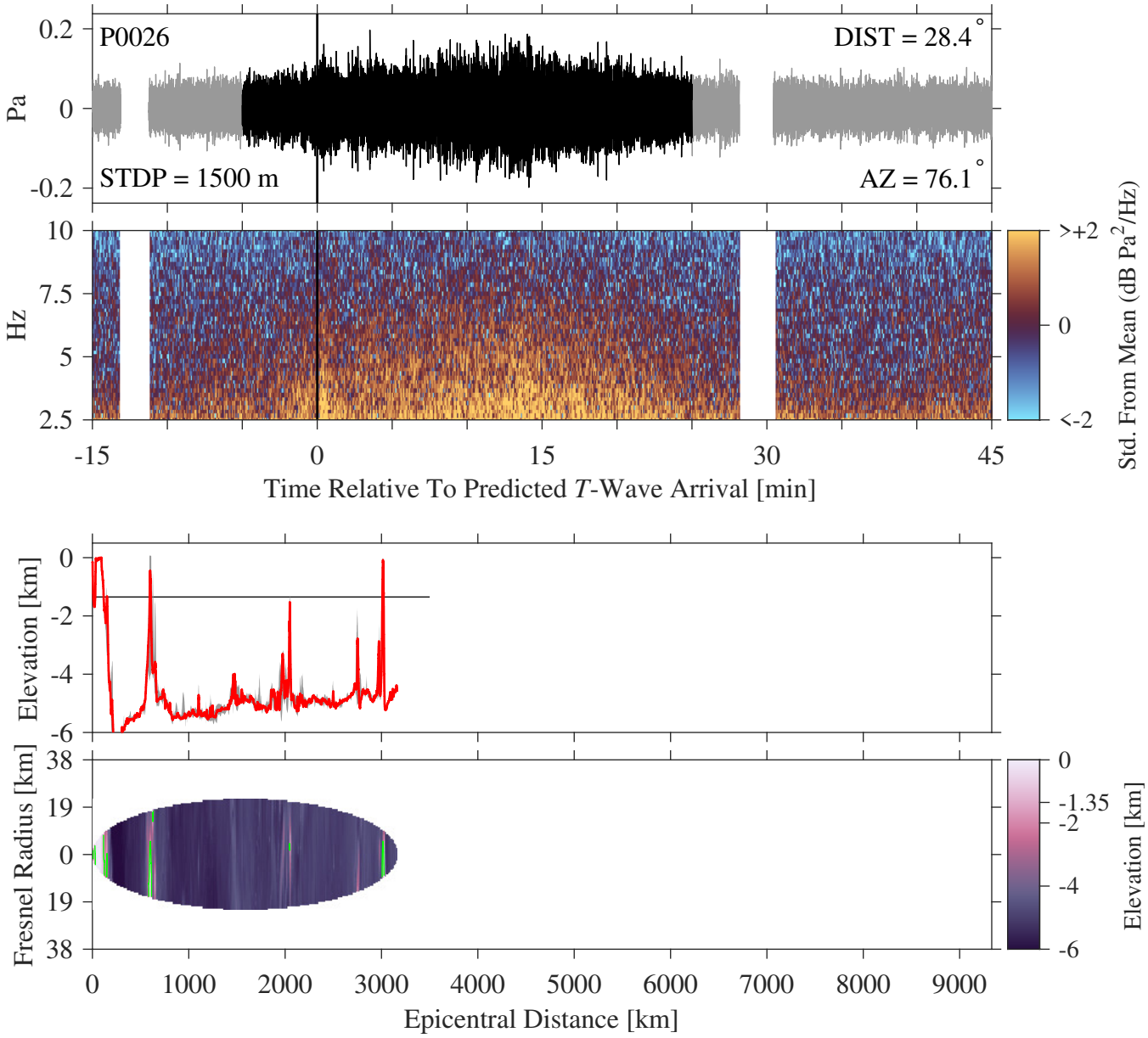

Figure S21. Time and spectral domain signals (two top panels, like Figures 3–4 of the Main Text), and bathymetric profile and map (bottom two panels, like Figure 5 of the Main Text), for MERMAID P0026.

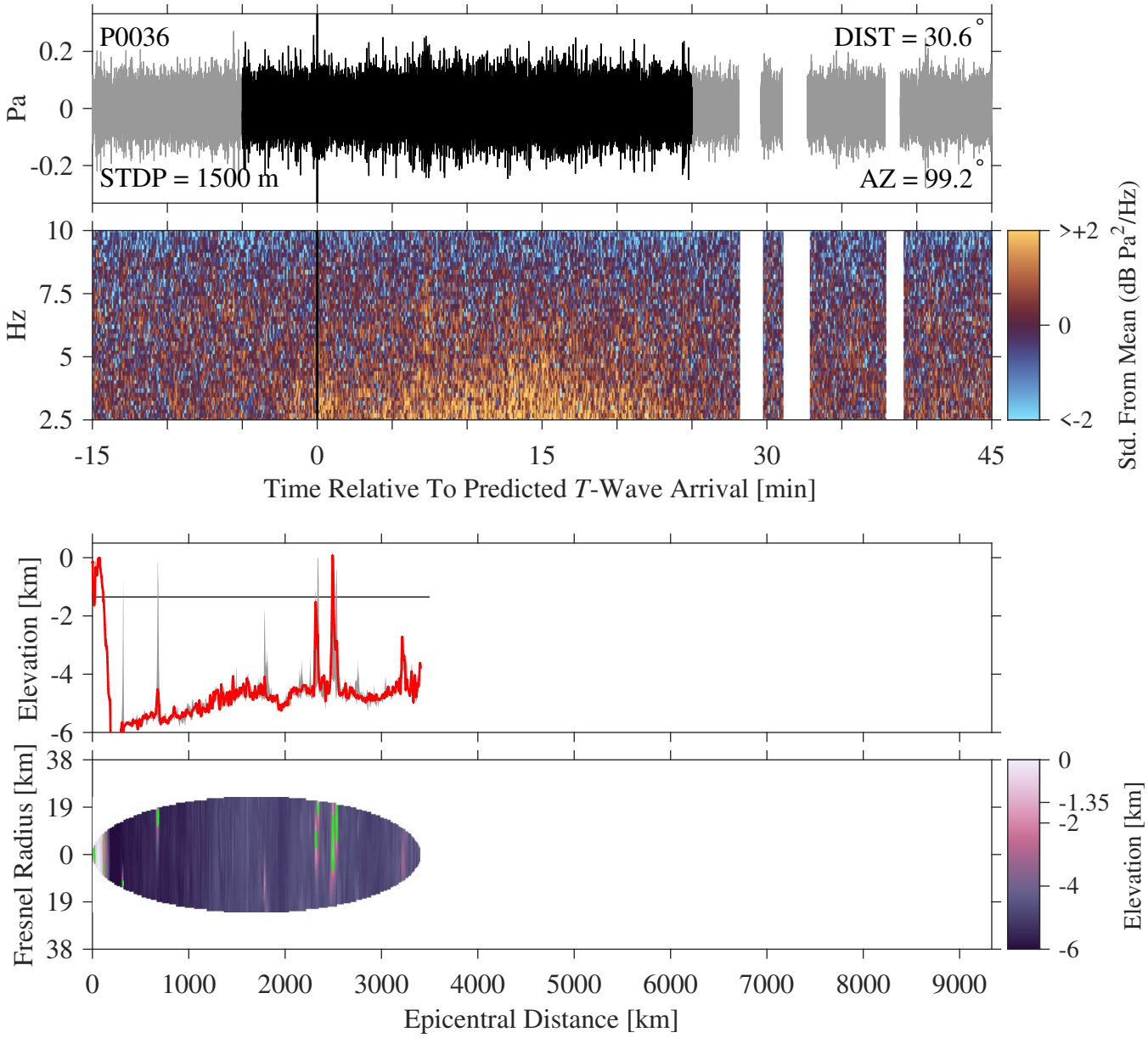

Figure S22. Time and spectral domain signals (two top panels, like Figures 3–4 of the Main Text), and bathymetric profile and map (bottom two panels, like Figure 5 of the Main Text), for MERMAID P0036.

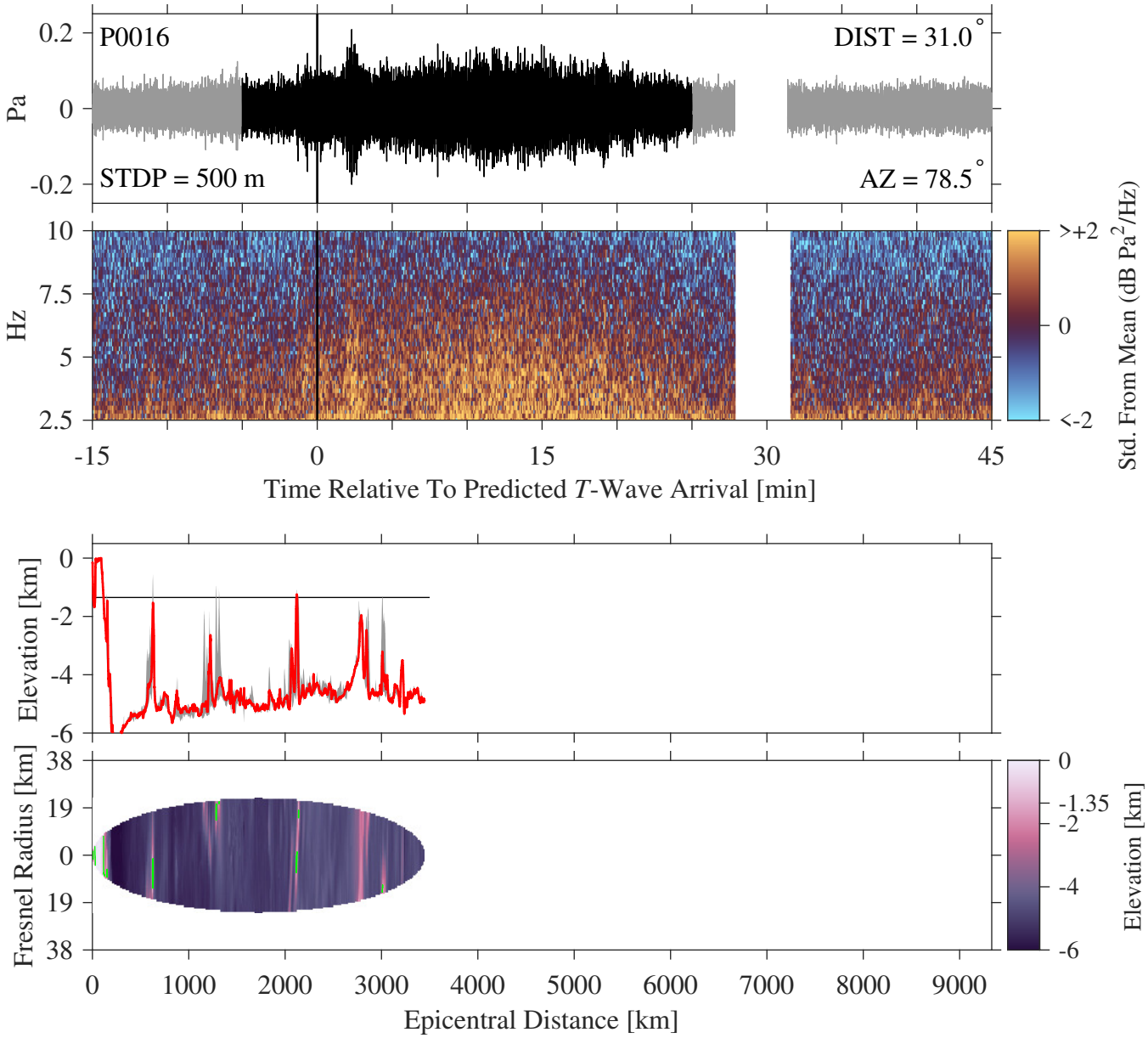

Figure S23. Time and spectral domain signals (two top panels, like Figures 3–4 of the Main Text), and bathymetric profile and map (bottom two panels, like Figure 5 of the Main Text), for MERMAID P0016.

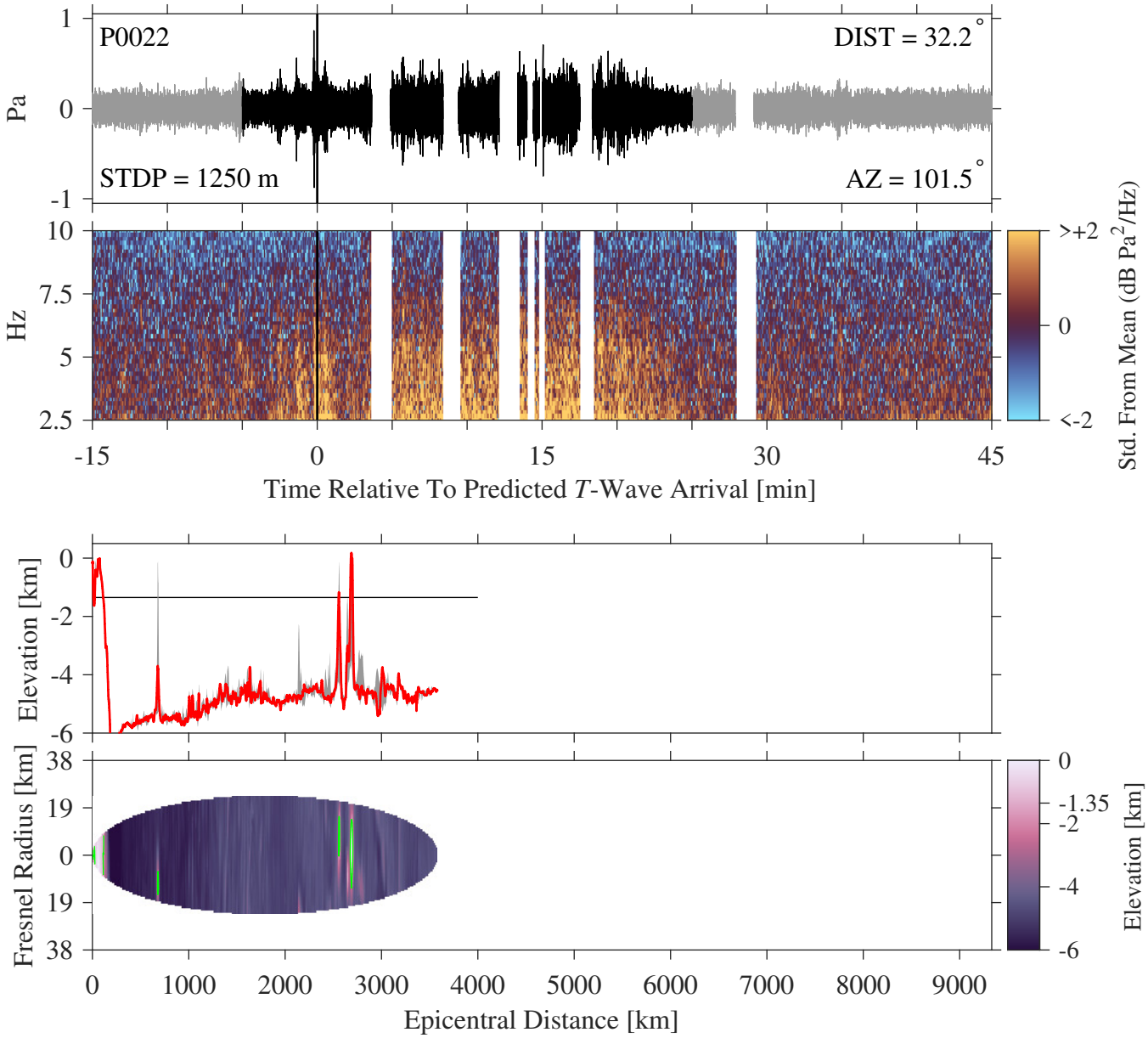

Figure S24. Time and spectral domain signals (two top panels, like Figures 3–4 of the Main Text), and bathymetric profile and map (bottom two panels, like Figure 5 of the Main Text), for MERMAID P0022.

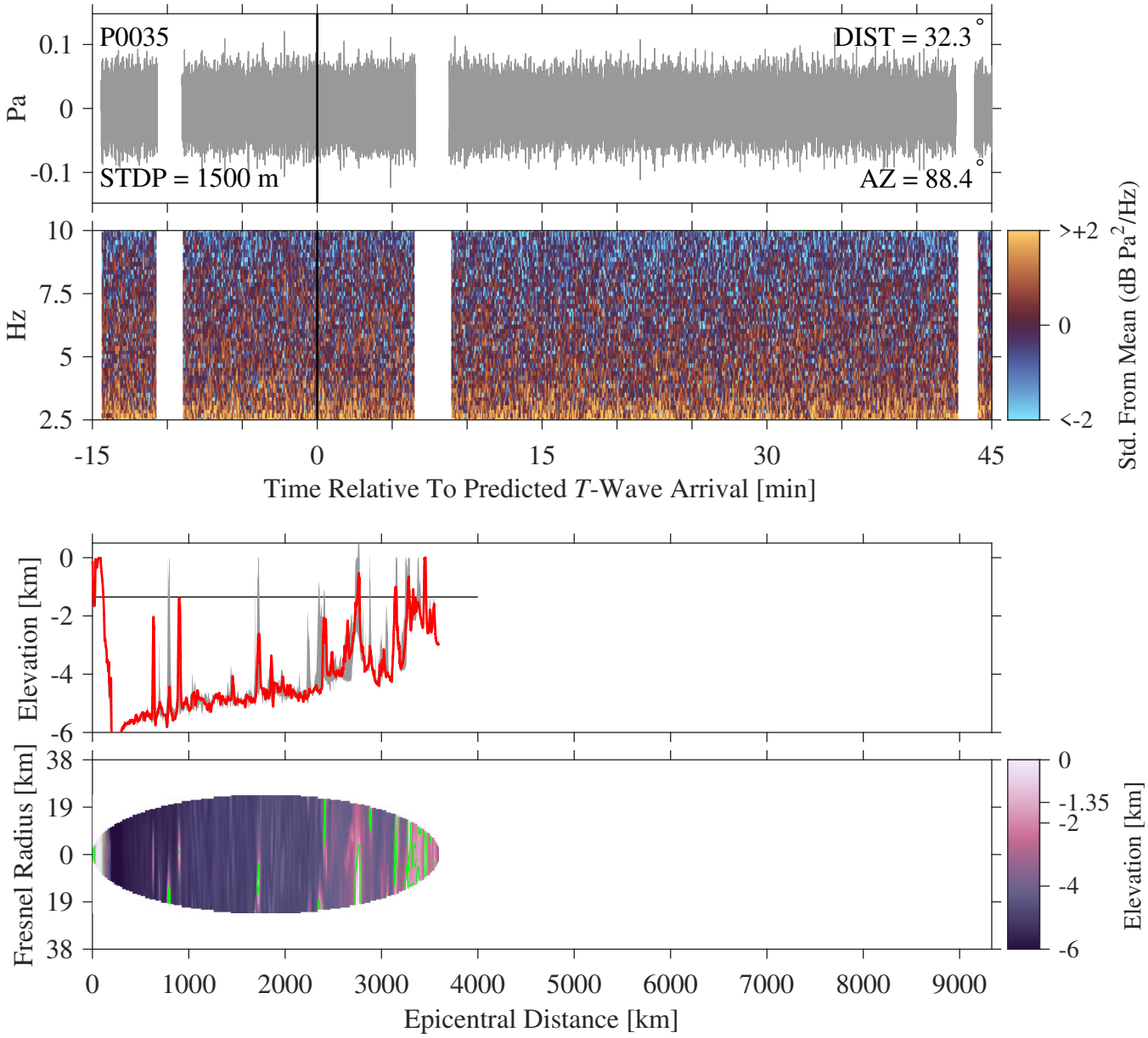

Figure S25. Time and spectral domain signals (two top panels, like Figures 3–4 of the Main Text), and bathymetric profile and map (bottom two panels, like Figure 5 of the Main Text), for MERMAID P0035.

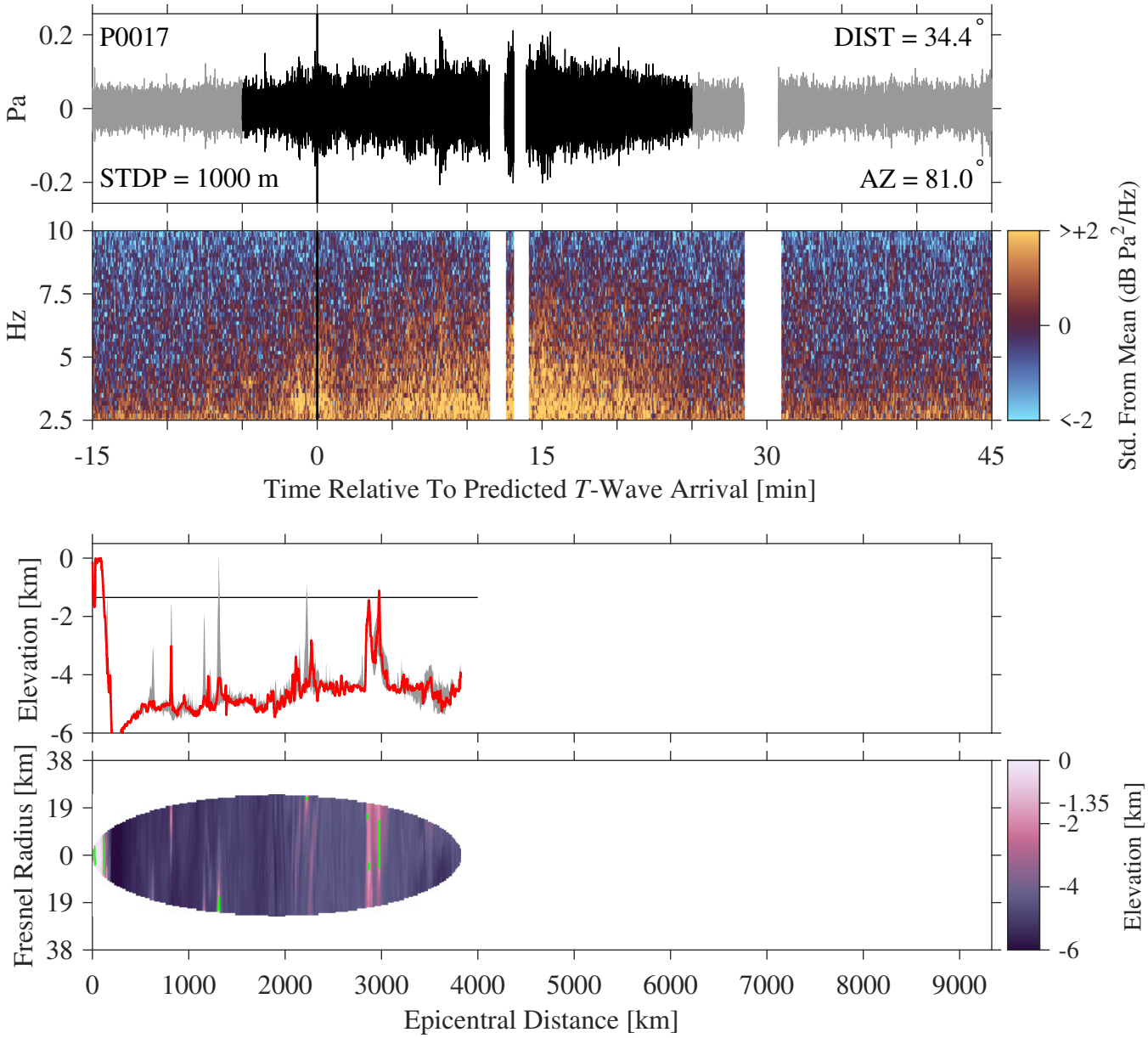

Figure S26. Time and spectral domain signals (two top panels, like Figures 3–4 of the Main Text), and bathymetric profile and map (bottom two panels, like Figure 5 of the Main Text), for MERMAID P0017.

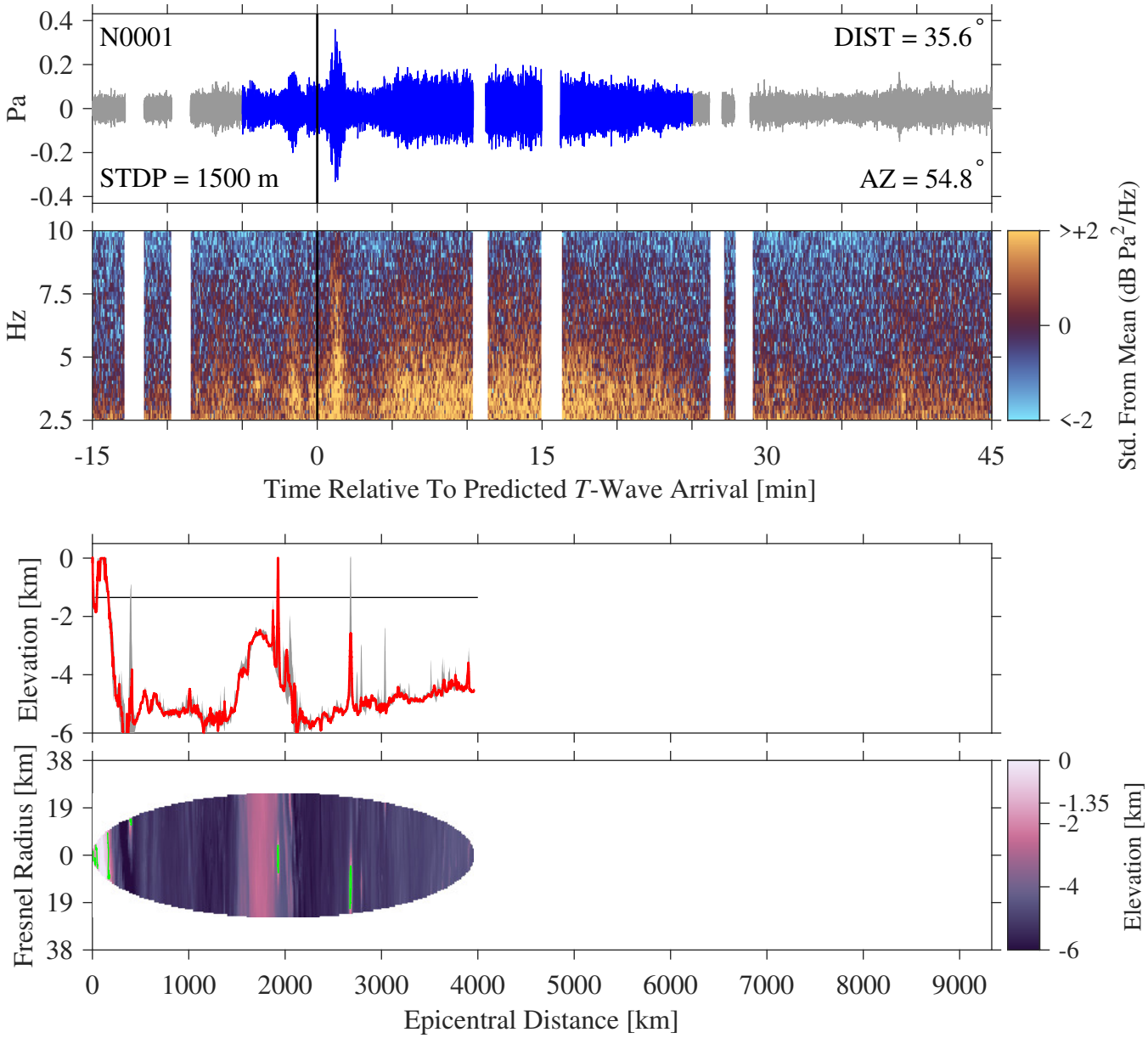

Figure S27. Time and spectral domain signals (two top panels, like Figures 3–4 of the Main Text), and bathymetric profile and map (bottom two panels, like Figure 5 of the Main Text), for MERMAID N0001.

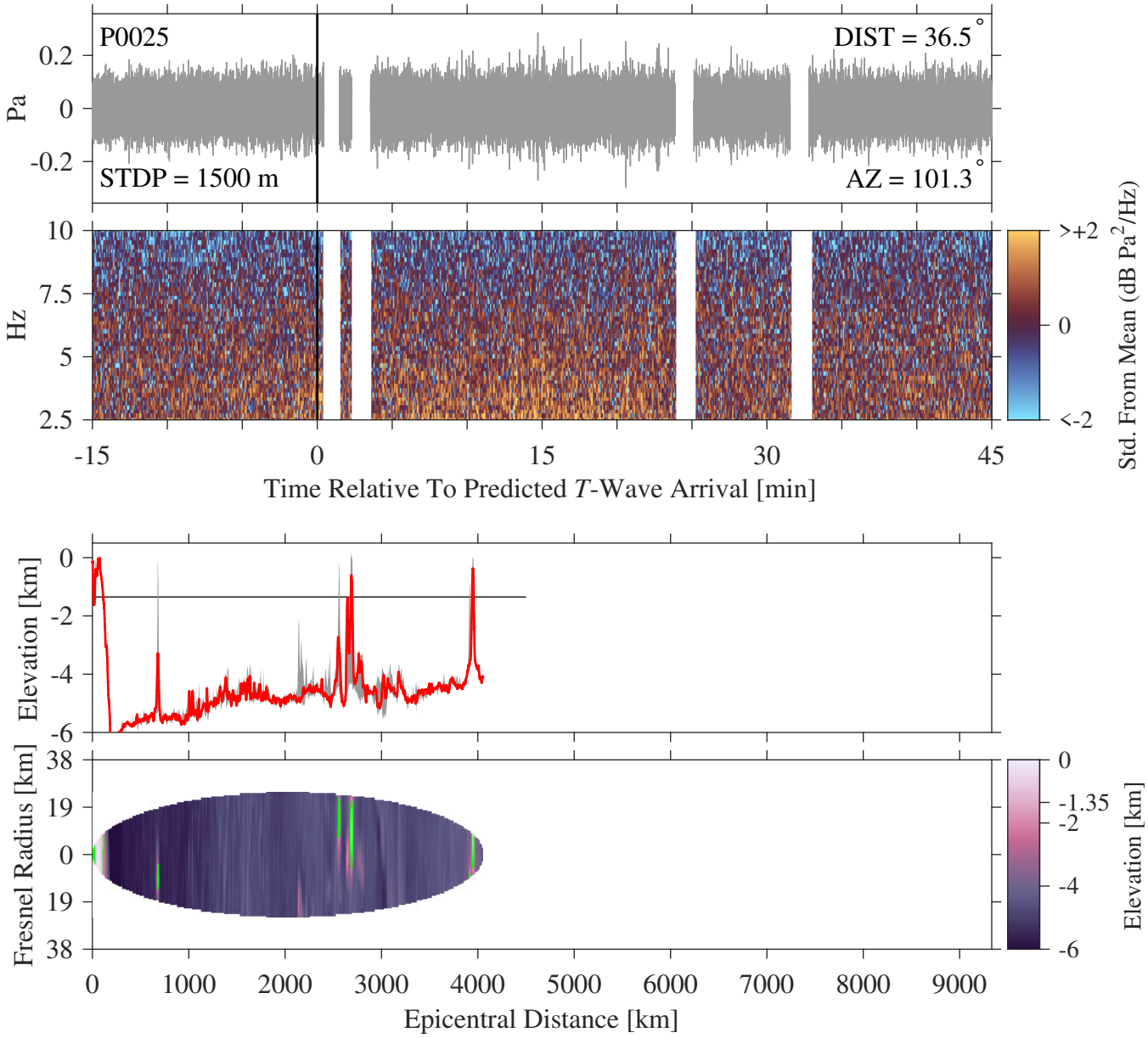

Figure S28. Time and spectral domain signals (two top panels, like Figures 3–4 of the Main Text), and bathymetric profile and map (bottom two panels, like Figure 5 of the Main Text), for MERMAID P0025.

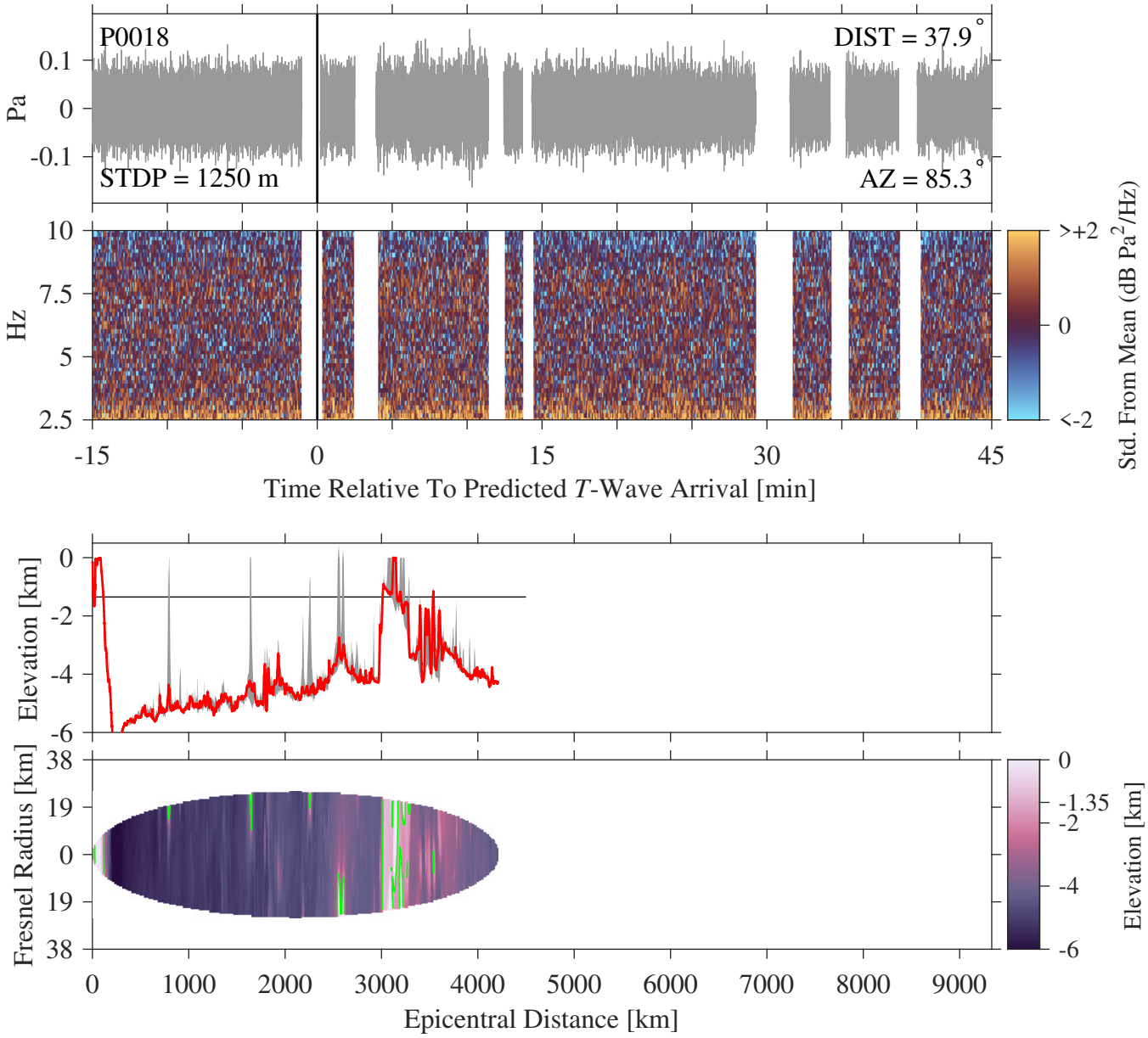

Figure S29. Time and spectral domain signals (two top panels, like Figures 3–4 of the Main Text), and bathymetric profile and map (bottom two panels, like Figure 5 of the Main Text), for MERMAID P0018.

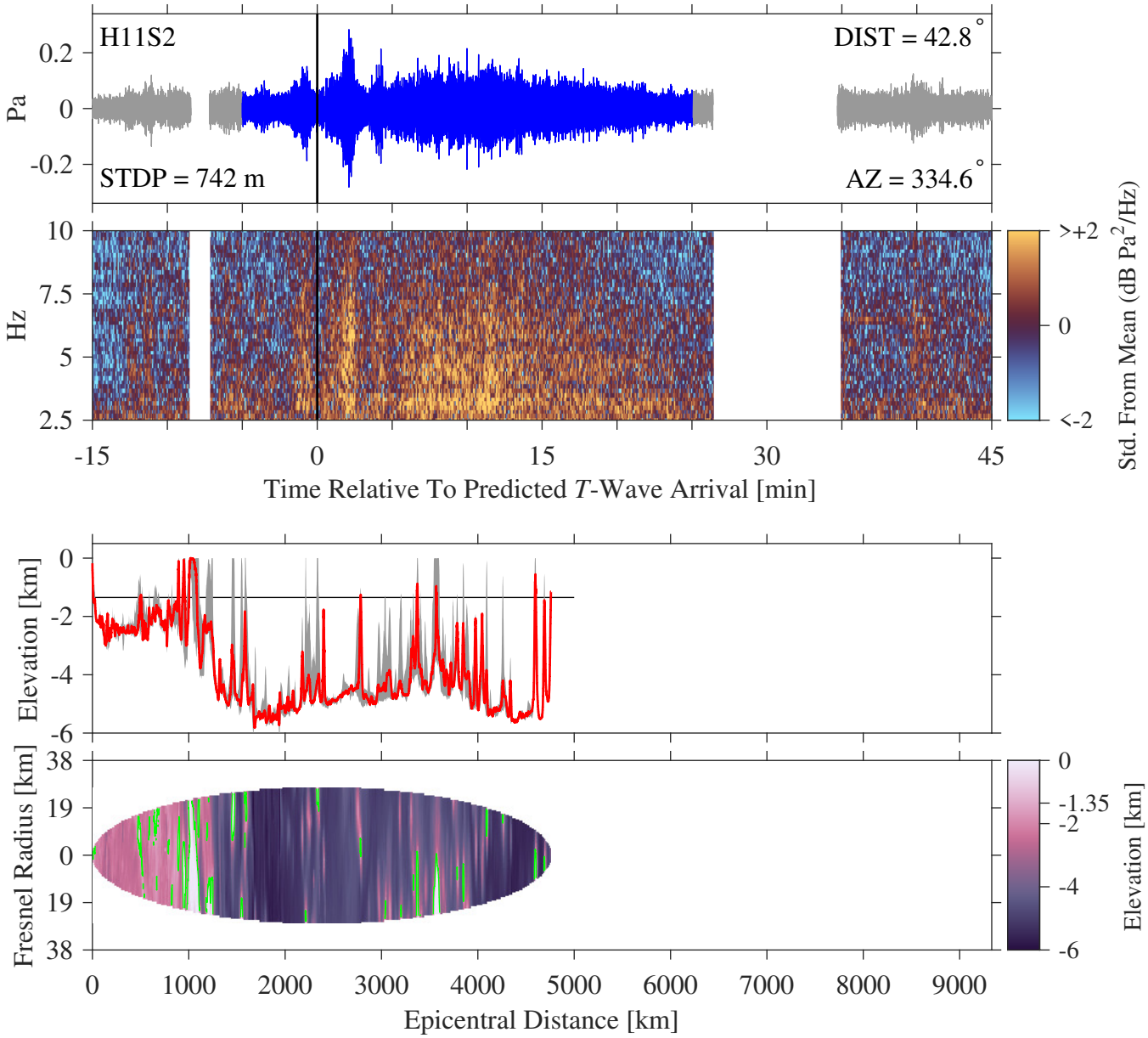

Figure S30. Time and spectral domain signals (two top panels, like Figures 3–4 of the Main Text), and bathymetric profile and map (bottom two panels, like Figure 5 of the Main Text), for IMS receiver H11S2.

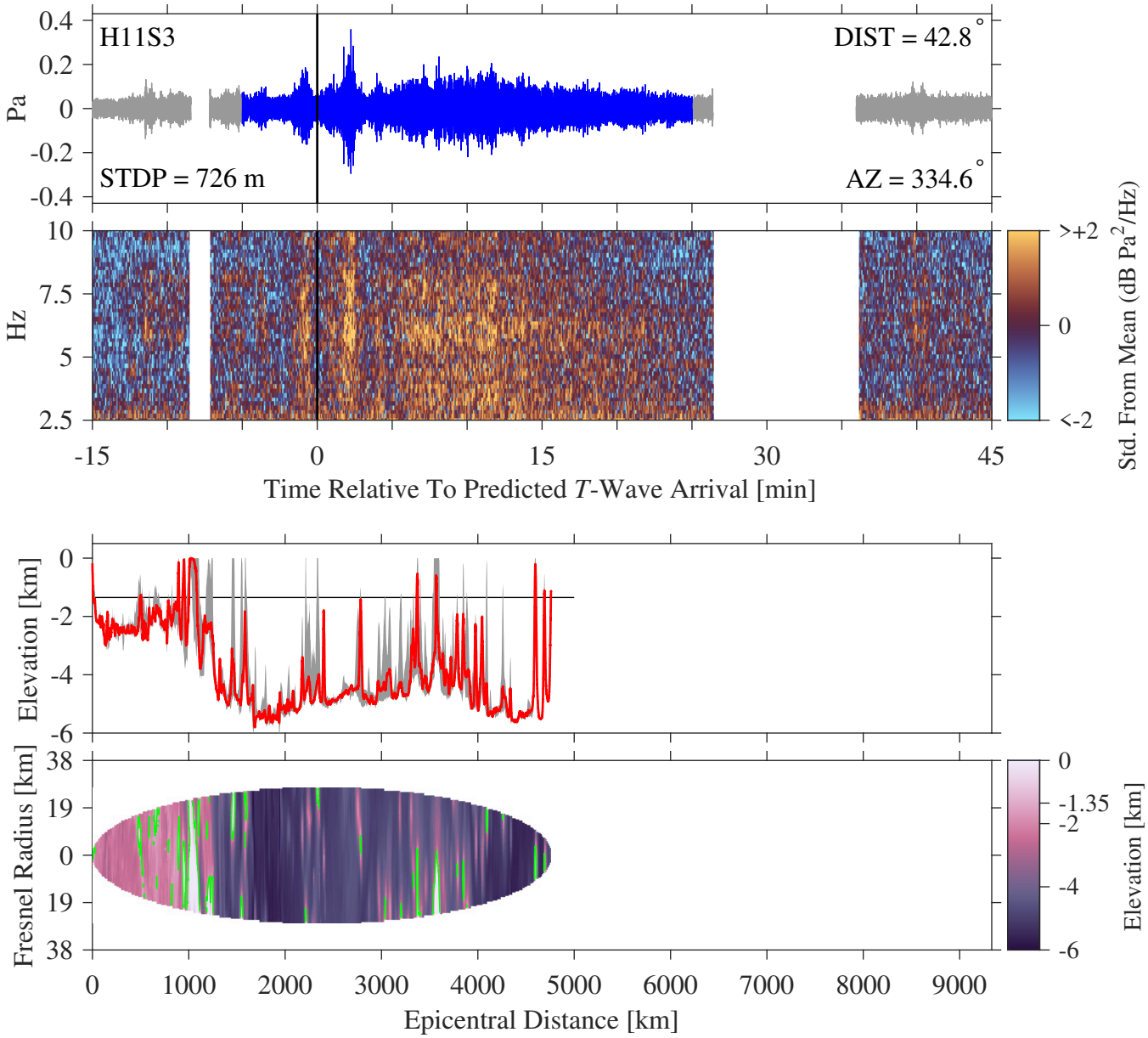

Figure S31. Time and spectral domain signals (two top panels, like Figures 3–4 of the Main Text), and bathymetric profile and map (bottom two panels, like Figure 5 of the Main Text), for IMS receiver H11S3.

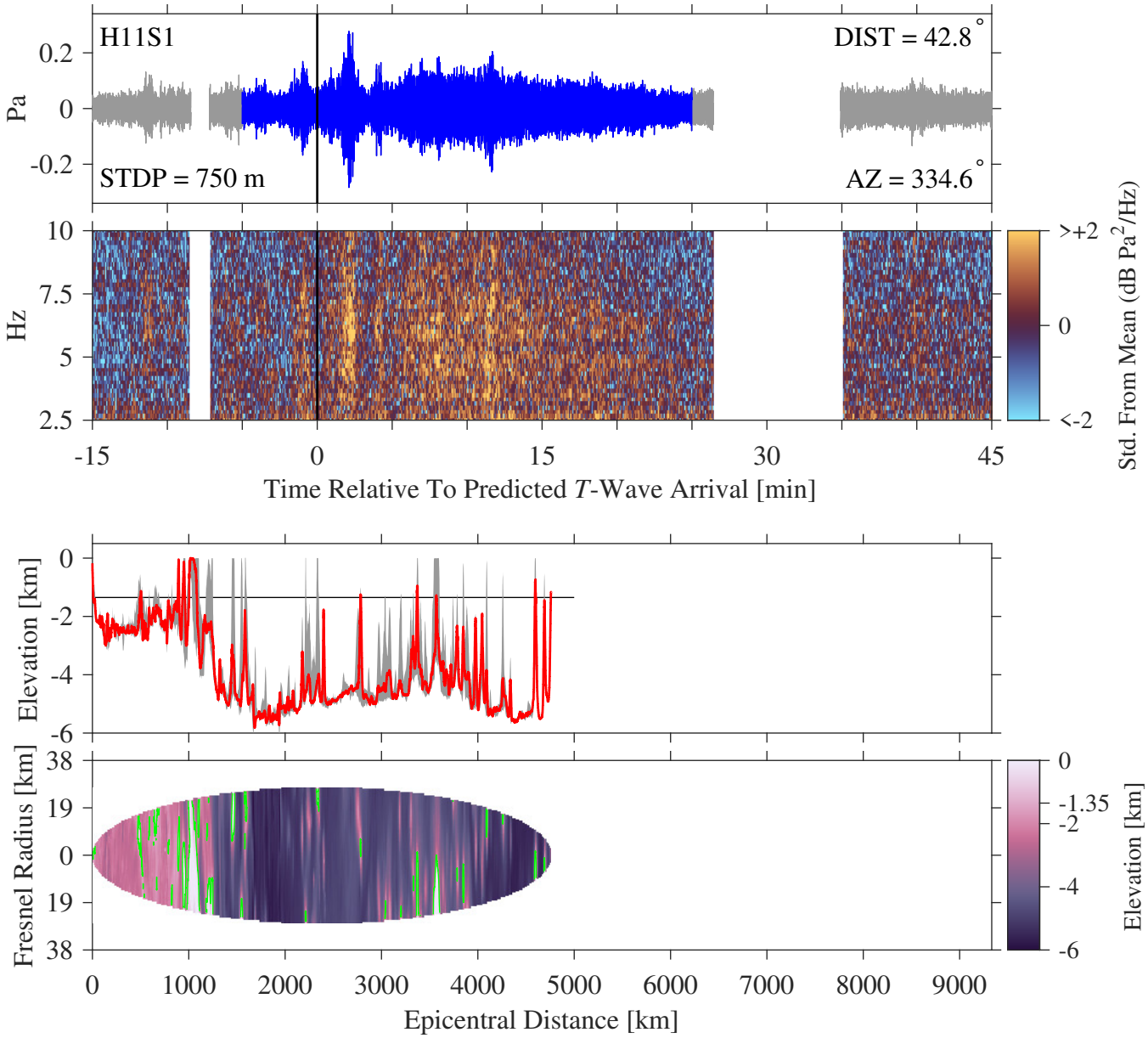

Figure S32. Time and spectral domain signals (two top panels, like Figures 3–4 of the Main Text), and bathymetric profile and map (bottom two panels, like Figure 5 of the Main Text), for IMS receiver H11S1.

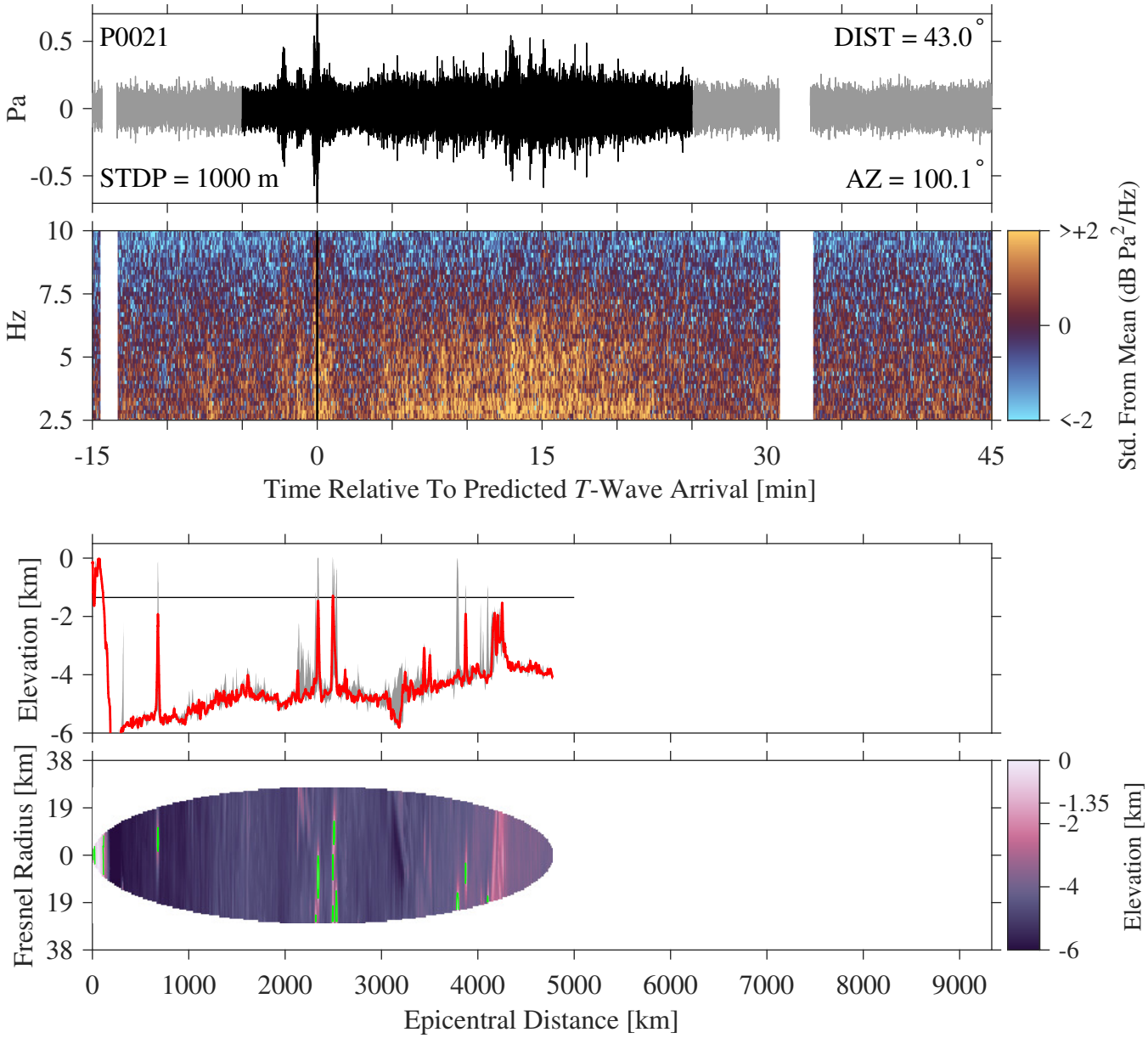

Figure S33. Time and spectral domain signals (two top panels, like Figures 3–4 of the Main Text), and bathymetric profile and map (bottom two panels, like Figure 5 of the Main Text), for MERMAID P0021.

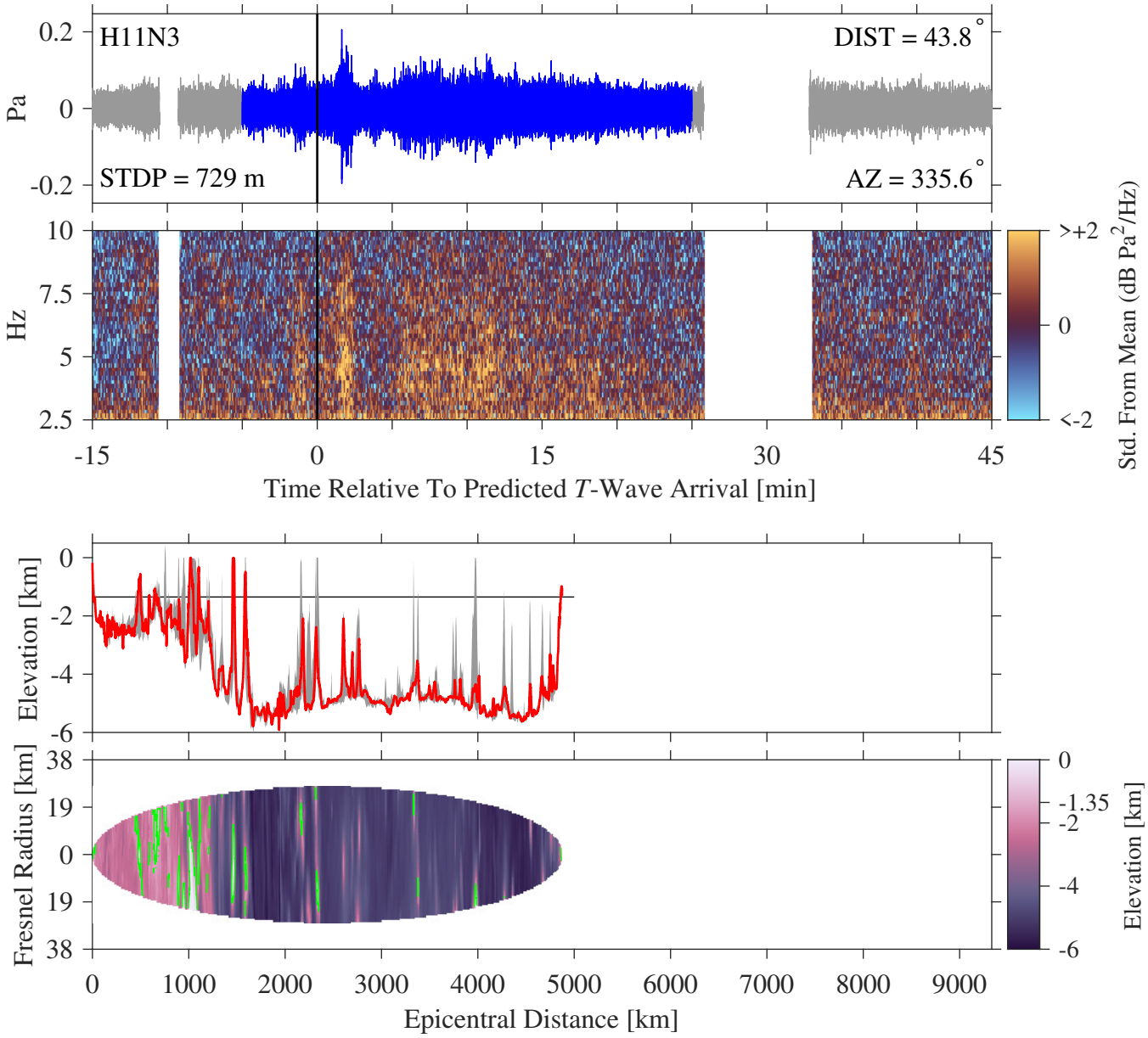

Figure S34. Time and spectral domain signals (two top panels, like Figures 3–4 of the Main Text), and bathymetric profile and map (bottom two panels, like Figure 5 of the Main Text), for IMS receiver H11N3.

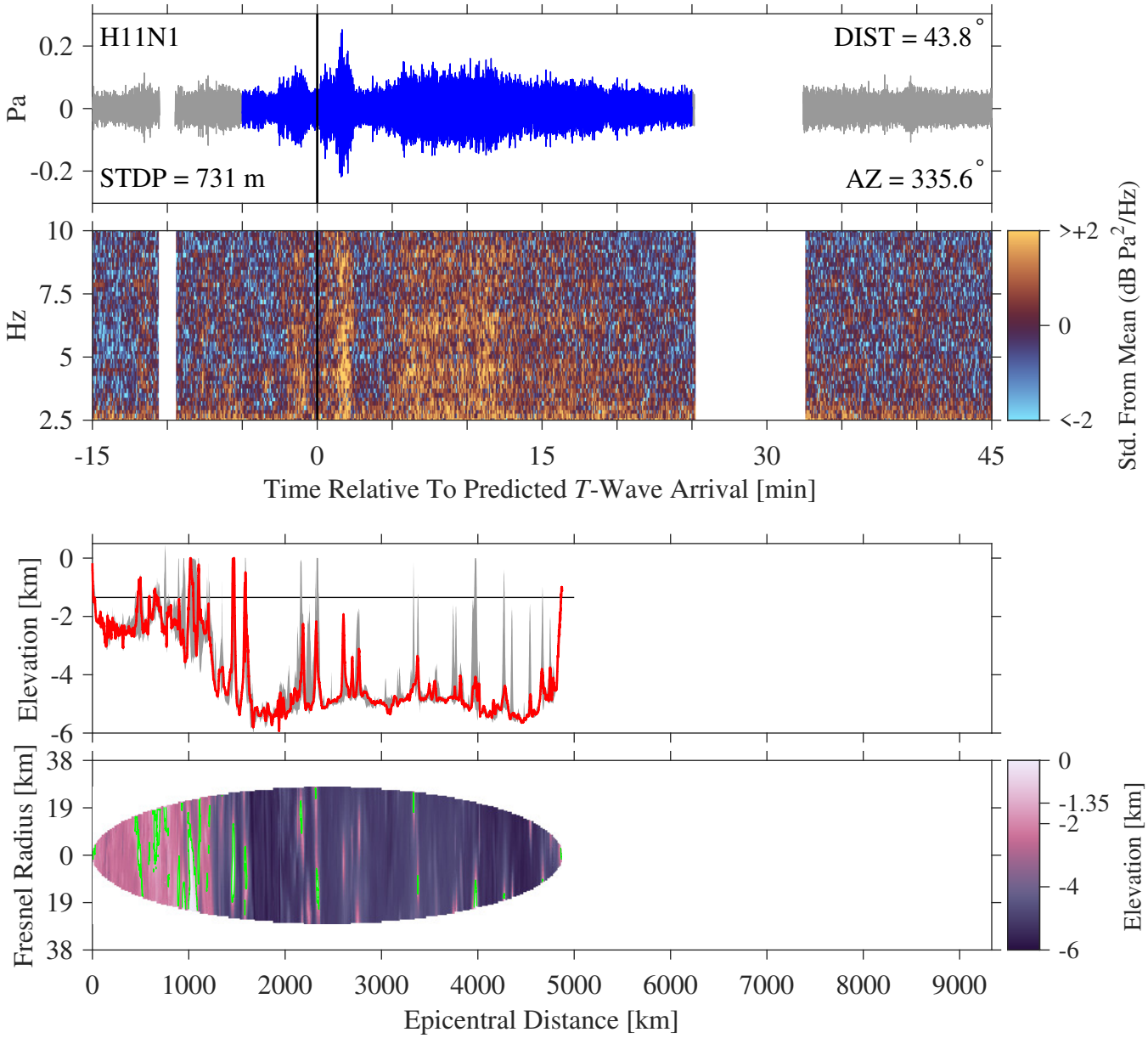

Figure S35. Time and spectral domain signals (two top panels, like Figures 3–4 of the Main Text), and bathymetric profile and map (bottom two panels, like Figure 5 of the Main Text), for IMS receiver H11N1.

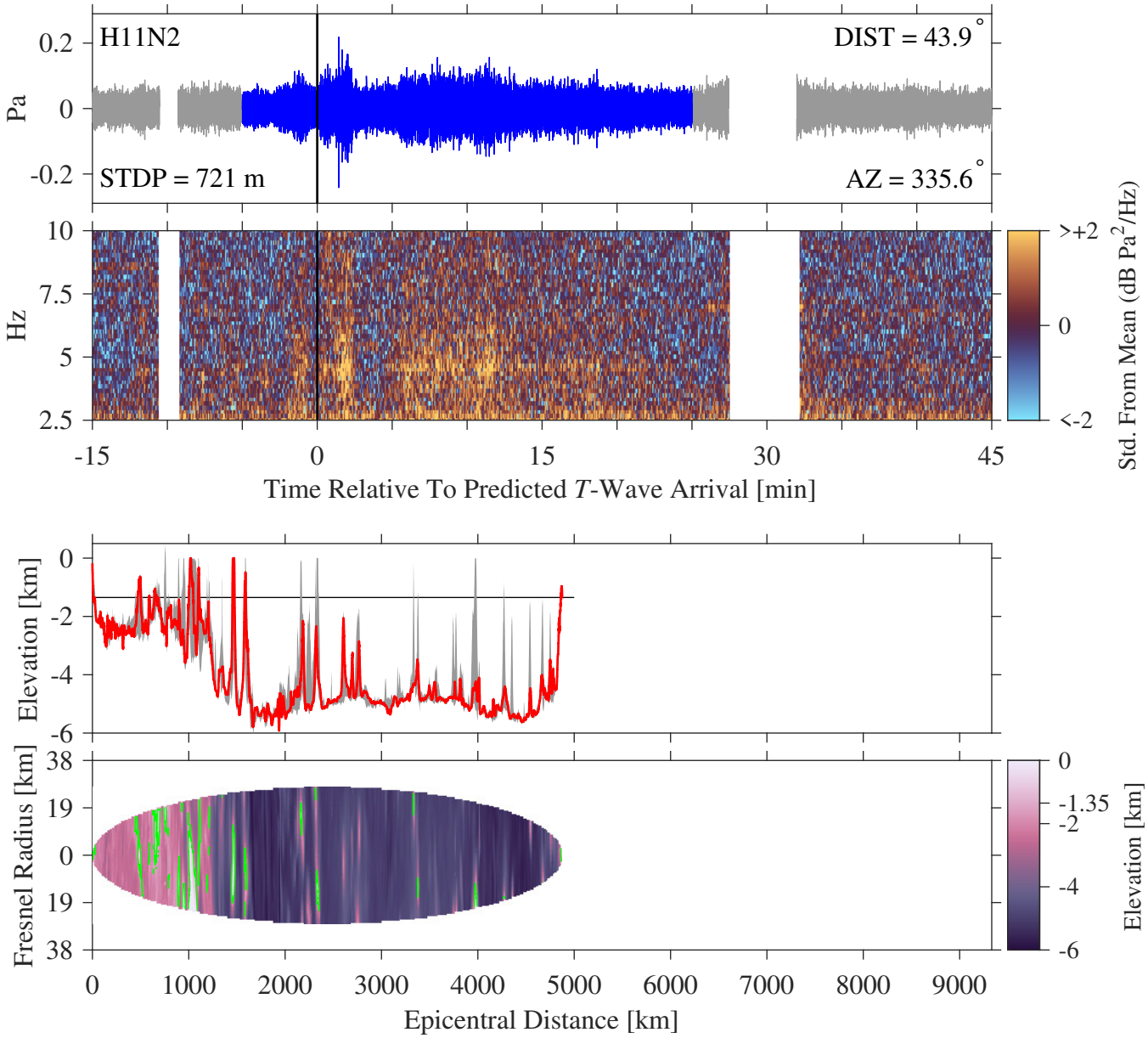

Figure S36. Time and spectral domain signals (two top panels, like Figures 3–4 of the Main Text), and bathymetric profile and map (bottom two panels, like Figure 5 of the Main Text), for IMS receiver H11N2.

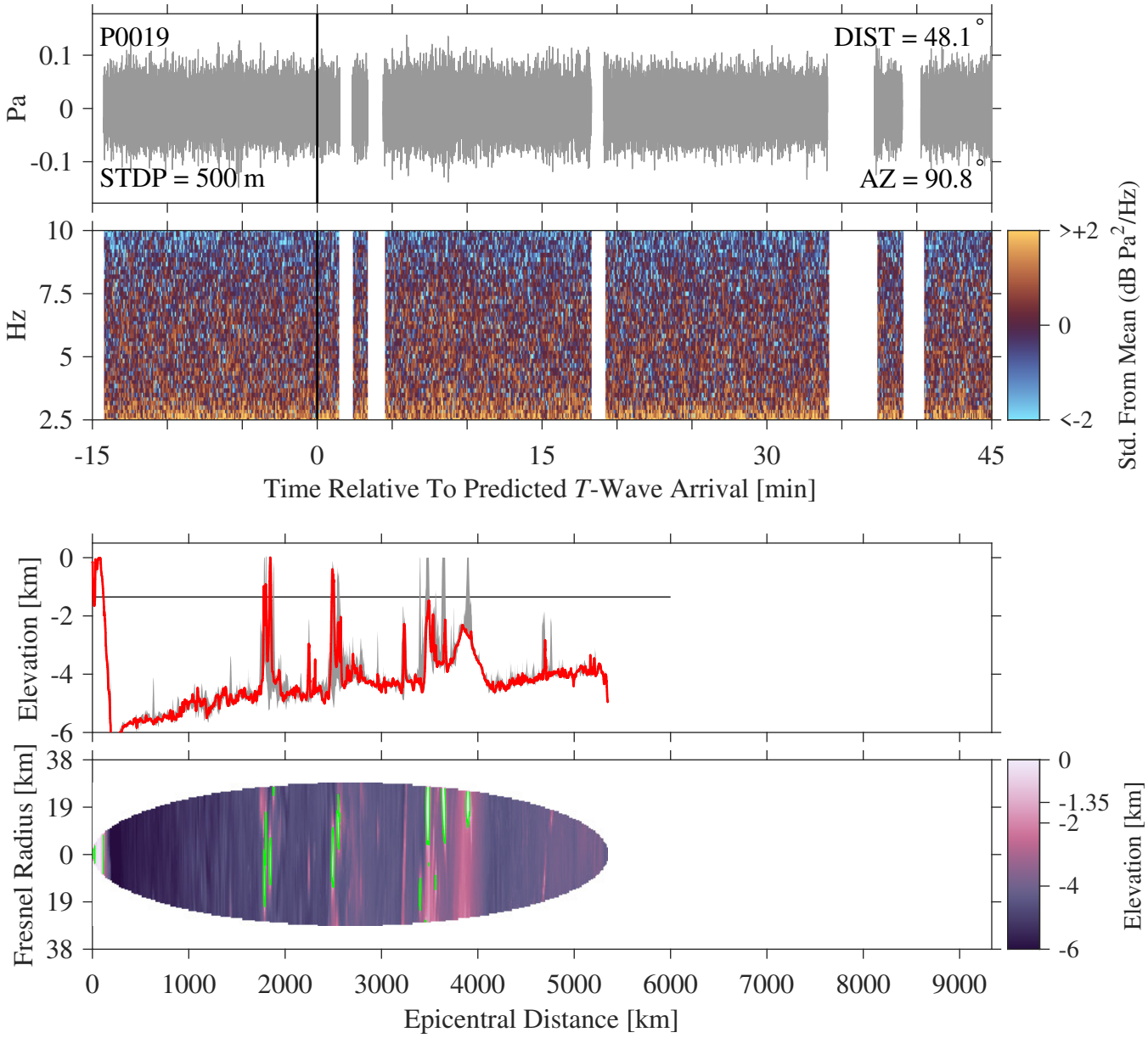

Figure S37. Time and spectral domain signals (two top panels, like Figures 3–4 of the Main Text), and bathymetric profile and map (bottom two panels, like Figure 5 of the Main Text), for MERMAID P0019.

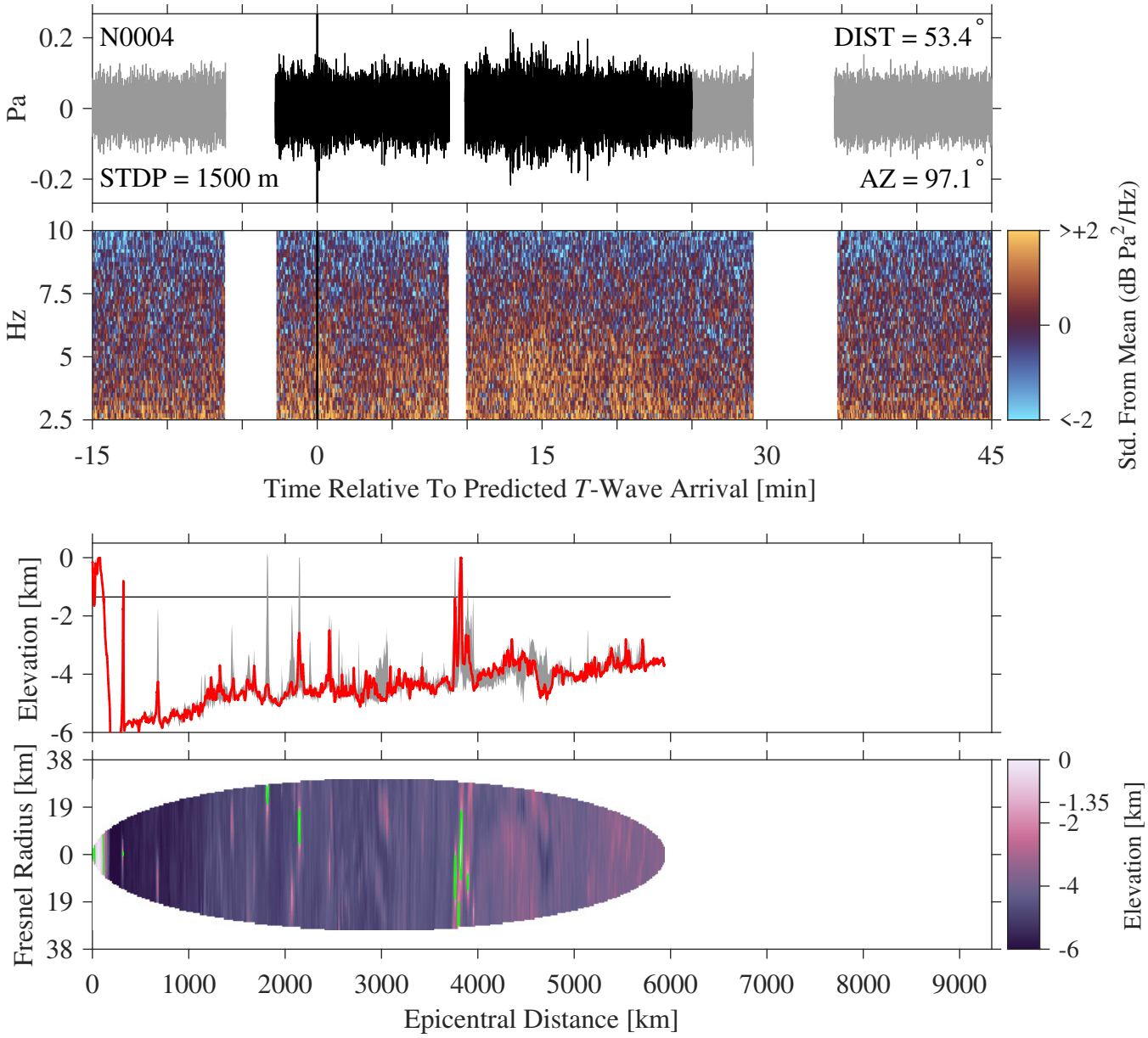

Figure S38. Time and spectral domain signals (two top panels, like Figures 3–4 of the Main Text), and bathymetric profile and map (bottom two panels, like Figure 5 of the Main Text), for MERMAID N0004.

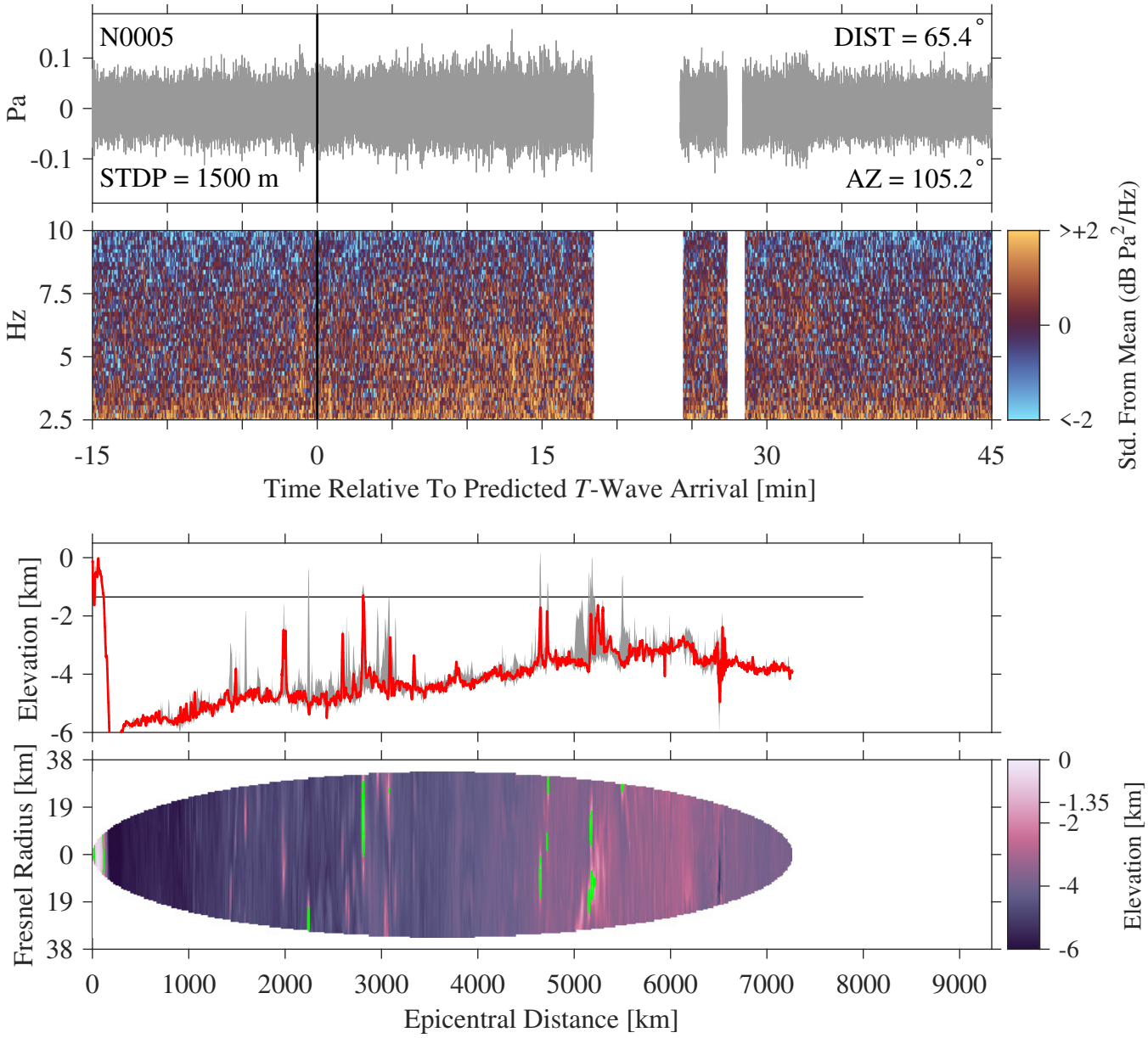

Figure S39. Time and spectral domain signals (two top panels, like Figures 3–4 of the Main Text), and bathymetric profile and map (bottom two panels, like Figure 5 of the Main Text), for MERMAID N0005.

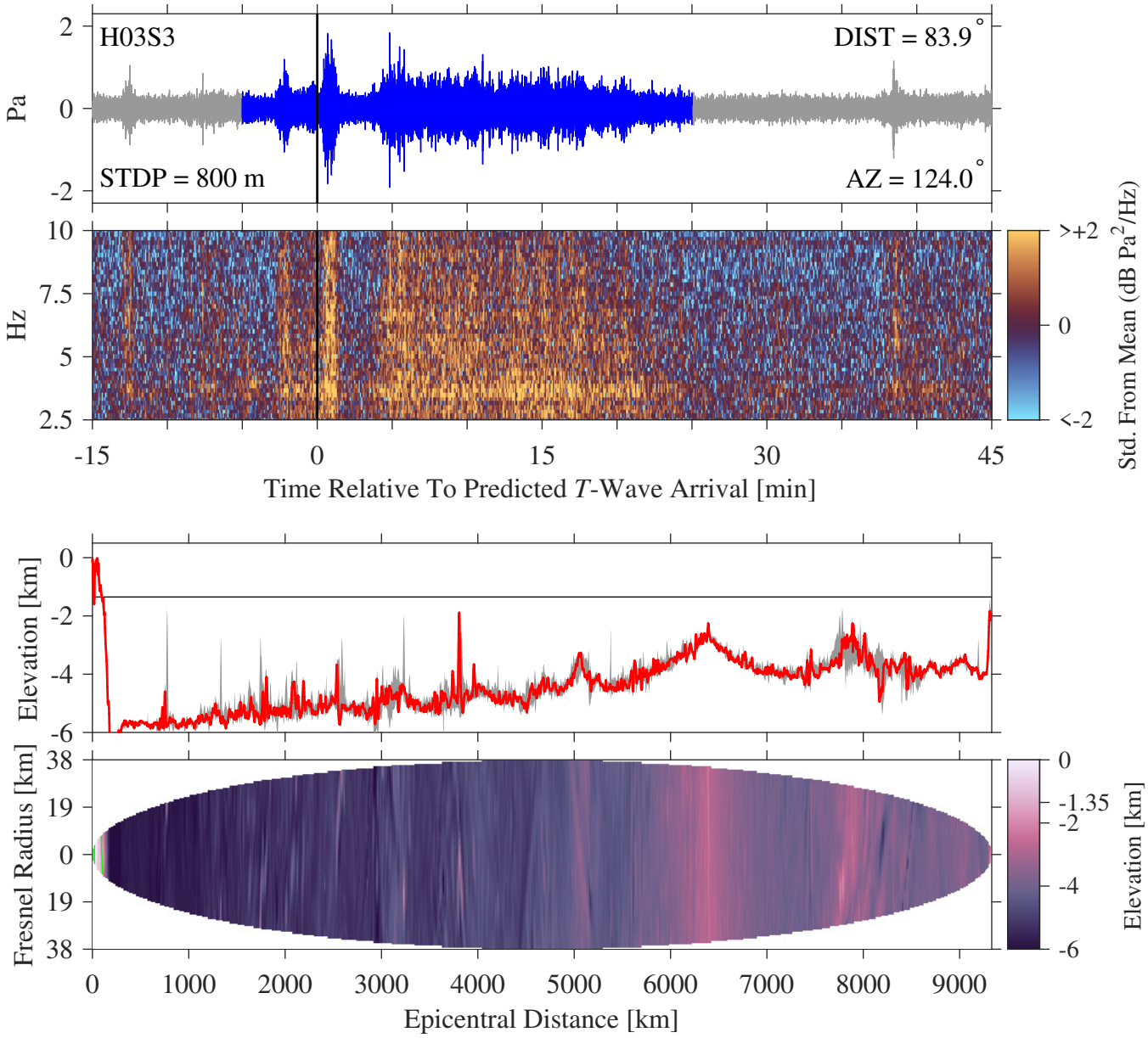

Figure S40. Time and spectral domain signals (two top panels, like Figures 3–4 of the Main Text), and bathymetric profile and map (bottom two panels, like Figure 5 of the Main Text), for IMS receiver H03S3.

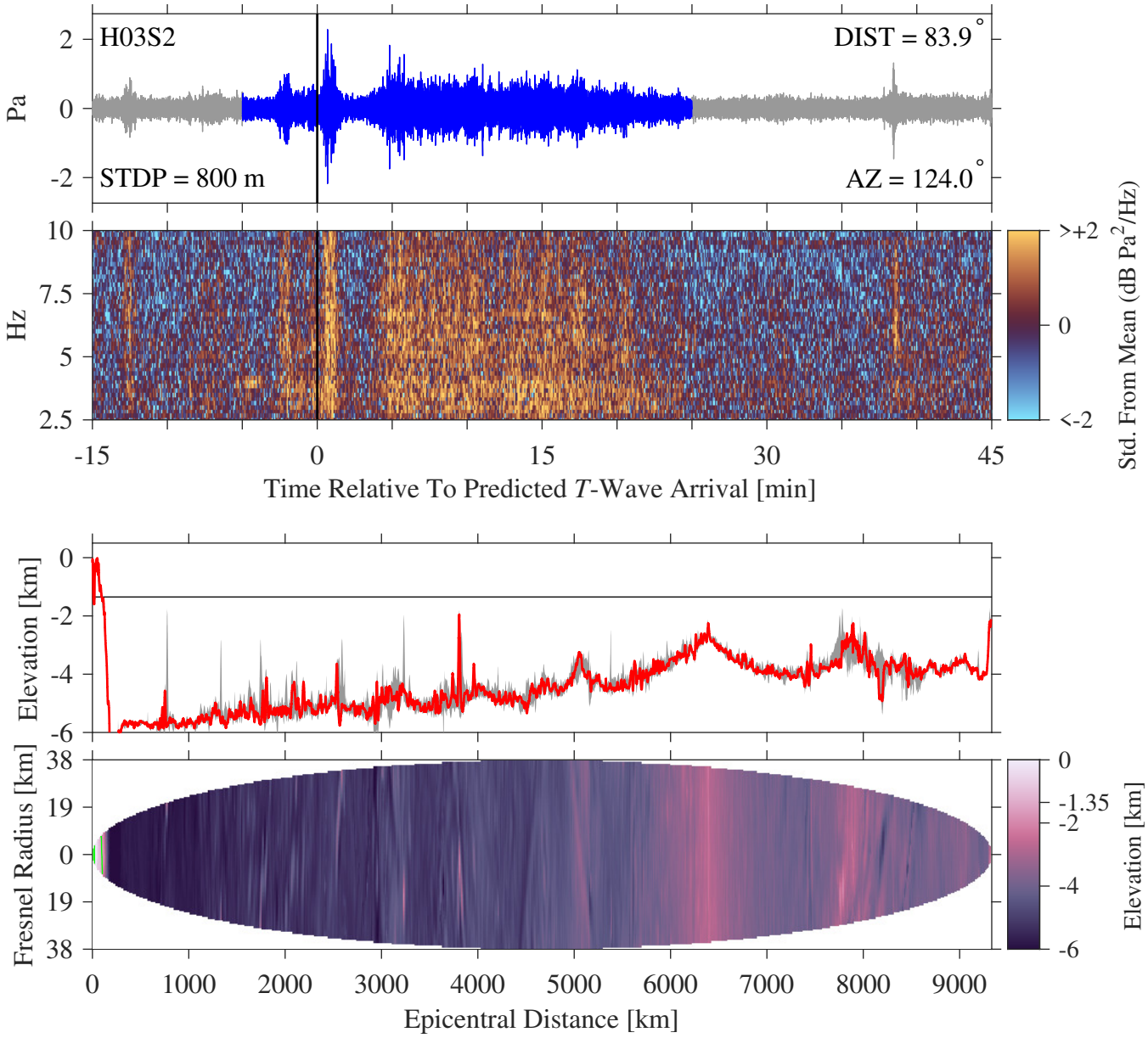

Figure S41. Time and spectral domain signals (two top panels, like Figures 3–4 of the Main Text), and bathymetric profile and map (bottom two panels, like Figure 5 of the Main Text), for IMS receiver H03S2.

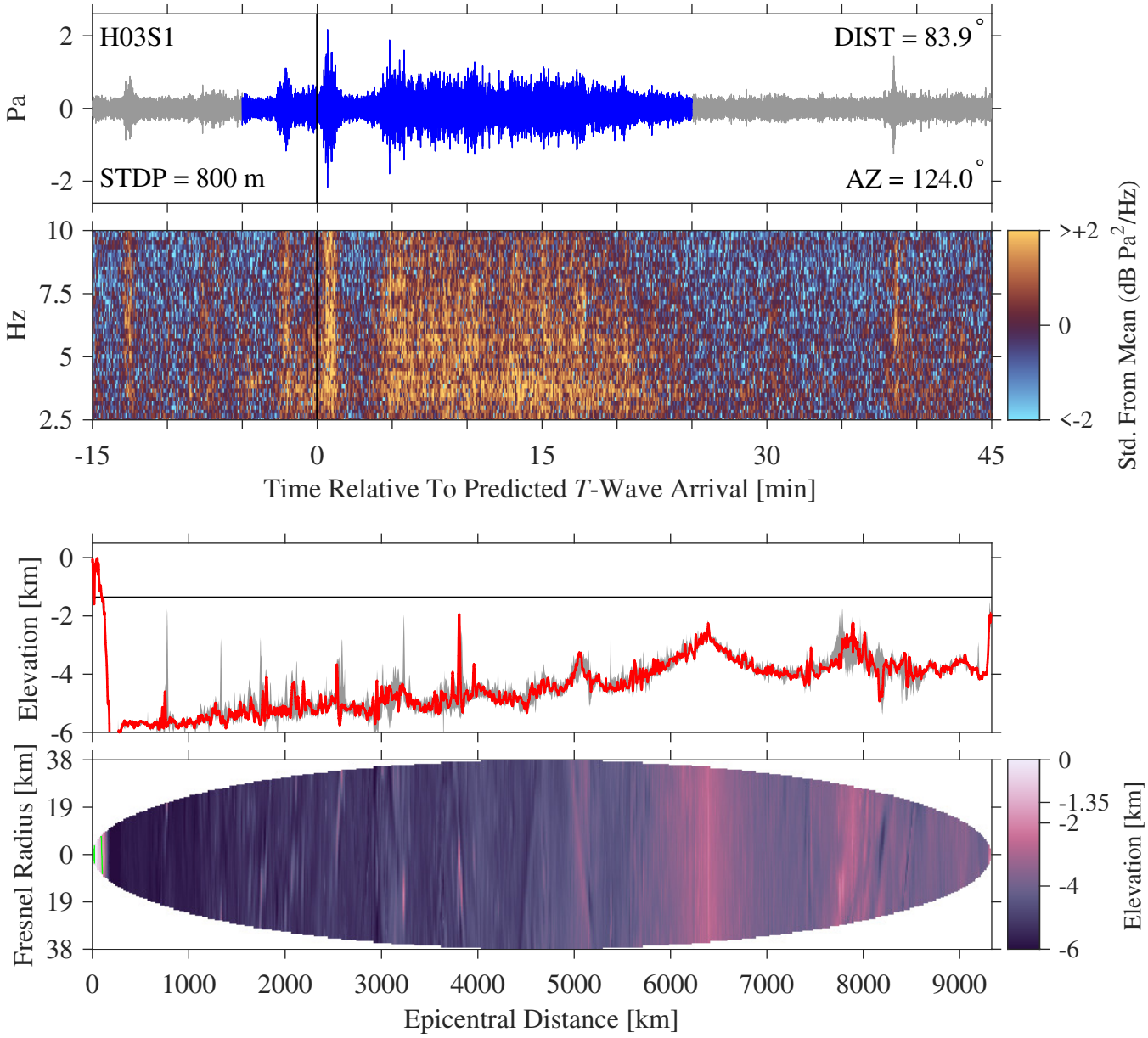

Figure S42. Time and spectral domain signals (two top panels, like Figures 3–4 of the Main Text), and bathymetric profile and map (bottom two panels, like Figure 5 of the Main Text), for IMS receiver H03S1.

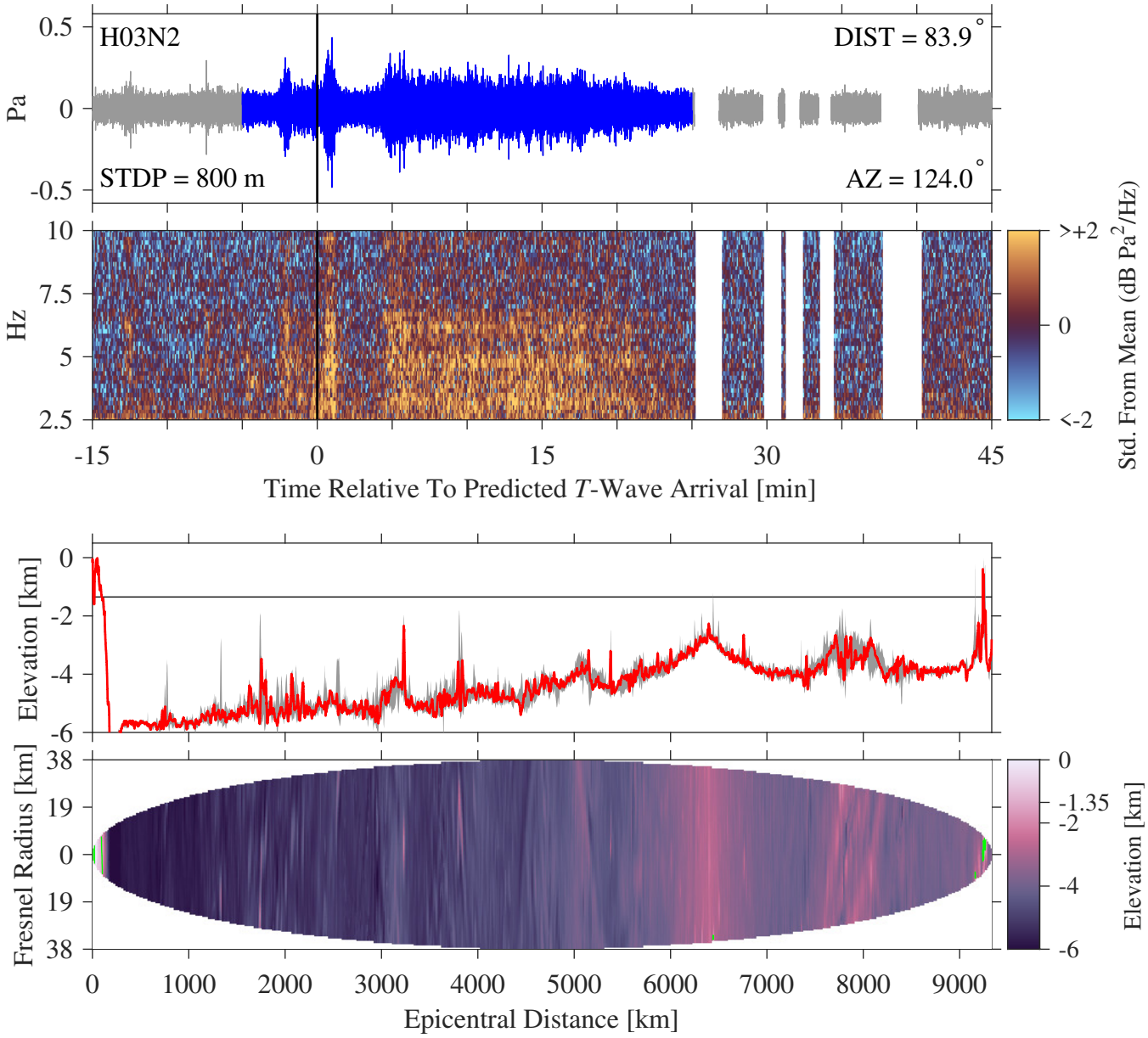

Figure S43. Time and spectral domain signals (two top panels, like Figures 3–4 of the Main Text), and bathymetric profile and map (bottom two panels, like Figure 5 of the Main Text), for IMS receiver H03N2. Note the bathymetric occlusions near the receiver, which explain signal loss compared to the complementary southern triad.

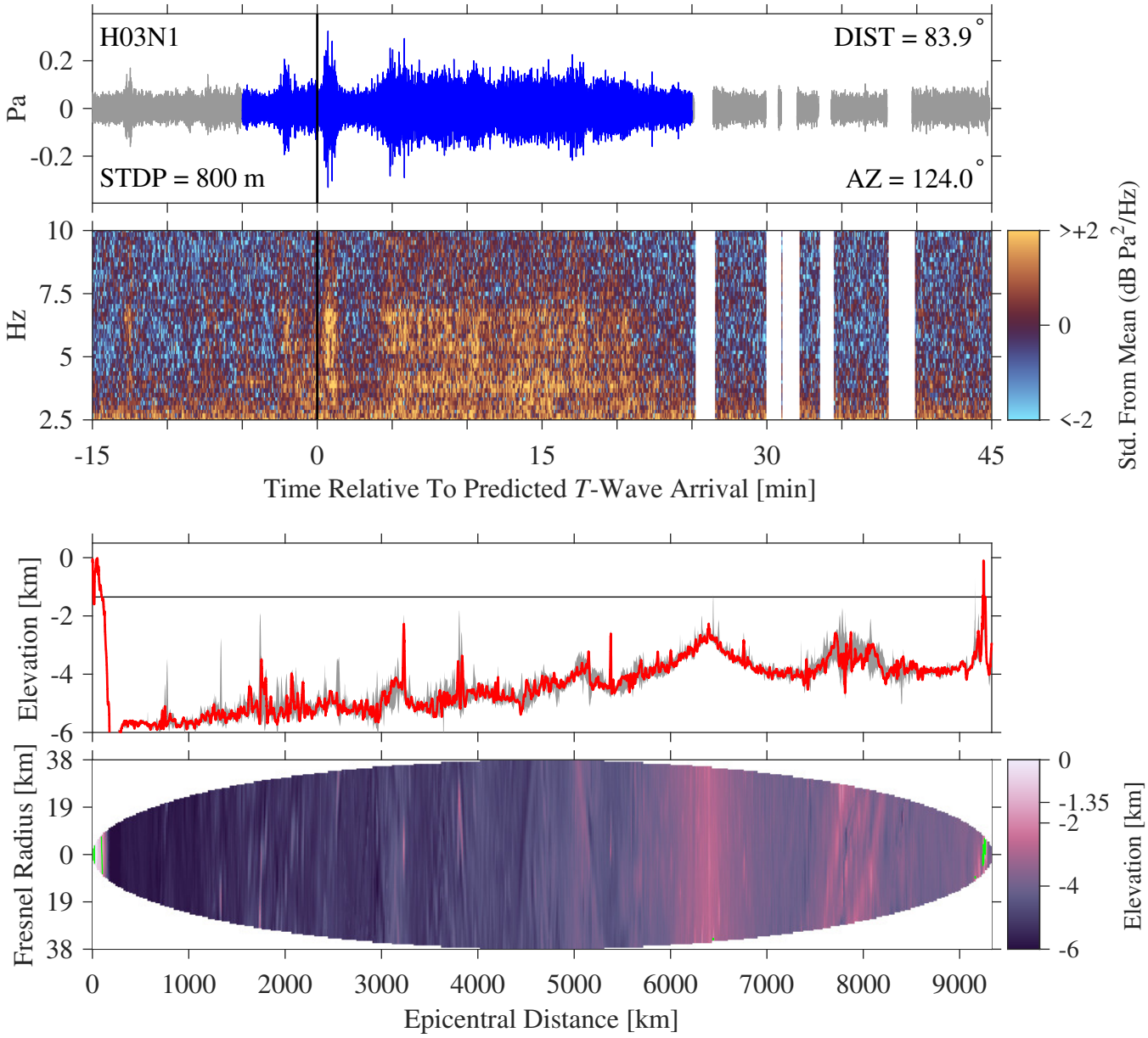

Figure S44. Time and spectral domain signals (two top panels, like Figures 3–4 of the Main Text), and bathymetric profile and map (bottom two panels, like Figure 5 of the Main Text), for IMS receiver H03N1. Note the bathymetric occlusions near the receiver, which explain signal loss compared to the complementary southern triad.

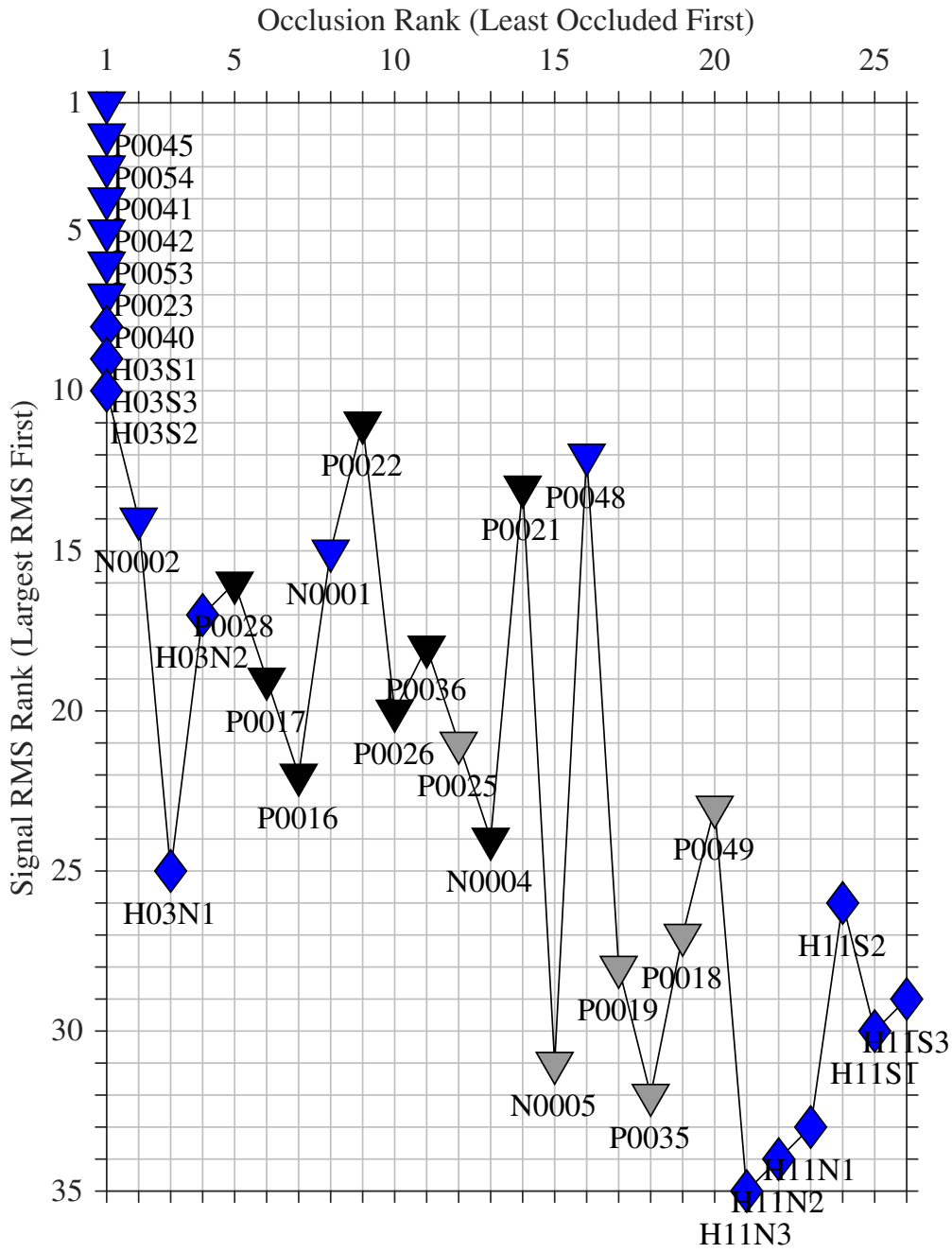

Figure S45. Ranked root-mean-squared (RMS) pressures in the 30-minute *T*-wave window, defined in Section 2 of the Main Text, versus their ranked occlusion count, $\Lambda_{1.0}$. All stations with zero occlusion count are stacked in the top left corner. Receiver symbols and colors are as in the Main Text. Overall, RMS pressure appears to fall off with increasing occlusion count.

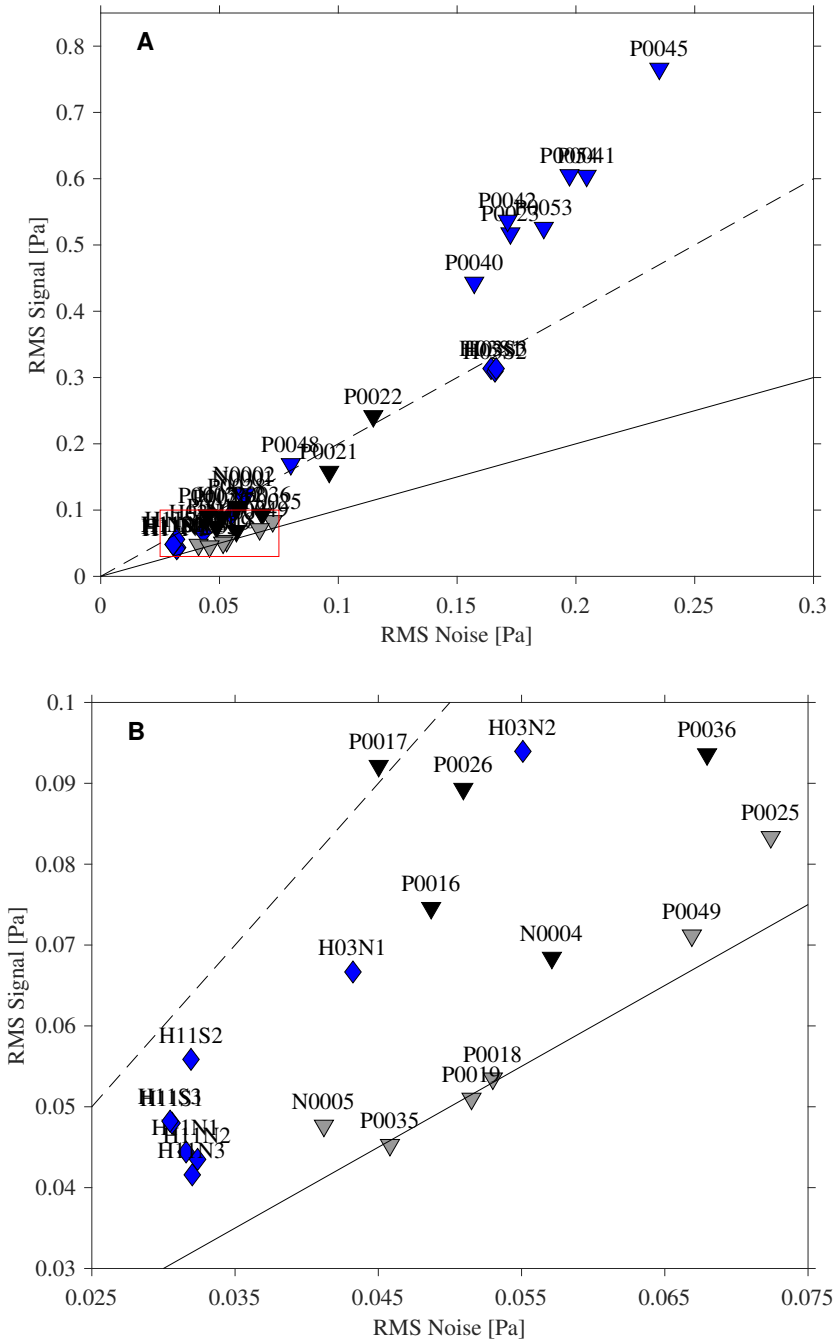

Figure S46. RMS pressure of the 30-minute *T*-wave signal window versus that of the preceding 10-minute "noise" window. (A) All stations, and (B) zoom-in of red rectangle in (A). Solid and dashed lines mark 1:1 and 2:1 SNRs, respectively. All Category C records, which show scant if any signal, lie on or near the 1:1: line.